Electrode-particle Impacts

A thesis submitted for the degree of Doctor of Philosophy

in Physical and Theoretical Chemistry

Stanislav V. Sokolov

December 12, 2017

Contents

Abstract

The thesis is concerned with the study of particles by impact voltammetry. The use of the particle-impact technique is developed and extended beyond quantitative sizing of spherical metallic nanoparticles to complex systems involving quasi-spherical nanoparticles, reversible agglomeration processes and extremely low levels of analyte. Initially the assumption that the particles are spherical is challenged and a system of quasi-spherical citrate-capped nanoparticles has been analyzed. The combination of SEM imaging and electrochemical nano-impact experiments was demonstrated to allow sizing and characterization of the geometry of single silver nanoparticles and determine an icosahedral geometry.

Next the agglomeration/aggregation state of silver nanoparticles is studied in a media of high ionic strength. Distinguishing agglomeration (reversible clustering of the particles) and aggregation (irreversible clustering) is a challenging task for conventional techniques, especially at arbitrary concentrations. Using the nano-impact technique in conjunction with light scattering techniques (nanoparticle tracking analysis and dynamic light scattering) it was demonstrated that even in high ionic strength environments, particles develop equilibria between agglomerated and monomeric species, which

in practice means the transport behavior is dominated by the presence of fast-diffusing monomers with high chemical reactivity.

Having developed an understanding of the agglomeration and aggregation state of the particles and underlying mass transport, the causes of agglomeration were considered and developed using the idea of entropy of mixing driven clustering, a concept hitherto unexplored and an entirely new perspective. Through the use of maximization of entropy of mixing the expected agglomeration population in the absence of any enthalpy effects and the contribution to the entropy from the formation of dimers, trimers etc., was predicted even though their formation causes an overall reduction in particle numbers. For a system of citrate-capped silver nanoparticles entropy was shown to play a dominant role in the observed size distributions. The distribution predicted by the model and the experimentally observed particle size distributions demonstrated the strong entropy contribution.

The last chapter is concerned with the design of an approach for the most sensitive electrochemical detection of nanoparticles, yet realized. The limit of detection is dependent on the mass transport of the particles to the electrode and the electroactive area of the electrode. The use of a hydrodynamic wall-jet flow causes high mass transport. Larger electroactive area increases the observed current magnitude but in order to detect individual particles low capacitance is a required and as a result traditional macroelectrodes cannot be used. Hence in order to increase the surface area and reduce the associated increase in capacitance we chose to use a random assembly of microelectrodes (RAM) which consist of hundreds of carbon fiber microelectrodes connected in parallel to a current collector, which results in large electroactive area and

relatively low capacitance. Using this in-house manufactured cell we were able to demonstrate femtomolar (10^{-15} M) limit of detection for 50 nm silver citrate-capped nanoparticles, which is substantially the lowest limit detection reported in the literature to date.

Acknowledgements

I owe a debt of gratitude to Prof. Richard Compton, who gave me an opportunity to learn experimental and theoretical aspects of electrochemistry. Without his support this thesis would not have been possible. I particularly enjoyed our trips to international conferences and the unforgettable visit to Tomsk. The atmosphere of the group he created, including the social aspects, really made my time in Oxford enjoyable and memorable.

I would like to thank Enno Kätelhön, Kristina Tschulik, and Christopher Batchelor-McAuley for guiding me through different facets of electrochemistry and each providing unique perspective. Many thanks to my imaging collaborators: Neil Young and Jennifer Holter; many images were taken and much time spent at the microscope. I would also like to thank Jeffrey Poon, Thomas Bartlett and Shaltiel Eloul, who have been amazing friends, we shared a great number of coffees, while discussing all exciting/frustrating sides of electrochemistry. A very special gratitude goes out to Lior Sepunaru for our insightful life discussions and his guidance. Finally thanks to all Compton group members, past and present: Blake, Giorgia, Dia, Eden, Crystal, Hannah, Chuhong, Xiuting, Wei, Alex and many others.

I dedicate this thesis to my family (Lina, Tatiana, Mikhail, Lorraine)

and my late grandfather Victor Sokolov, who always supported my desire for knowledge, wanted me to study in England, and made it all possible.

"We are trying to prove ourselves wrong as quickly as possible, because only in that way can we find progress." -**Richard P. Feynman** *(1918-1988)*

Chapter 1

An introduction to electrochemistry

In this chapter the fundamental components of an electrochemical system are discussed and a theoretical background is presented necessary for understanding of the concepts covered in the present thesis. For more detailed and comprehensive treatment of electrochemical concepts the reader is referred to the textbooks Understanding Voltammetry [1] and Electrochemical Methods: Fundamentals and Application [2], which provide meticulous overviews of the field of electrochemistry and an excellent foundation for further research.

1.1 Major symbols and abbreviations

Listed below are symbols used throughout this thesis. Table **??** shows the Roman symbols used for variables, Table 1.2 shows the Greek Symbols used for the variables, and Table 1.3 shows the common abbreviations used in the

present thesis.

Table 1.1: Roman symbols used in the present thesis

Symbol	Definition	Usual Units	Chapter
A_{mol}	Absorbance of a Sample	none	2
A_r	Atomic Mass	$g\ mol^{-1}$	2
A	a) Area	m^2	1,3,4,5,7,8
	b) Frequency factor in a rate expression	Depends on order	2,7
$C_{j(x=0)}$	Concentration of Species j at the electrode	$mol\ m^3$	1,7
C_j	Concentration of Species j	$mol\ m^3$	1,7
c^*	Bulk concentration	$mol\ m^3$	1,3,4,5,8
c	Speed of light in vacuum	$m\ s^{-1}$	2
D_∞	Diffusion Coefficient at infinite dilution	$m^2\ s^{-1}$	1
D_x	Diffusion Coefficient of species x	$m^2\ s^{-1}$	1,2,3,4,5,6,7
E_{exp}	Experimentally Measured Potential Different	V	1,
E^0	Standard Potential of an Electrode or Couple	V	2
f_H	Henry Function	none	2
F	a) Faraday Constant	96487 Coulombs	1,2,3,4,5,7,8
	b) Flux of electroactive species	$mol\ m^{-2}\ s^{-1}$	1
f	Rotation Frequency		1,7
G	Gibbs Free Energy	$kJ\ mol^{-1}$	1,6
h	Planck constant	$J\ s$	1
I_0	Incident Intensity	cd	2
i_p	Peak Current	A	2
i_t	Current at Time t	A	1
I	Transmitted Intensity	cd	2
k_0	Standard Heterogeneous Rate Constant	$m\ s^{-1}$	1,7
k_B	Boltzmann Constant		1
k_x	Heterogeneous Rate constant of a Reaction x	$m\ s^{-1}$	6
m_e	Rest mass of an electron	kg	2
N_A	Avogadro's constant	mol^{-1}	1,2,3,4,5,8
n	Refractive Index of a media	none	2
p	Momentum of a particle	$kg\ m^{-1}\ s^{-1}$	2
q	Scattering Vector	none	2
$R_{circumscribed}$	Ratio between the volume of the solid and circumscribed sphere	none	3
R_{elec}	Radius of wall-jet electrode	m	1,8
r_{nm}	Radius of a Nanoparticle	m	2,3,4,5,6,7,8
r_{sphere}	Radius of a Sphere	m	1
R_e	Reynolds Number	none	1
R_s	Solution Resistance	Ω	1
R	Gas Constant	$J\ mol^{-1}\ K^{-1}$	1
T	Temperature	K	1,2,3,4,5,7,8
t	Time	s	1
$V_{(x,y,z)}$	Velocity Flow Profile	none	2,7
$V_{polyhedron}$	Volume of a polyhedron	m^3	3
V_{sphere}	Volume of a sphere	m^3	3
v_x	Axial Flow Velocity	$m\ s^{-1}$	
v	a) Scan Rate	$V\ s^{-1}$	2
	b) Kinematic viscosity	$kg\ m^{-1}\ s^{-1}$	1,7
x_{DL}	Debye Length	m	1
x	Perpendicular Distance from the Electrode	m	7
Z_D	Hydronamic Mean Radius	m	2
Z_j	Charge of Species j	none	1

Table 1.2: Greek symbols used in the present thesis

Symbol	Definition	Usual Units	Chapter
α	Cathodic Transfer Coefficient	none	1
$\bar{\mu}_j^0$	Standard Electrochemical Potential of Species j	$kJ\ mol^{-1}$	1
β	Anodic Transfer Coefficient	none	1
δ_0	Hydrodynamic Layer Thickness	m	2,7
δ	Nernst Diffusion Layer Thickness	m	1
ϵ	Molar Extinction Coefficient	$M^{-1}\ m^{-1}$	2
η	Viscosity	$Pa\ s$	2
Γ	a) Gamma function	none	1,7
	b) Surface coverage of an adsorbate	$molecules\ m^{-2}$	1
γ_j	Activity Coefficient of a species j	none	1
γ	Surface Tension	$N\ m^{-1}$	2
μ_e	Electrophoretic Mobility	$mol\ m^{-2}$	2
μ_j^0	Standard Chemical Potential of Species j	$kJ\ mol^{-1}$	1
ω	Angular Frequency of Rotation	s^{-1}	1,7
ϕ_x	Electrostatic Potential of a medium	V	1
ρ	Bulk metal density	$kg\ m^3$	2,3,4,5,8
σ	Standard Deviation of the distribution	none	2,3,4,5,6,7,8
λ	Wavelength	m	2
ε_0	Permitivity of Free Space	$C^2\ N^{-1}\ m^{-2}$	1
ε_r	Dielectric Constant of a Medium	none	1

Table 1.3: Abbreviations used in the present thesis

Abbreviation	Meaning	Chapter
APTES	3-Triethoxysilylpropylamine	2
BV	Butler-Volmer	1,5
CCD	Charge-coupled Device	2
CE	Counter Electrode	1,3,4,5,8
CFT	Colloidal Filtration Theory	7
CTAB	Cetyl trimethylammonium bromide	2
CV	Cyclic-Voltammetry	1,3,4,5,8
DLS	Dynamic Light Scattering	2,5,6,8
DLVO	Derjaguin, Landau, Verwey, and Overbeek	5
EDX	Energy Dispersive X-ray	2
EPI	Electrode Particle Impact	9
GC	Glassy Carbon	2,3,4,5
IHP	Inner-Helmholz Plane	1
IUPAC	International Union of Pure and Applied Chemistry	3,4,5,6
LSRP	Localised Surface Plasmon Resonance	2
NP	Nanoparticle	2,3,4,5,6,7,8
NTA	Nanoparticle Tracking Analysis	2,4,5,6
OHP	Outer-Helmholz Plane	1
PdI	Polydispersity Index	2
PEEK	Polyether Ether Ketone	8
PEG	Polyethylene Glycol	2
PZC	Potential of Zero Charge	2
RAM	Random Assembly of Microelectrodes	3,4,8
RDE	Rotating Disk Electrode	1
RE	Reference Electrode	1,3,4,5,8
RRDE	Rotating Ring-Disk Electrode	1,7
SCE	Saturated Calomel Electrode	1,2,3,4,5,8
SEM	Scanning Electron Microscopy	2,3,4,5
SHE	Standard Hydrogen Electrode	1,3,4,5,8
STEM	Scanning Transmission Electron Microscopy	2
TEM	Transmission Electron Microscopy	2
UV-vis	Ultraviolet-Visible	2
WE	Working Electrode	1,3,4,5,8

1.2 Thermodynamics

Electrochemical systems involve a combination of three fundamental components: thermodynamics, kinetics and mass transport. It is insightful to

study these aspects separately. Classical thermodynamics is concerned with systems at equilibrium and allows one to predict the direction of a chemical reaction, but not its rate. [3] The following general reaction is considered:

$$aA + bB \rightleftharpoons cX + dY \tag{1.1}$$

The most useful thermodynamic quantity for chemical reactions is the Gibbs energy (G) of the system which corresponds to the maximum amount of reversible work that may be performed by a given system at constant pressure and temperature. [4] At equilibrium the thermodynamic system achieves mimimisation of the Gibbs energy in accordance with Equation 1.2 and the sum of chemical potentials of reactants (A,B) is equal to the chemical potentials of the products (X and Y).

$$dG_{sys} = 0 \tag{1.2}$$

The chemical potential of species j can be defined as Gibbs energy per mole of j in accordance with Equation 1.3

$$\mu_j = (\frac{\partial G}{\partial n_j})_{T,n_i \neq n_j} \tag{1.3}$$

The present work is concerned with reactants and the products in solution and the chemical potential for the solution phase species can be expressed in accordance with Equation 1.4

$$\mu_j = \mu_j^0 + RTln\frac{[j]}{[\,]^0} \tag{1.4}$$

where the μ_j^0 is the standard chemical potential, R is the gas constant (8.314 $J\ mol^{-1}\ K^{-1}$), $[j]$ is the concentration of species j, $[\ ]^0$ is the standard concentration. If the reactants are pure liquids or solids the chemical potential can be approximated by the standard chemical potential in accordance with Equation 1.5

$$\mu_j = \mu_j^0 \tag{1.5}$$

Knowledge of the chemical potential allows to define a general equilibrium constant for the reaction 1.1 as

$$K_c = \frac{(\frac{[X]}{[\ ]^0})^c(\frac{[Y]}{[\ ]^0})^d}{(\frac{[A]}{[\ ]^0})^a(\frac{[B]}{[\ ]^0})^b} \tag{1.6}$$

The concept of chemical equilibrium can be extended to electrochemical reactions which involve the transfer of an electron to species A from an electrode and the formation of a product B in accordance with Equation 1.7

$$A + e^- \rightleftharpoons B \tag{1.7}$$

Provided that the number of electrons transferred between the two species is insignificantly small and the concentration is unperturbed then the two species are said to be in electrochemical equilibrium. [1,2] The transfer of an electron e^- differentiates electrochemical equilibria from chemical equilibria discussed earlier. [5] The electron transfer at the electrode leads to charge separation and causes the establishment of difference in potential. The position of equilibrium between the products and reactants is no longer simply dependent on the chemical potential of the species but is a function of the

chemical potential μ_j and the electrical energy of the species in a given phase. The electrochemical potential is defined in accordance with Equation 1.8

$$\bar{\mu}_j = \mu_j + Z_j F \phi \tag{1.8}$$

where Z_j is the charge of the species, F is the Faraday constant (96487 Coulombs) and corresponds to the charge of one mole of electrons and ϕ is the potential of a particular phase (solution or electrode) in which the reacting species is found. As a result the electrochemical equilibrium shown in Equation 1.7 can be expressed in terms of the equality of the electrochemical potentials of the reactants and the products.

$$\bar{\mu}_A + \bar{\mu}_{e^-} = \bar{\mu}_B \tag{1.9}$$

The substitution of Equation 1.4 into Equation 1.9 yields the Nernst equation for a single electrode-solution interface [6]:

$$\Delta\phi = \phi_m - \phi s = \frac{\Delta\mu^0}{F} + \frac{RT}{F} ln[\frac{[A]}{[B]}] \tag{1.10}$$

where $\Delta\phi$ is the potential difference, ϕ_M and ϕ_S are the electrical potentials of the electrode and the solution and:

$$\Delta\mu^0 = \mu_B^0 - \mu_A^0 - \mu_{e^-}^0 \tag{1.11}$$

where the potential drop at the interface is expressed in terms of standard chemical potentials. Practical experimental measurements require a complete

electric circuit in order to measure the potential difference and lead to a creation of two electrode-solution interfaces at the contact points. As a result it is impossible to measure the absolute value of $\Delta\phi$ at a single interface and a second electrode is required. The first electrode of interest is traditionally referred to as a working electrode (WE) and the second electrode is known as a reference electrode. The experimentally measured potential difference E_{exp} is:

$$E_{exp} = (\phi_M - \phi_S)_{WE} - (\phi_M - \phi_S)_{RE} + IR_s \tag{1.12}$$

where $(\phi_M - \phi_S)_{WE}$ and $(\phi_M - \phi_S)_{RE}$ correspond to the two interfaces, I is the current passed, and the IR_s term is potential drop due to the resistance, R_s, of the solution. In practice the IR_s potential drop can be minimized through the use of an inert supporting electrolyte and/or decrease of the area of the working electrode. The main requirement is for the reference electrode to maintain constant potential at the interface $(\phi_M - \phi_S)_{RE}$ and historically the standard hydrogen electrode has been used. In accordance with IUPAC [7] the values should be reported against this reference electrode. The above derivation of the Nernst equation (Equation 1.10) relied on the ideal behaviour of the electrolyte solutions, which is only valid for dilute solutions, hence to extend the applicability of the model to the concentrated solutions encountered experimentally Equation 1.4 needs to be modified with activity coefficients to account for the non-ideal behaviour at higher concentrations:

$$\mu_j = \mu_j^0 + RTln\frac{\gamma_j[j]}{[\,]^0} \tag{1.13}$$

where γ is the activity coefficient of species j. For concentrated solutions γ_j

deviates from unity and the degree of deviation acts as a measure of non-ideality and may be due to ion-solvent or ion-ion interactions. As a result as $[j] \to 0$, the chemical potential $\mu_j \to \mu_j^0$ and the solution becomes ideal. By measuring the potential difference against the standard hydrogen electrode and choosing the concentration of ions such that

$$\mu_a = \mu_a^0 \tag{1.14}$$

$$\mu_b = \mu_b^0 \tag{1.15}$$

one can define standard electrode potentials E^0 and use these values for subsequent calculations. As a result if we consider a general electrochemical equilibrium:

$$v_A A + v_B B + ...e^-(m) \rightleftharpoons v_x X + v_y Y + ... \tag{1.16}$$

where v_A are the stoichiometric coefficients, the measured potential difference can be expressed as:

$$E = E^0(\frac{A, B...}{X, Y}) + \frac{RT}{F} ln(\frac{\gamma_A^{v_A}\gamma_B^{v_B}[A]^{V_A}[B]^{V_B}...}{\gamma_X^{v_X}\gamma_Y^{v_Y}[X]^{V_X}[Y]^{V_Y}...}) \tag{1.17}$$

Unfortunately such measurements are often difficult to perform experimentally since the activity coefficients γ_j are often unknown and it is difficult to determine the concentration dependence of the coefficients. As a result the formal potential is defined as:

$$E_f^0(\frac{A, B...}{X, Y...}) = E^0(\frac{A, B...}{X, Y...}) + \frac{RT}{F}(\frac{\gamma_A^{v_A}\gamma_B^{v_B}...}{\gamma_Y^{v_Y}\gamma_Y^{v_Y}}) \tag{1.18}$$

As a result the measured potential can be expressed as:

$$E = E_f^0(\frac{A, B...}{X, Y...}) + \frac{RT}{F} ln(\frac{[A]^{V_A}[B]^{V_B}...}{[X]^{V_X}[Y]^{V_Y}...}) \tag{1.19}$$

1.3 Double Layer

In the previous section the potential drop at the interface has been discussed from a thermodynamics point of view. In order to fully understand the electrochemical processes taking place at the electrode it is necessary to evaluate the spatial distribution of this drop ($\phi_M - \phi_S$). [8] If the electrode is charged, the ions in the solution will experience attraction or repulsion depending on their respective charge and form "layers" of solution species at the interface. [9] The attracted ions have finite size and consequently finite solvation. Depending on the identity of the species they can chemically interact with the electrode and form chemical bonds. The layer closest to the electrode is known as the compact or Stern layer [10] and consists of specifically adsorbed ions or molecules. The Inner-Helmholz Plane (IHP) is defined as the distance from the centre of these specifically adsorbed ions to the electrode surface. After the IHP there is an additional layer of strongly bound adsorbed solvated ions, which are not free to move and this layer is known as the Outer-Helmholz Plane (OHP). The steepest potential drop is confined to the Inner and Outer-Helmholz Planes. Further from the OHP the ions still experience electrostatic force but are free to move under thermal forces; this layer is known as the 'diffuse layer'. The "thickness" of the layer is described by Gouy-Chapman [11] theory and is also known as the Debye length

(x_{DL}) [9]:

$$x_{DL} = \sqrt{\frac{\varepsilon_r \varepsilon_0 k_B T}{2 N_A e^2 I}} \tag{1.20}$$

where ε_r is the dielectric constant, ε_0 is the permittivity of free space, k_B is the Boltzmann constant, T is the temperature, N_A is the Avogadro constant, e is the electronic charge, I is the ionic strength of the electrolyte. At $25°C$ and for 1:1 electrolyte (for example KCl) Equation 1.20 simplifies to:

$$x_{DL} = 9.607 \times 10^{-9} \sqrt{\frac{1}{I}} \tag{1.21}$$

It can be seen that the thickness of the diffuse double layer is dependent on the concentration of the electrolyte. Figure 1.1 shows the effect of the electrolyte concentration on the thickness of the double layer for a 1:1 electrolyte at $25°C$ in accordance with the Equation 1.20 . As a result a large proportion of electrochemical experiments is conducted using high concentration of the supporting electrolyte (ca. 0.1 M) and the corresponding Debye length is approximately one nm in accordance with Equation 1.20. The electric field is confined to within close proximity of the electrode and the diffusing solution species experience the full interfacial potential drop and the corresponding thermodynamic driving force.

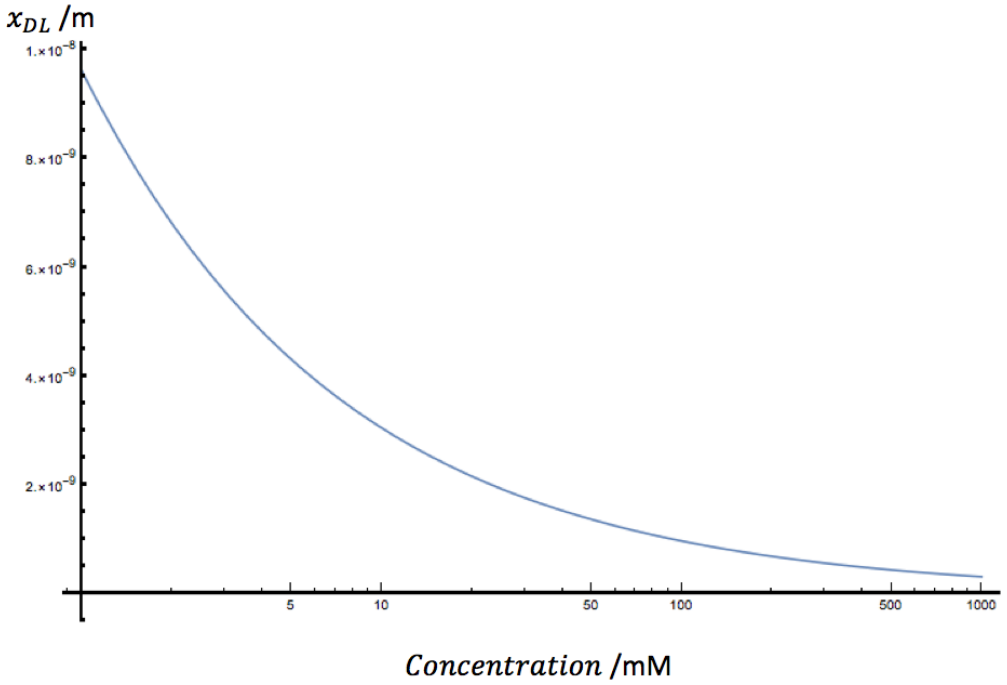

Figure 1.1: Diffuse double layer thickness as a function of concentration of 1:1 supporting electrolyte at $25.0°C$

The double layer model described above is known as the Gouy-Chapman-Stern [10] model and can be conveniently summarized on a schematic: figure 1.2 which shows the ionic distribution and the corresponding potential drop for electron transfer.

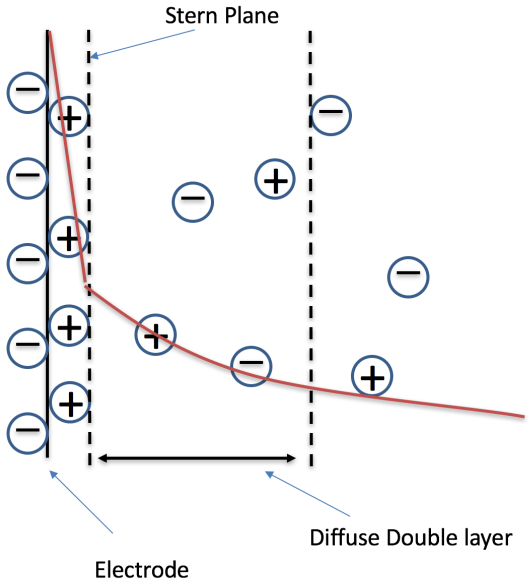

Figure 1.2: Schematic double layer structure and the corresponding potential profile as a function of the distance from the electrode surface (red line).

1.4 Electrode Kinetics

Up to the present point the electrochemical processes have been described at equilibrium. According to the Nernst equation (Equation 1.10) the potential difference and the direction of flow of electrons at the electrode-solute interface is determined by the concentration of the electroactive species. Consequently if the potential at the interface can be controlled, it is possible to shift the position of the equilibrium and the concentration of the electroactive species involved in such equilibrium. This idea is a fundamental key concept in electrochemistry and facilitates the study of a wide range of processes through variation of the applied potential. [1, 12] In order to understand how potential can be applied one can consider a Fermi level model of a metal.

Due to the overlapping of the molecular orbitals a metal has effectively continuous energy states referred to as the conduction band. [13] The electrons in this band are mobile and can be thought of as a gas. The highest occupied energy level is referred to as the Fermi level. By applying the potential externally to the metal electrode, the position of the Fermi level can be shifted with respect to the solution phase species. [2] As a result the system will shift from equilibrium and in order to compensate for the change, the concentration of electroactive species will change at the interface until the new equilibrium position is reached. Figure 1.3 shows the process schematically using an energy diagram: a) initially the system is at equilibrium and the rates of forward and backward electron transfer are equal as the Fermi level of the metal is equal to the highest occupied molecular orbital of the reacting species, b) then after the potential is applied such that electrons have higher energy at the metallic electrode, the shift in the Fermi level causes electron transfer from the metal to the solute species and the reaction takes place c) the potential is reversed and as a result the direction of electron transfer reverses from the solution phase species to the electrode. The applied potential perturbs the equilibrium and the system can no longer be described by the Nernst equation and kinetics of the process needs to be taken into account. In order to understand the kinetics aspect we will consider an outer sphere electrochemical reaction [14] involving a single electron transfer at the electrode:

$$\mathrm{Ru(NH_3)_6}^{3+} + \mathrm{e}^- \underset{\mathrm{k_b}}{\overset{\mathrm{k_f}}{\rightleftharpoons}} \mathrm{Ru\,(NH_3)_6}^{2+}$$

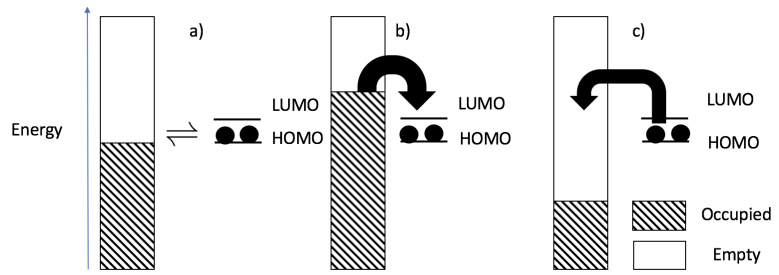

Figure 1.3: Schematic diagram illustrating the effect of an applied potential on the relative energies of the metallic electrode Fermi-level and the solution phase electroactive species.

where k_f is the rate of the reduction and k_b is the rate of oxidation. The current passed will be proportional to the flux of the electroactive species and the area of the electrode and the number of electrons transferred per reacting species:

$$I = nFAJ \tag{1.22}$$

where n is the number of electrons transferred (n=1 in the present case), F is the Faraday constant, A is the area of the electrode and J ($moles\ cm^{-2}s^{-1}$) is the flux of electroactive species. Flux is defined as:

$$J = k_f[Ru(NH_3)_6^{3+}]_0 - k_b[Ru(NH_3)_6^{2+}]_0 \tag{1.23}$$

Note that the concentration of electroactive species ($[j]_0$) is taken at the electrode surface and ignores the distance-distributed electron tunnelling. The rates of the forwards and backwards reaction are potential dependent ($k_j = f(E)$). By altering the applied potential the rates can be changed to promote either oxidation or reduction of the species of interest. Based on

the semi-empirical evidence one can propose that the rate constants depend exponentially on the applied potential:

$$k_f \propto exp[\frac{-\alpha F(\phi_M - \phi_S)}{RT}] \tag{1.24}$$

$$k_b \propto exp[\frac{\beta F(\phi_M - \phi_S)}{RT}] \tag{1.25}$$

$$\alpha + \beta = 1 \tag{1.26}$$

where α and β are the transfer coefficients for the cathodic and anodic processes respectively. Experimentally we can control the potential at the electrode (ϕ_M). Hence according to the Equations 1.24-1.25 if ϕ_M is made more positive with respect to ϕ_S the rate constant k_b will increase leading to the oxidation of $Ru(NH_3)_6{}^{2+}$ to $Ru(NH_3)_6{}^{3+}$. If the ϕ_M is made more negative with respect to ϕ_S the rate constant k_f will increase and reduction of $Ru(NH_3)_6{}^{3+}$ will be observed.

It is insightful to consider a theoretical case in which the electrode interface is at equilibrium with a solution where the bulk concentrations of both species is equal. In this system $E_{exp} = E_f^0$ and $k_f C_a^* = k_b C^*$ and consequently $k_f = k_b$. Thus E_f^0 is the potential where the forward and reverse rate constants are equal and have the same value. This value is known as standard rate constant k_0. Knowledge of the standard rate constant allows to express rate constants at other potentials in terms of k_0. [1, 2]

For convenient interpretation of experimental results we can express the rate constants in terms of the applied potential and the standard formal

potential of the redox couple:

$$k_f = k^0 exp[\frac{-\alpha F(E_{exp} - E_f^0)}{RT}] \tag{1.27}$$

$$k_b = k^0 exp[\frac{\beta F(E_{exp} - E_f^0)}{RT}] \tag{1.28}$$

The potential E_{exp} is defined in accordance with Equation 1.12. Substituting the expressions for the rate constants into the expression for flux (Equation 1.23) yields the famous Butler-Volmer (BV) equation [15] for the flux to an electrode and forms the basics of the electrochemical kinetics theory:

$$J = k^0(exp(\frac{-\alpha F(E - E_f^0)}{RT})[Ru(NH_3)_6^{3+}]_0 - exp(\frac{\beta F(E - E_f^0)}{RT})[Ru(NH_3)_6^{2+}]_0) \tag{1.29}$$

The total flux observable consists of the cathodic and anodic components.

$$J_{total} = J_c + J_a \tag{1.30}$$

This kinetic theory is based on empirical observations and does not provide justification for the magnitude of the observed rate constants but it is widely used due to relative simplicity and a small number of fitting parameters. Butler-Volmer equation relates the flux of electroactive species, applied potential, the standard electrochemical rate constants and the transfer coefficients of the electroactive species. The transfer coefficients [16, 17] (α and β) are dependent on the position of the transition state of the reactants and can be found experimentally through Tafel analysis, an experimental method which will be discussed in further detail in Section 1.7. Figure 1.4 shows the

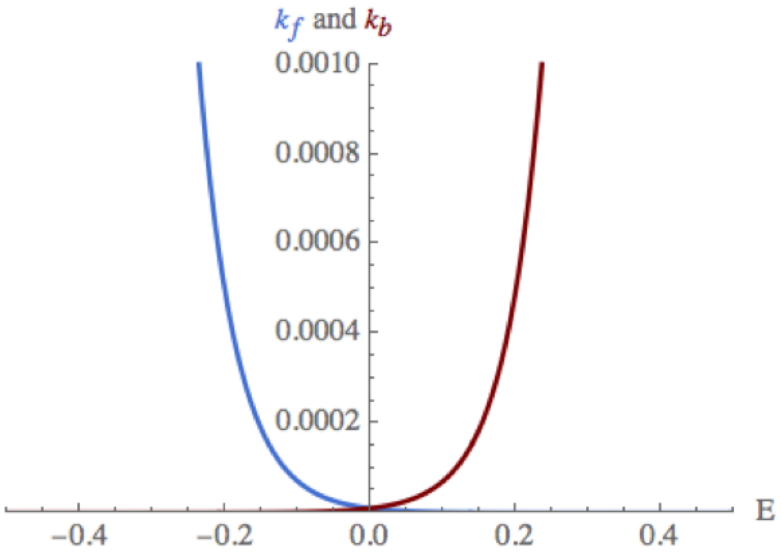

Figure 1.4: Effect of the applied potential on the rate constants and the resultant unscaled current response.

schematic dependence of the rate constants on the applied potential.

1.5 Mass transport

Having discussed the thermodynamics and kinetics of electrochemical processes it is crucial to consider the effects of the mass transport on the experimentally observed current. Up to the present point we have considered the kinetic effects on the observed rate constants and did not take the possible mass-transport limitations into account or the effect on the observed current response. In the absence of the thermodynamic and kinetic limitations, the electroactive species must be within the electron tunnelling distance of the electrode surface. The tunnelling distance cut-off is media-dependent and for aqueous systems is generally confined to 1 nm. [18] We shall consider

three major contributions to the mass transport: diffusion, convection and migration

1.5.1 Diffusion

Diffusion is a spontaneous process caused by mass transfer down the concentration gradient from high to low concentrations. The process was first postulated by Adolf Fick. [19] The equation is known as Fick's first law, which quantifies the flux through a given plane:

$$j = -D\frac{\partial c}{\partial x} \tag{1.31}$$

where D is the diffusion coefficient of a given species, $\frac{\partial c}{\partial x}$ is the concentration gradient. The negative sign is due to the fact that the mass transfer takes place down the concentration gradient. Diffusion coefficients are media and temperature dependent and generally range between 10^{-9} to 10^{-10} $m^2 s^{-1}$. The temperature dependence of the diffusion coefficients usually follows an Arrhenius type relationship [20]:

$$D = D_\infty exp(\frac{-E_a}{RT}) \tag{1.32}$$

where D_∞ is the theoretical value of the diffusion coefficient at infinite temperature. As a result it is important to conduct the experiments under thermostatted conditions. The diffusion coefficient will be dependent on the size of the diffusing species and the viscosity of the solvent. Small molecular species will move faster and consequently have higher diffusion coefficients.

As a result diffusion coefficients may be used to estimate how far species diffuse in a given period of time. For the case of one dimensional diffusion, this distance is known as root mean square displacement ($\sqrt{< x^2 >}$):

$$\sqrt{< x^2 >} = \sqrt{2Dt} \tag{1.33}$$

Figure 1.5 shows the root mean square displacement as a function of time for a molecule with a diffusion coefficient of $1 \times 10^{-9}\ m^2 s^{-1}$. It can be seen that it takes the molecule a significant time to diffuse beyond a few microns.

Fick's first law (Equation 1.31) quantifies the diffusive flux through a plane, but for practical electrochemical experiments one needs to consider the changes of concentration with time. This variation was expressed by A. Fick analogously to the one dimensional transfer of heat as:

$$\frac{\partial c}{\partial t} = D\frac{\partial^2 c}{\partial x^2} \tag{1.34}$$

and is now known as Fick's second law. Equation 1.34 is valid for planar macro-electrodes and can be extended to other geometries in three dimensions:

$$\frac{\partial c}{\partial t} = D(\frac{\partial^2 c}{\partial x^2} + \frac{\partial^2 c}{\partial y^2} + \frac{\partial^2 c}{\partial z^2}) \tag{1.35}$$

Please note that the above equations have assumed the diffusion coefficient to be isotropic an assumption valid for small molecular species. For the case of larger objects such as nano and micro-particles the diffusion coefficient can be dependent on their positions with respect to the boundaries ($D = f(x, y, z, T)$). The anisotropic case will be discussed in later chapters of this

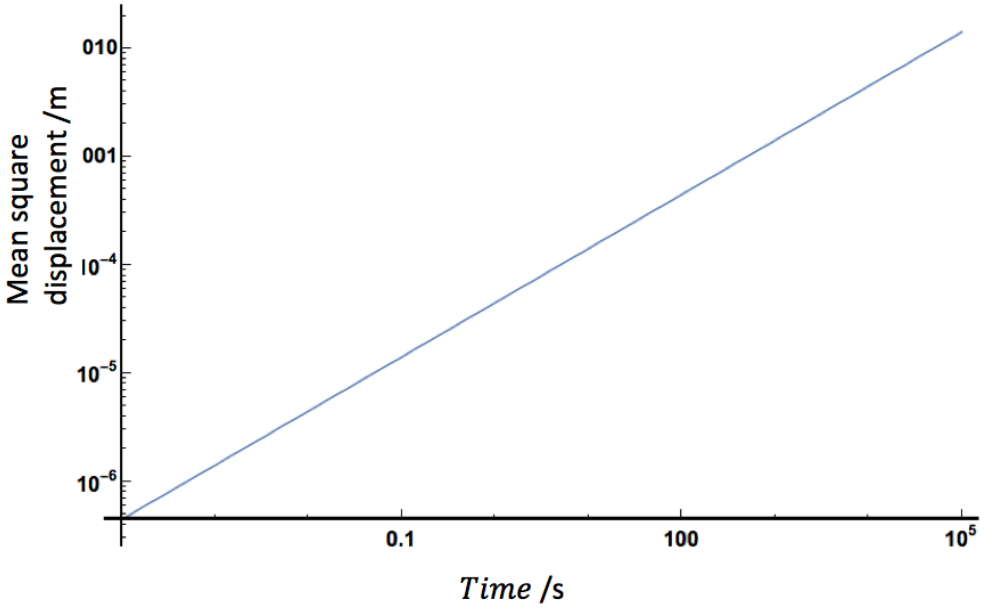

Figure 1.5: The root mean square distance as a function of the diffusion time

thesis.

1.5.2 Migration

It has been discussed in Section 1.3 that in the absence of the supporting electrolyte the electric field can extend a significant distance (few microns) into the solution. As a result a charged electroactive species will experience a force based on their respective charges and position and may be attracted or repelled. [9,21,22] This phenomenon is known as migration and is accounted for in the flux expression by introduction of an additional term which relates the charge of the species, and of the electric field:

$$j = -D(\frac{\partial c}{\partial x} + \frac{[i]ZF\partial\phi}{RT\partial x}) \tag{1.36}$$

where $[i]$ is the concentration of the electrolyte $\frac{\partial \phi}{\partial x}$ is the electric field. Under an assumption that no specific ion adsorption takes place, the variation of the electric field with distance is given by [2, 9]:

$$tanh(\frac{1}{2}\theta) = \frac{1}{2}sinh(2\theta_0) \times e^{-x/x_{DL}} \tag{1.37}$$

where $\theta_0 = \phi_M - \phi_S$, x is the distance from the electrode and x_{DL} is defined in accordance with Equation 1.21. As a result the addition of the supporting electrolyte compresses the double layer and leads to the potential drop being confined to within close proximity of the electrode. In effect the contribution of the migration term is minimized and the system can be adequately described by the diffusion-only model. As a result experimentally one encounters 20-100 mM concentration of supporting electrolyte being used. A potential problem with the use of high concentrations of supporting electrolyte are the impurities which may interfere with the measurements.

1.5.3 Convection

An additional form of mass transport apart from diffusion and migration is convection. Convection can be divided into two categories: natural and forced. We will discuss the distinction between the two and the experimental methods which utilise convection as a means of increasing mass transport.

Natural convection

In a static solution thermal gradients are likely to arise. Species will respond by moving from areas of high to low density and will affect the distribu-

tion of the electroactive species. [23] These gradients are exceedingly hard to model and very sensitive to the experimental vessel geometry. An additional consideration is the density gradient which may develop as a result of a reaction at the electrode surface when there is a difference in density between the products and reactants. [24] As a result, thermostatting is used to minimize such effects and the duration of voltammetric measurements is typically limited to less than one minute.

Forced convection

The distance travelled by the diffusing species is exceedingly small on the time-scale of an electrochemical experiment ($t < 1$ min) according to Equation 1.33. As a result it is often advantageous to increase the rate of mass transport in order to be able to detect lower concentrations of the analyte and eliminate the effects of unwanted natural convection. An obvious solution to the problem is a form of physical agitation by mechanical means. The key design requirements of such hydrodynamics system are a well-defined, reproducible flow, amicable to the theoretical modelling. The solution flow transports the electroactive species to the electrode and causes an increase in flux. By adjusting the rate of flow mass transport can be effectively controlled, thereby allowing the study of wide range of reaction time-scales. Please note that within close proximity to the electrode there exists a stagnant solution layer, where diffusion is still the dominant mode of mass transport. The most general statement relating diffusion, forced convection and flux is given by:

$$j = -D \bigtriangledown c + cV(x, y, z) \tag{1.38}$$

where $\bigtriangledown$ is the differential operator $\bigtriangledown = \frac{\partial}{\partial x} + \frac{\partial}{\partial y} + \frac{\partial}{\partial z}$ and $V(x, y, z)$ is the flow profile which also depends on the geometry of a given system. One of the most challenging aspects of this equation involves the modelling of the flow profile $V(x, y, z)$. As a result we can include the forced convection term in Fick's second law (Equation 1.34) and determine the change of concentration with time:

$$\frac{\partial c}{\partial t} = D \bigtriangledown^2 c - V(x, y, z) \bigtriangledown c \tag{1.39}$$

To date multiple experimental approaches have been reported: rotating disk and rotating ring-disk (RDE and RRDE) [25], channel flow [26] and wall-jet electrodes. In the present thesis we will discuss the rotating disk and wall jet electrodes.

1.6 Electrode Design

In the present section common types of electrodes used in the present thesis are discussed. Electrodes can be separated into two broad categories: stationary and hydrodynamic, and feature different modes of mass transport.

1.6.1 Stationary Electrodes

Macroelectrodes

Macroelectrodes have long been the electrodes of choice due to simple mass transport (effectively 1-D diffusion) and relative simplicity of the manufacturing procedure. [27] Typically, an electroactive disk with a radius of 2-6 mm is embedded within a polymeric matrix and polished to mirror finish. The

most common electroactive substrates are: gold, platinum and glassy carbon. The advantages of microelectrodes is that the surface can be re-polished thereby ensuring reproducible surface prior to experimental measurements. The main disadvantage is the slow mass transport which limits their use to electrochemical reaction with small values of the standard electrochemical rate constant (k_0).

Microelectrodes and arrays of microelectrodes

With the development of low-noise electronics, efficient Faraday cage shielding and fast numerical simulation methods, microelectrodes have steadily gained popularity. As will be discussed in Section 1.7.2, as the size of the electrode decreases radial diffusion becomes significant, yielding higher mass transport rates. As a result faster reaction time scales can be accessed. The most common design involves a microdisk with a radius of 1-50 μm embedded in a non-conductive resin. For higher signal to noise ratio, arrays of microelectrodes have been designed, which involve multiple microelectrodes in periodic or random arrangements. Numerous ways of manufacturing arrays have been developed including such methods as: patterned electrodeposition, [28] photolithography, [29] screen-printing. [30] The present thesis will be mainly concerned with the use of random assembly of microelectrodes (RAM) which involves hundreds of carbon fibers dispersed in resin, connected in parallel to a current collector.

1.6.2 Hydrodynamic Electrodes

Rotating Disk Electrode

Despite being over sixty years old, [25, 31] a rotating disk electrode (RDE) remains one of the most popular hydrodynamic approaches to study kinetic processes. The rotating disk in a large volume of solution acts as a 'pump' and pulls the solution to the electrode surface and a well-defined flow is developed. The flow regime is dependent on the frequency of rotation, size of the electrode and the viscosity of the solution. Most experiments are conducted under laminar flow conditions using rotation frequencies up to 2000 Hz. Under such conditions there is a predominant velocity in the main direction of flow. At higher rotation rates the flow undergoes irregular fluctuations, may develop vortices and is exceedingly hard to model theoretically and the flow becomes turbulent. The change in the flow behaviour occurs at a critical Reynolds number ($R_e \approx 2 \times 10^3$) [25, 32, 33] defined as:

$$R_e = \frac{fr^2}{v} \tag{1.40}$$

where f (Hz) is the rotation frequency, r (m) is the radius of the disk and v $(kg\ m^{-1}s^{-1})$ is the kinematic viscosity. The complete hydrodynamics description of the rotating disk involves three components: radial, azimuthal, and axial velocities. The solution to the velocity flow profiles ($V(x, y, z)$) at the RDE were provided via integral approximation by Von Karman [34] and numerically by Cochran. [35] Within close proximity to the electrode the radial flow contribution is negligible, and only the axial velocity needs to be

taken into account. According to this solution at the disk surface there exists a relatively stagnant solution layer. This layer is known as the hydrodynamic layer, and its thickness is defined as:

$$\delta_0 = 3.6\sqrt{\frac{\upsilon}{2\pi f}} \tag{1.41}$$

The axial velocity v_x is a function of separation distance x from the rotating electrode and is given by:

$$v_x = \sqrt{\upsilon\omega}(\frac{-0.51\omega x^2}{\upsilon} + \frac{\omega^{3/2}x^3}{3\upsilon^{3/2}} - ...)\ for\ x < \delta_0 \tag{1.42}$$

$$v_x = -0.886\sqrt{\upsilon\omega}\ for\ x > \delta_0 \tag{1.43}$$

As a result of the above analysis one can conclude that the rotating disk is uniformly accessible (a property only possessed by a select few hydrodynamic systems [36]). The flux of the solution towards the surface is independent of the radial distance from the axis of rotation. The time dependent partial differential equation describing the concentration profile of the system is:

$$\frac{\partial c}{\partial t} = D\frac{\partial^2 c}{\partial x^2} + cv_x^2\frac{\partial c}{\partial x} \tag{1.44}$$

The theoretical treatment is one dimensional and was pioneered by V. Levich [37, 38]. Levich solved Equation 1.44 under the assumption of steady-state ($\frac{\partial c}{\partial t} = 0$), using the first term approximation of the series given in Equation 1.42 and derived the concentration profile of the reactants, given by Equation

1.45:

$$c(x) = \frac{\gamma\left(\frac{1}{3}, \frac{0.51\omega^{3/2}x^3}{3Dv^{1/2}}\right)}{\Gamma\left(\frac{1}{3}\right)}c^* \tag{1.45}$$

where Γ and γ are the full and incomplete Gamma functions respectively. The partial derivative at the electrode surface ($\frac{\partial c}{\partial x}|_{x=0}$) yields an expression for the limiting current:

$$I_{lim} = 1.554nFAD^{2/3}v^{-1/6}\omega^{1/2}c^* \tag{1.46}$$

Wall-jet electrode

The rotating disk electrode involves multiple mechanical parts and can have potential noise problems due to the coupling of the motor and the electrochemical cell. In addition a large volume of solution is required to ensure laminar flow, although note that designs have been proposed which allow smaller volume of solution to be used [39]. An alternative approach involves forcing the solution to the electrode via the use of a pump. The flow and electrochemical components are decoupled and lower electrical noise will be observed. The wall-jet electrode is based on the stationary disk electrode submerged in a solution containing the electroactive species and a jet is directed at the electrode surface. The resultant 'umbrella' flow profile provides a steady supply of electroactive species to the electrode. The observed current response will be dependent on the diffusion coefficient of the species, viscosity of the solution, flow velocity (V_f), nozzle diameter(a), separation distance (d) and the radius of the electrode R_{elec}. In practice provided that the separation distance is sufficiently small, the current response is virtually

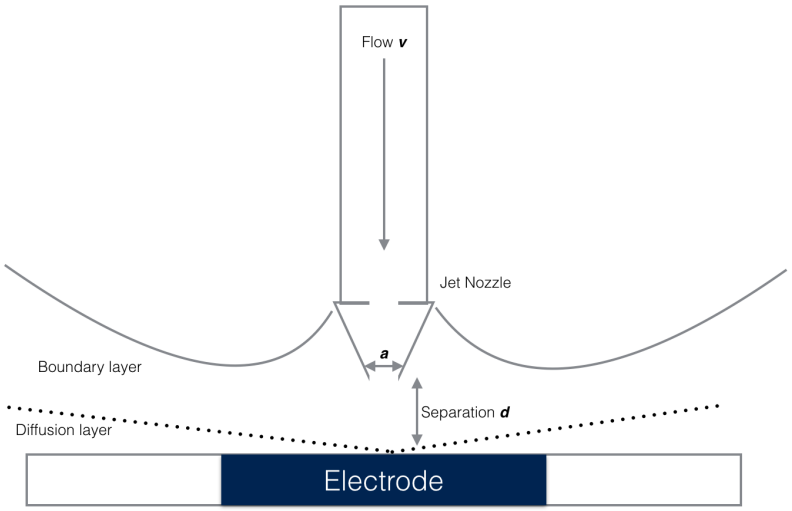

Figure 1.6: Flow profile at a wall-jet electrode

independent of it. The schematic structure is shown in Figure 1.6 and demonstrates the key components and distances. The limiting current response is given by [1]:

$$I_{lim} = 1.35nFD^{2/3}v^{-5/12}a^{-1/2}R_{elec}^{3/4}V_f^{3/4}c^* \tag{1.47}$$

The use of a wall-jet electrode allows low limits of detection of analyte and as result has found numerous applications in electroanalytical chemistry. [40] The main disadvantage is that unlike RDE, the wall-jet electrode is not uniformly accessible, the diffusion layer thickness varies as a function of a distance of separation from the axis of flow and as a result the theoretical problem requires two dimensional treatment, which hinders the mechanistic simulation of complex multistep processes. [41]

1.7 Electrochemical Methods

Having discussed the three theoretical components of an electrochemical system we next proceed to experimental measurements and the methods employed to study electroactive species. We will briefly discuss the general design of an electrochemical cell and proceed to discuss the experimental techniques used to study various aspects of an electrochemical reaction. The techniques could be split into two major categories: potentiostatic (involving control of the potential) and galvanostatic (involving the control of current passed). The present thesis will be mainly concerned with potentiostatic techniques: chronoamperometry, linear sweep and cyclic voltammetry.

1.7.1 Electrochemical Cell

In section 1.2 the necessity of having a minimum of two electrodes for electrochemical measurements was discussed. Most cells involve either two or three electrode configurations. Both types involve the working electrode (electrode at which the reaction of interest takes place) and a reference electrode against which potential is measured. It is often advantageous to have a non-chemically active, conductive WE made of materials such as gold, platinum or glassy carbon in order to avoid adsorption of electroactive species and unwanted side reactions. Traditionally the standard hydrogen electrode has been used as a reference. However since its invention in 1941 [42], the saturated calomel electrode (SCE) has gained popularity due to simplicity of operation and stable potential. The potential-determining equilibrium in an

SCE is based on the following reaction:

$$\frac{1}{2}\mathrm{Hg_2Cl_{2(s)}} + e^-_{(m)} \rightleftharpoons \mathrm{Hg_{(l)}} + \mathrm{Cl^-_{(aq)}} \tag{1.48}$$

According to IUPAC the potentials should be reported with respect to the SHE where $E^0(H^+/\frac{1}{2}H_2) = 0$ V. For an SCE the potential is +0.241 V vs. SHE at $25°C$ and remains constant providing a high fixed concentration of potassium chloride electrolyte is used. The equilibrium will also be perturbed by the passage of a large current and as a result two electrode measurements are mainly confined to micro-electrodes where the current magnitude is insufficient to affect the position of the equilibrium. In order to circumnavigate the problem, a counter electrode (CE) is introduced to facilitate the passage of current without the perturbation of the reference electrode equilibrium. As a result the potential is constant and known with respect to the reference electrode and the current passage takes place between the WE and CE electrodes. The counter electrode is usually chosen to be inert and can be separated from the rest of the solution by a frit in order to avoid contamination of the cell by the by-products. [2] Figure 1.7 shows the schematic structure of a three electrode cell. Using the three electrode cell setup, shielded by a Faraday cage to minimize the electromagnetic interference and connected to a potentiostat a wide range of measurements can be performed, highlighting the versatility of electrochemistry.

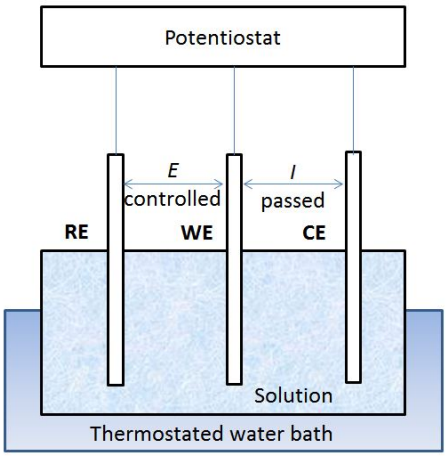

Figure 1.7: Schematic structure of a three electrode cell

1.7.2 Chronoamperometry

Chronoamperometry is one of the simplest electrochemical methods and involves a change (step) in potential from one potential E_1 to another E_2. Typically at E_1 the electroactive species are in electrochemical equilibrium with the WE and no overall charge transfer takes place. Thus initially the concentration of the electroactive species is uniform and equal to the bulk concentration (c^*). By stepping the potential to E_2, the Fermi level of the electrode is shifted and electron tunnelling can take place to/from the electroactive species as shown in Section 1.4 (Figure 1.3). As a result of an electrochemical reaction at the electrode the concentration of electroactive species will be depleted leading to an establishment of a concentration gradient with respect to the bulk solution and leading to the diffusion of species towards the electrode down the concentration gradient. If E_2 is a sufficient overpotential so that there are no kinetic limitations, the electrochemical reaction will be limited only by the mass transport of the electroactive species.

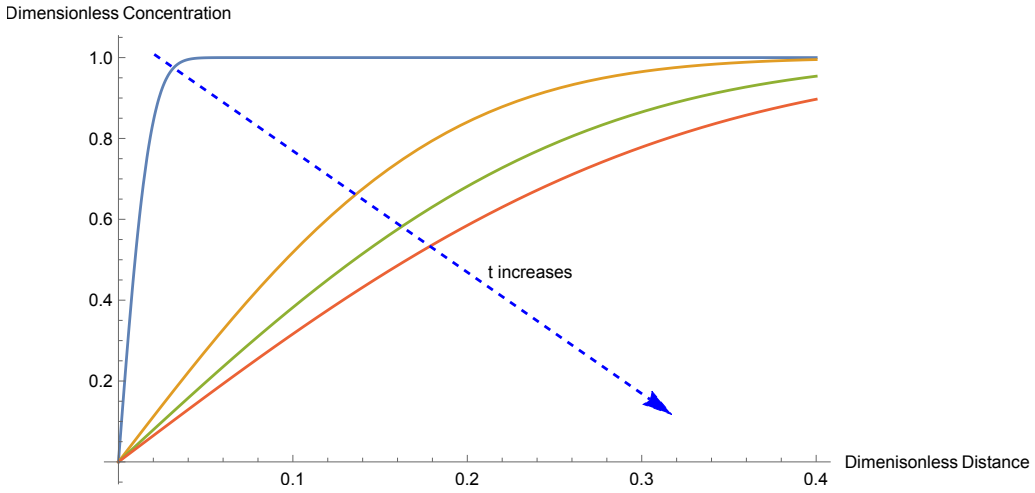

Figure 1.8: Dimensionless concentration profiles based on the solution to the Equation 1.49 as a function of separation from the electrode

Chronoamperometry at a planar geometry

For a planar macroelectrode, the current response can be predicted mathematically first by the use of the one dimensional version of Fick's 2nd law to determine the concentration profile as a result of a potential step subject to the boundary conditions:

$$\begin{aligned} &\frac{\partial c}{\partial t} = D\frac{\partial^2 c}{\partial x^2} \\ &t = 0,\ [C]_x = c^* \\ &t > 0,\ [C]_0 = 0 \quad and \quad t > 0,\ [C]_\infty = c^* \end{aligned} \tag{1.49}$$

The resultant dimensionless concentration profiles as a function of distance from the electrode are shown in Figure 1.8 at increasing time intervals. It can be seen that at longer time-scales due to the depletion of reactants, concentration gradients become shallower. The knowledge of the concentration profile as a function of time allows one to calculate the flux at the electrode

surface based on the Fick's first law (Equation 1.31)

$$j = D\frac{\partial c}{\partial x}|_{x=0} \tag{1.50}$$

By substituting the obtained flux expression into Equation 1.22 it follows that:

$$I = \frac{nFA\sqrt{D}c^*}{\sqrt{\pi t}} \tag{1.51}$$

this expression is known as the Cottrell equation [43] and allows one to predict the current response as a function of time for a large planar electrode of an area A after a potential step. Figure 1.9 shows the predicted current response. It should be noted that at infinite time ($t \to \infty$) the predicted current is zero. In reality natural convection will take place in the bulk solution due to the density gradients caused by electrolysis and an increase in the flux of the electroactive species will be observed. As a result a steady state current will be observed. One can define the solution layer thickness beyond which, the solution is well-mixed by natural convection and the concentration of electroactive species is effectively constant. This layer is known as the Nernst diffusion layer and its thickness can be linearly approximated by:

$$\delta = \sqrt{\pi Dt} \tag{1.52}$$

The Nernst diffusion layer thickness is dependent on the diffusion coefficient of the species and the time scale of the experiment. Figure 1.10 shows the Nernst layer (dashed red line) under linear approximation and the accurate concentration profile derived from Fick's second law.

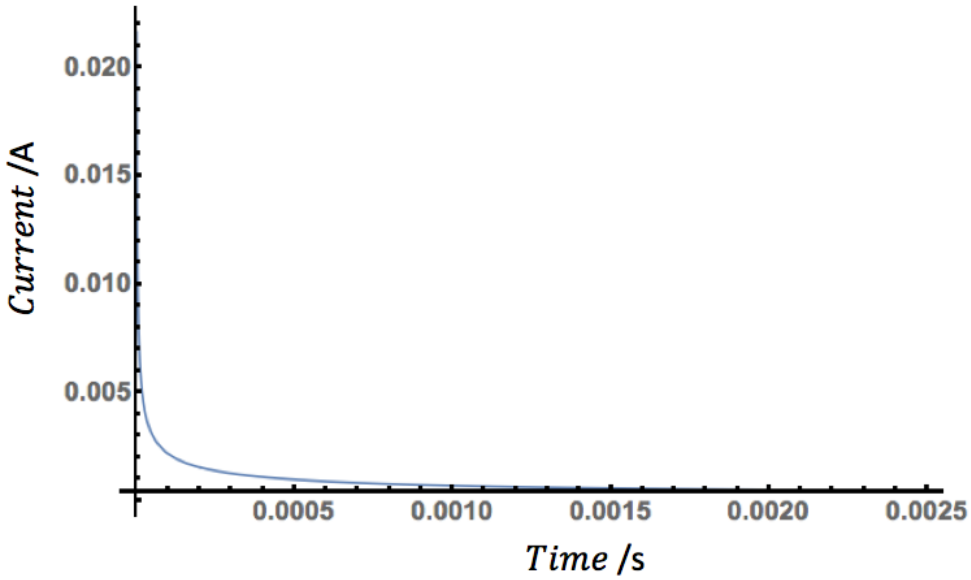

Figure 1.9: Predicted current response based on the Cottrell equation. Parameters $D = 1 \times 10^{-9} m^2 s^{-1}$, $A = 1.25 \times 10^{-5} m^2$, $c^* = 1mM$.

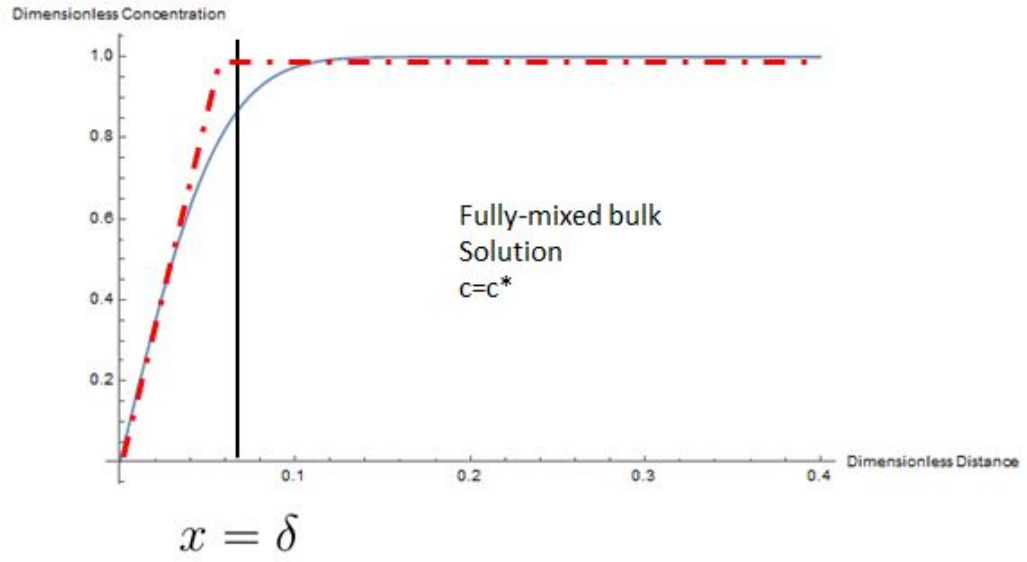

Figure 1.10: The approximate diffusion layer thickness and the true concentration profile

Chronoamperometry at alternative geometries

For a large macroelectrode provided that the area is sufficiently large the diffusion can be treated as a one dimensional problem (the edge effects are ignored). Diffusion is effectively planar. On the other hand for a spherical electrode radial diffusion is important and becomes dominant at longer timescales. As a result for such electrode, the time dependent solution to Fick's second law as a result of a potential step (Equation 1.34) yields an expression for current [44]:

$$i = \frac{nFADc^*}{r_{sphere}} + \frac{nFA\sqrt{D}c^*}{\sqrt{\pi t}} \tag{1.53}$$

where r_{sphere} is the radius of the sphere. At short time scales:

$$i_{(t\approx 0)} \approx \frac{nFA\sqrt{D}c^*}{\sqrt{\pi t}} \tag{1.54}$$

while at longer time scales ($t \rightarrow \infty$)) the radial diffusion term becomes dominant leading to an establishment of steady-state response.

$$i_{(t\rightarrow\infty)} \approx \frac{nFADc^*}{r_{sphere}} \tag{1.55}$$

Similar behaviour is observed as the size of an electrode is decreased and becomes comparable to the diffusion layer thickness, as is a case for microelectrodes ($r < 100\mu m$). The edge effects become dominant, leading to radial diffusion and steady state current is observed. The solution to the diffusion equation is complex as it involves diffusion in two dimensions and can be

obtained numerically. For a microdisk electrode numerical approximation has been provided by Shoup and Szabo for the expected current [45]:

$$i_{microdisk} = 4nFrDc^* f(\tau) \tag{1.56}$$

where

$$f(\tau) = 0.7854 + 0.8862\tau^{-0.5} + 0.2146e^{-0.7823\tau^{-0.5}} \quad \tau = \frac{4Dt}{r^2} \tag{1.57}$$

Cylindrical electrodes show an intermediate behaviour between the two extremes (planar and spherical geometries) and reach pseudo-steady state, the current response has been approximated numerically by Szabo [46, 47]:

$$i = (2\pi nFD_0C_0l)f(\tau) \tag{1.58}$$

where

$$f(\tau) = \frac{2e^{(-\frac{\sqrt{\pi t}}{20})}}{\sqrt{\pi t}} + \frac{1}{ln[(e^{-\gamma})^{0.5} + e^{5/3}]} \tag{1.59}$$

1.7.3 Linear Sweep and Cyclic Voltammetry

Chronoamperometry is the simplest experimental technique and involves a fixed step potential. However potential can be changed continuously as a function of time and the resultant current response recorded. As a result it is possible to probe the reaction at different potentials and observe the effect on the rate constants and extract kinetic parameters. Linear sweep voltammetry (LSV) and cyclic voltammetry (CV) are closely related tech-

niques and both involve a change of potential with time with a rate known as the scan rate v. The potential is swept from starting potential E_1 to final potential E_2 during linear sweep voltammetry and the reverse sweep is applies to record a cyclic voltammogram. The potential-time plots for the two methods are shown in Figure 1.11. If a triangular waveform is applied to a working electrode immersed in a solution containing redox active species, the electrochemical process can be studied by recording current as a function of potential. Initially we consider the case when only reduced form of an electroactive species is in the solution. At the start the potential is insufficient to drive the reaction and the current is effectively zero. As the applied potential becomes more positive, electron transfer from the species to the electrode takes place and the reactants become oxidised. As the species are consumed at the electrode surface, concentration gradient is established causing the species to diffuse from the bulk solution and a Nernst diffusion layer is established. The establishment of the Nernst diffusion layer leads to an observation of a peak in the current-potential plot as the mass transport is now diffusion limited. The decay current follows the Cottrell equation (Equation 1.51). As the potential is reversed the generated oxidised species are being reduced and similar process takes place. The resultant plot is referred to as a cyclic voltammogram and is shown schematically in Figure 1.12. The exact shape would be dependent on the kinetics of the process and the mass transport. Initially we will focus on voltammetry at a planar electrode, followed by a discussion of different geometries.

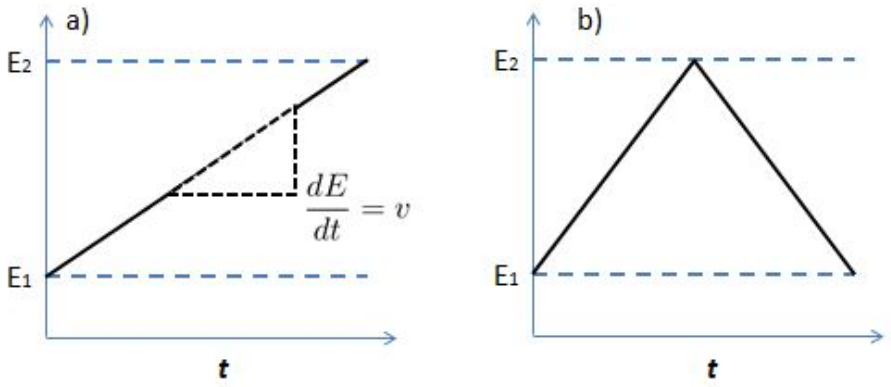

Figure 1.11: a) Linear sweep potential as a function of time b) cyclic voltammetry potential as a function of time

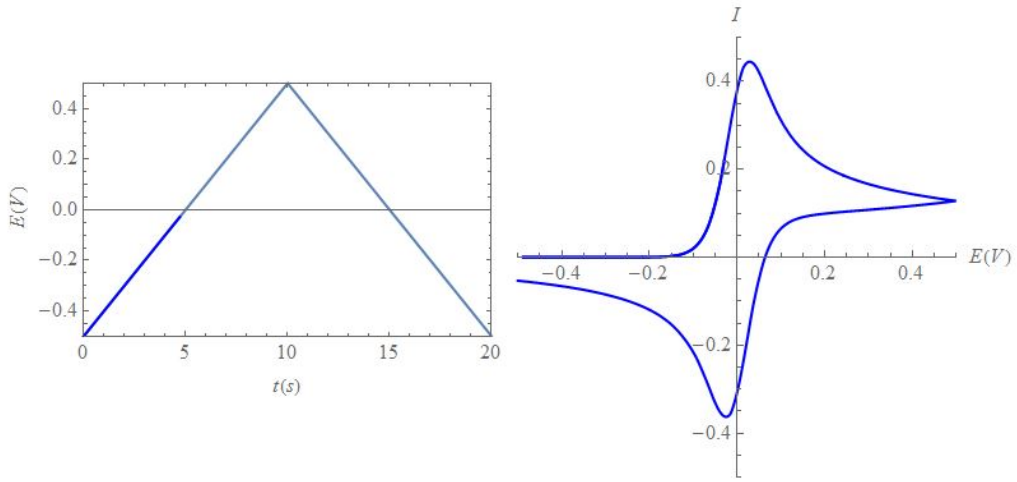

Figure 1.12: Triangular sweep applied at the working electrode as a function of time and the corresponding plot of current-potential dependence for a reversible process at a planar macroelectrode.

Voltammetry at planar macroelectrodes

It is useful to separate voltammograms into two broad categories: reversible ("fast" electron transfer kinetics) and irreversible ("slow" electron transfer kinetics). In Section 1.4 we have discussed the standard electrochemical rate constant k_0 in the context of Butler-Volmer theory which determines the rate of an electrochemical reaction. In order to classify a given reaction the standard electrochemical rate constant is compared to the rate of mass transport. For the present discussion a diffusion-only system is assumed. We define the mass transport coefficient as [1]:

$$m_T = \frac{D}{\delta} \tag{1.60}$$

where δ is the Nernst diffusion layer thickness. At a planar macroelectrode, when the potential is swept at a scan rate v the mass transport coefficient can be approximated by:

$$m_T \approx \sqrt{\frac{D}{RT/Fv}} \tag{1.61}$$

If the standard electrochemical rate constant k_0 is greater than the mass transport coefficient the process is termed reversible ($k_0 >> m_T$). When the mass transport coefficient exceeds the electrochemical rate constant, the process is termed irreversible ($k_0 << m_T$). The intermediate behaviour is known as quasi-reverisible and corresponds to cases when the standard electrochemical rate constants are of similar magnitude ($k_0 \approx m_T$). From the above discussion it is evident that control of the mass transport allows one to observe reactions at different time scales and provided that mass transport

exceeds the standard electrochemical rate constant most reactions will appear irreversible. For large planar stationary macroelectrodes it is possible to define a parameter Λ [48, 49], which allows us to classify a reaction based on the ratio of the standard electrochemical rate constant and mass transport coefficient, assuming a symmetric reactant/product barrier ($\alpha = 0.5$):

$$\Lambda = \frac{k_0}{\sqrt{\frac{FDv}{RT}}} \tag{1.62}$$

The range of values of the Λ parameter identifies the following cases:

$$Reversible: \quad \Lambda \geq 15 \quad and \quad \Lambda \geq 0.3\, v^{1/2} cm\ s^{-1} \tag{1.63}$$

$$Irreversible: \quad \Lambda \leq 10^{-3} \quad and \quad \Lambda \leq 2 \times 10^{-5}\, v^{1/2}\ cm\ s^{-1} \tag{1.64}$$

$$Quasi{-}reversible: \quad 15 > \Lambda > 10^{-3} \quad and \quad 0.3\, v^{1/2} > \Lambda > 2{\times}10^{-5}\, v^{1/2}\ cm\ s^{-1} \tag{1.65}$$

For a diffusional reversible reaction the peak current (I_p) for at a given scan rate at a planar macroelectrode can be predicted using the Randles-Ševčík equation [1, 2]:

$$i_p = 0.4463 nFAc^*(\frac{nFvD}{RT})^{1/2} \tag{1.66}$$

where n is the overall number of electrons transferred (typically 1). Experimentally a scan rate study can be conducted to test whether a given process is diffusionally controlled and extract the diffusion coefficient of the species.

For an irreversible reaction the Randles-Ševčík takes the form:

$$I_p = 2.99 \times 10^5 n(n' + \alpha)^{1/2} A D^{1/2} C v^{1/2} \tag{1.67}$$

where n is the number of electrons in an overall electrochemical process, n' is the number of electrons involved prior to the rate determining step. Prediction of the current response for an irreversible reaction requires the knowledge of the transfer coefficient α of the rate determining step. In Section 1.4 transfer coefficients were described as part of Butler-Volmer kinetics theory. Experimentally the parameter can be determined by using Tafel analysis. If we consider a simple one electron transfer reaction:

$$A + e^- \rightleftharpoons B \tag{1.68}$$

At high overpotentials the flux is predominated by one component either cathodic (J_c) or anodic (J_a) in accordance with Butler-Volmer equation (Equation 1.29), Equation 1.30 and assuming n=1. As a result:

$$J_{total} \approx J_c = k^0 exp(\frac{-\alpha F(E - E_f^0)}{RT})[A]_0, \quad when \quad E << E_f^0 \tag{1.69}$$

$$J_{total} \approx J_a = k^0 exp(\frac{\beta F(E - E_f^0)}{RT})[B]_0, \quad when \quad E >> E_f^0 \tag{1.70}$$

As a result, by plotting the natural logarithm of experimental current as a function of potential, values for α and β parameters can be extracted:

$$\alpha = -\frac{RT}{F}(\frac{\partial ln|J_c|}{\partial E}) \tag{1.71}$$

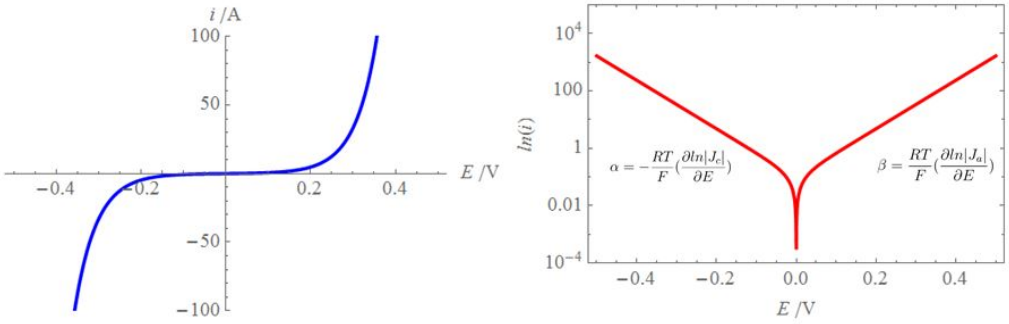

Figure 1.13: Current response and the corresponding Tafel plots for the cathodic and anodic components

$$\beta = \frac{RT}{F}(\frac{\partial ln|J_a|}{\partial E}) \tag{1.72}$$

Figure 1.13 shows the observed current response and the corresponding Tafel plots for cathodic and anodic components.

Voltammetry at alternative geometries

Up to this point the application of voltammetry has been discussed in the context of large planar macroelectrodes. However the electrode geometry has a significant effect on the mode of mass transport and by altering the geometry the rate of mass transport can be controlled leading to significantly different behaviour, as demonstrated in Section 1.7.2 using chronoamperometry. In the case of cyclic voltammetry at small spherical, hemispherical or microdisk electrodes, sigmoidal steady-state curves are observed at moderate scan rates due to highly efficient mass transport. By contrast to large macroelectrodes which have planar diffusion as a dominant mass transport, the efficient mass transport arises at spherical and microelectrodes due to convergent radial distribution. This leads to a formation of a thin diffusion layer and a steep

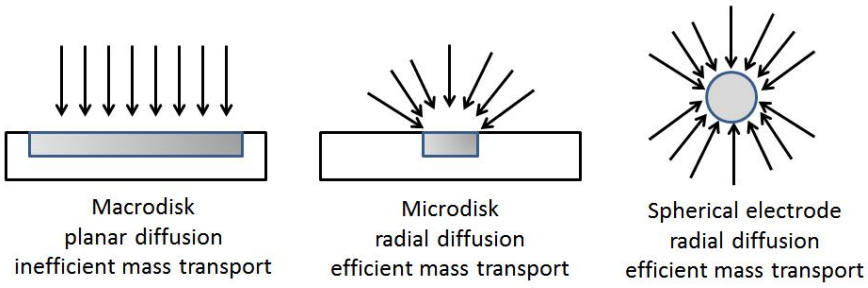

Figure 1.14: Comparison of the diffusion regimes of a macrodisk, microdisk and spherical electrodes.

concentration gradient of the electroactive species. As the electrolysis continues the diffusion layer thickness increases with time, but due to the spherical expansion more electroactive species become available. Eventually a constant diffusion gradient is established, which leads to a steady-state response. The different diffusion processes are shown schematically in Figure 1.14 for planar macroelectrode, spherical electrode and microelectrode. The shape of such curves are dependent on the standard electrochemical rate constant (k_0). The resultant sigmoidal curves can be generally described by an equation in accordance with the reaction 1.68 [50]:

$$i = \frac{4rFD_Bc_B^*}{\Theta}[1 + \frac{\pi}{K\Theta}(\frac{2K\Theta + 3\pi}{4K\Theta + 3\pi^2})] \tag{1.73}$$

where

$$K = k^0 exp(\frac{-\alpha F(E - E_f^0)}{RT}), \text{ and } \quad \Theta = 1 + \frac{D_B}{D_A} exp(\frac{nF}{RT}(E - E_0)) \tag{1.74}$$

Figure 1.15 shows the simulated effect of standard electrochemical rate constant (k_0) on the voltammograms, all other parameters being kept constant. The steady-state current magnitude for a one electron ($n = 1$) reversible reaction at these geometries dominated by convergent diffusion is given by:

$$Sphere: \quad I_{lim} = 4\pi r D F c^* \tag{1.75}$$

$$Hemisphere: \quad I_{lim} = 2\pi r D F c^* \tag{1.76}$$

$$Microdisk: \quad I_{lim} = 4 r D F c^* \tag{1.77}$$

Note that the limiting current is independent of the scan rate only at moderate scan rates, as the scan rate increases the behaviour would transition from steady-state sigmoidal waves to peaked voltammogram. The behaviour can be quantified by defining a parameter p [1]:

$$p = \sqrt{\frac{F r^2 v}{RTD}} \tag{1.78}$$

The peak-shaped voltammograms are observed when $p >> 1$ and steady state behaviour is established when $p << 1$.

The present discussion can be extended to the arrays of microelectrodes. The situation is more complex and generally requires numerical simulation due to multiple diffusion layers. [51] For an array of microelectrodes it is important to consider the separation distance (d_e) between the individual electrodes and the effect it has on the diffusion layers at different time scales. Four distinct cases can be identified for a *macro-sized* substrate and shown

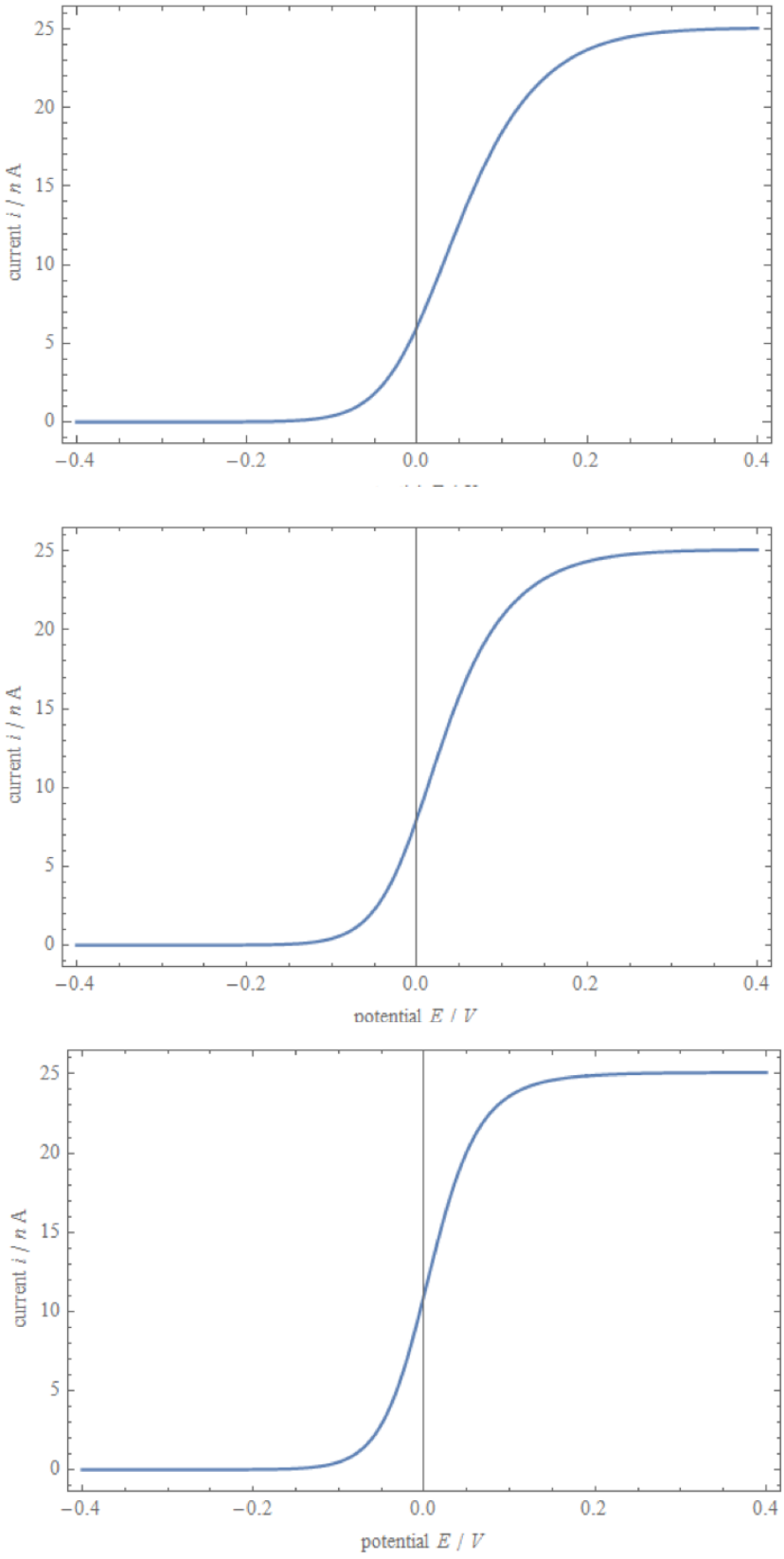

Figure 1.15: Steady state voltamograms for a microdisk electrode showing the effect of electrochemical rate constant

schematically in Figure 1.16. [1,51] In the Case 1, the scan rate is fast and the separation between the electrodes is greater than the diffusion layer thickness, as a result planar diffusion is the dominant mode of transport in accordance with Equation 1.53. The resultant voltammograms will be peaked and the overall response would correspond to the sum of individual isolated linear diffusion responses of the microelectrodes. At longer timescales or lower scan rates, the radial diffusion will become dominant and provided that the inter-electrode distance is greater than the diffusion layer thickness, the steady state response observed is proportional to the number of electrodes in a given array, this is shown schematically as Case 2. For fundamental investigations Case 2 is the most beneficial as the signal to noise ratio is increased. [52] Case 3 involves partially overlapping diffusion layers and as a result the complex response cannot be described in terms of the behaviour of an isolated microelectrode. As the interseparation distance between the electrodes decreases, complete overlap of diffusional fields takes place, which leads to the overall planar diffusion. Consequently the array behaves as a macroelectrode of an area equal to the entire geometric area occupied by the array, which includes the electroinactive spacer. Case 4 is interesting from the point of view of practical applications as the material needed to achieve the macroresponse can be significantly lower, leading to lower price point for the resultant devices especially when noble metals are used.

The above discussion relates to macro-sized substrates. If a micro-sized substrate is used, for example a relatively inert carbon microdisk electrode modified with catalytic platinum nanoparticles, a steady state response is observed even if the diffusion layers of the adjacent nanoparticles overlap

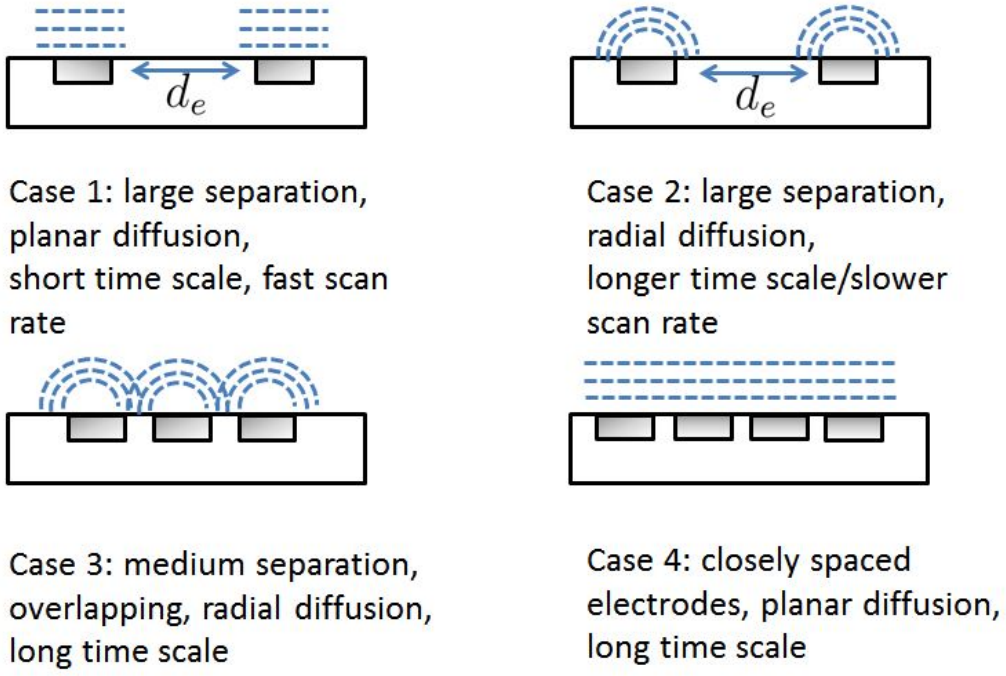

Figure 1.16: Diffusion layers at an array at different time scales and separation distances

completely. In this case, the magnitude of the observed current is expected to be slightly lower than that experienced by a microelectrode of comparable geometrical dimensions, which experiences radial diffusion when $Dt > r^2$. [53] This means that radial diffusion is even more significant for nanoelectrode arrays compared to microelectrode arrays, and hence theoretical approaches that were valid for the latter may be no longer applicable to nanoelectrode arrays of micrometric size.

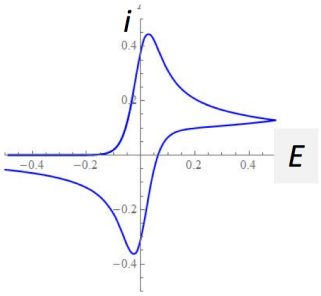

Case 1: large separation, planar diffusion, short time scale, fast scan rate, peaked CV

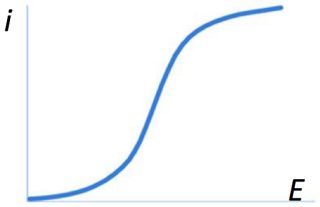

Case 2: large separation, radial diffusion, longer time scale/slower

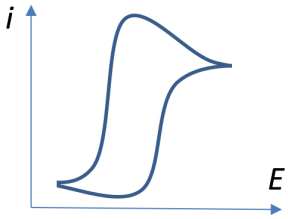

Case 3: medium separation, overlapping, radial diffusion, long time scale, mixed CV

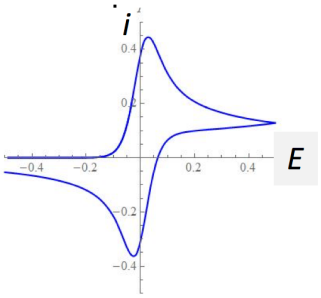

Case 4: closely spaced electrodes, planar diffusion, long time scale, peaked CV

Figure 1.17: Approximate shapes of cyclic voltammograms for the four arrays cases

Chapter 2

Nanoparticle Characterization Techniques

This chapter describes nanoparticles. Related characterization techniques will also be discussed. In the present thesis we follow the IUPAC [7] definition of a nanoparticle, which is any material with a single dimension below 100 nm. Nanoparticles have been the focus of intense research due to their novel physical properties such as the surface plasmon displayed by metallic nanoparticles, enhanced thermal conductivity and super paramagnetism. An important area of research is the energy applications of nanoparticles within batteries and fuel cells. Due to their high surface to volume ratio significant proportions of atoms are in high energy surface states. As a result nanoparticles are capable of catalysing [54] a wide range of important reactions such as the oxygen reduction [55] and hydrogen evolution reactions [56]. Understanding the physical properties requires accurate characterisation of materials being used. [57] Multiple techniques have been developed to date

to facilitate the study of nanomaterials. Many of the applications involve the nanoparticles suspended in a solution. [58] However the characterization techniques can be split into two broad categories: solution phase in situ techniques and ex situ approaches. This distinction is particularly important for biomedical applications where understanding in situ behaviour is crucial for safe and efficient applications. The main methods used in the present work are: electron microscopy (scanning electron microscopy (SEM) and transmission electron microscopy (TEM)), light scattering techniques (dynamic light scattering (DLS) nanoparticle tracking analysis (NTA) and ultra-violet visible spectroscopy (UV-vis).

2.1 Electron Microscopy

The size of the nanoparticles is below the wavelength of visible light (390-700 nm) and a shorter wavelength is required to probe their structure. Due to wave particle duality electrons can behave as waves in accordance with the De Broglie equation [59]:

$$\lambda = \frac{h}{p} \tag{2.1}$$

where λ is the wavelength, h is the Planck constant ($6.626 \times 10^{-34} Js$) and p is the momentum of the particle. As a result if an electron is accelerated by a potential difference its wavelength can be tuned. Based on the electron momentum under relativistic corrections, the wavelength of an electron under

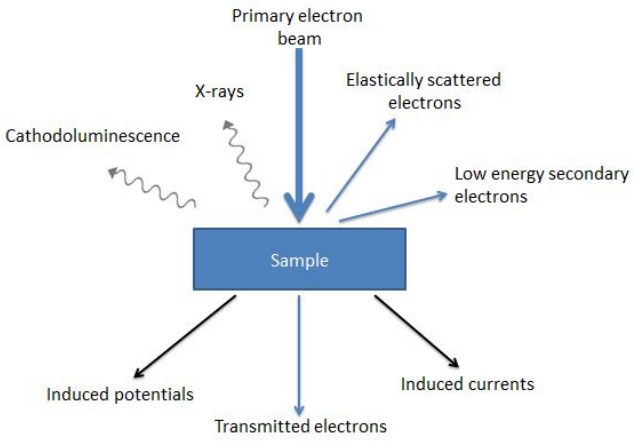

Figure 2.1: Schematic interaction of an electron beam with a sample

an applied potential difference is given by [60]:

$$\lambda = \frac{h}{(2m_e eV(1 + \frac{eV}{m_e c^2}))^{1/2}} \tag{2.2}$$

where m_e is the rest mass of an electron, e is the electron charge, V is the applied potential, c is the speed of light in vacuum. Experimentally electron wavelengths span from 2.7×10^{-11} m at an acceleration potential of 2 keV to 1.9×10^{-12} m at an acceleration potential of 300 keV. [60] When electrons collide with a sample a large range of physical interactions can take place and these are schematically shown in Figure 2.1. X-rays can be emitted by the sample due to electron beam colliding with core inner shell electrons. The x-ray energies are dependent on the elements present within the sample and can be measured using a solid-state detector. As a result the composition of the sample can be analysed and used to map the presence of different elements. Electron microscopy has been the main ex situ nanoparticle characterisation technique used due to the resulting readily interpretable visual

two dimensional information. Two broad electron microscopy techniques are widely used: scanning electron microscopy (SEM) and transmission electron microscopy (TEM). Both techniques involve the generation of an electron beam. The main difference lies in acquisition methods used and acceleration voltages employed.

2.1.1 Scanning Electron Microscopy

Scanning electron microscopy involves generation of an electron beam using a metallic filament (typically tungsten) under an applied potential bias. [61] The generated electrons are accelerated under a potential difference in vacuum and electromagnetic lenses are used to focus the beam. [62] The highly collimated electron beam is then used as a probe and moved across the sample using scanning coils and the interaction of the beam with the material analysed. The sample of interest can be mounted on most conductive substrates via a simple dropcasting, a particular advantage from the electrochemical perspective. For imaging, low energy secondary electrons are used due to high spatial sensitivity as the interaction is limited to the surface atoms. The detector is positioned at an angle above the sample. The emitted secondary electrons are attracted to a positively charged grid in front of a scintillation detector which converts the impacting electrons to visible light. The resultant image was traditionally recorded on a photographic plate but nowadays is stored digitally. The quality of the image is dependent on the energy of the electron beam and the scan rate. Figure 2.2a shows the components of an SEM instrument. Figure 2.3 shows a high resolution image of gold

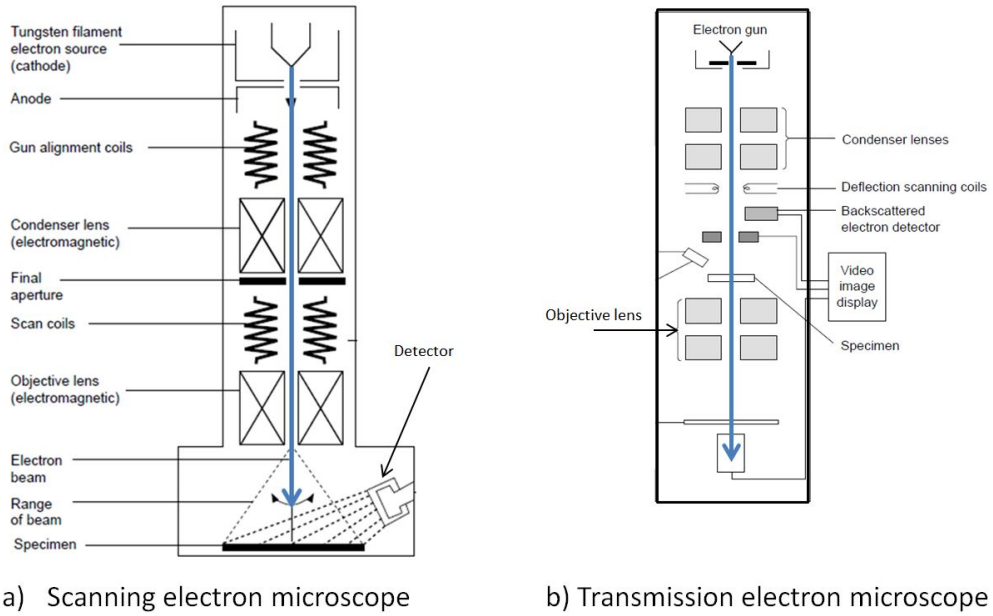

Figure 2.2: Schematic of a scanning electron microscope (a) and a transmission electron microscope (b). [63]

nanoparticles on a glassy carbon substrate. Elastically scattered electrons (ESE) have higher energies in comparison to secondary electrons and may originate deeper from within the sample ($\approx$ 100 nm). As a result the spread of the beam is higher and the spatial resolution is lower, leading to poor images. Nevertheless ESE can be used to produce an image based on the atomic number contrast. Areas of a sample containing heavy nuclei give high emissions of elastically scattered electrons and as a result appear as bright spots with areas with lighter nuclei appearing darker. SEM allows imaging of relatively large sample areas (microns in length) and can be used to study surface processes as well as bulk by etching. The lowest SEM resolution to date is approximately 20 nm. The main disadvantage of the technique is that sample must be conductive, otherwise charging effects occur leading to

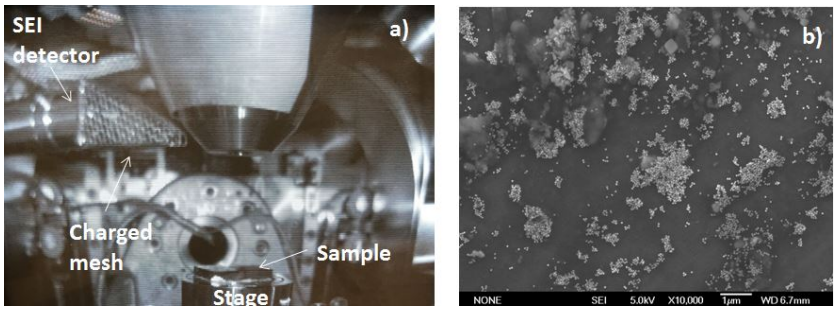

Figure 2.3: a) View from within the SEM sample chamber b) SEM image of gold nanoparticles on a glassy carbon substrate, obtained using secondary electron imaging mode

significant image distortion. As a result non-conductive samples are often coated with a gold or platinum film (thickness 1-5 nm) to eliminate these unwanted effects. Unfortunately in the case of soft organic particles their structure can be irreversibly altered due to the coating procedure, thereby limiting applicability of the technique. An additional disadvantage is the relatively high cost.

2.1.2 Transmission Electron Microscopy

Transmission electron microscopy uses a high energy electron beam focused on a thin sample and measures the electrons transmitted through the latter by a detector positioned underneath the sample. [60] The electrons which have passed through the sample collide with a fluorescent screen and their kinetic energy is converted to visible light, thereby forming an image. The image is formed by comparing the light intensities at different positions on the detector. Figure 2.2b shows the components of a TEM instrument. Holey carbon copper grids are used as common imaging substrates and the sample is drop cast and dried. TEM can routinely resolve the smallest nanopar-

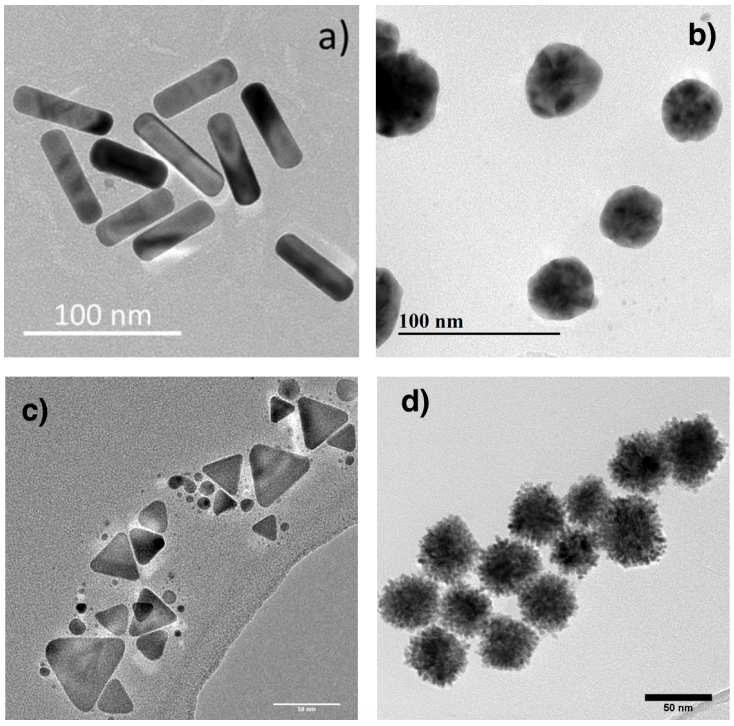

Figure 2.4: TEM images of a) gold nanorods [64], b) alloy silver-gold nanoparticles [65], c) silver nanoprisms, [66] d) platinum nanoparticles. All images except the gold nanorods were taken by the author using a Jeol 3000-F microscope.

ticles (r=0.5nm) and resolutions even below 1 nm are achievable. Figure 2.4 shows a selection of typical transmission electron microscopy images of different nanoparticles. Depending on the specification of the instrument TEM can be used as a scanning technique with very high sensitivity. This is known as "scanning transmission electron microscopy" (STEM). By measuring the emitted x-rays from the sample using a detector positioned at an angle above the sample it is possible to map elements within a single particle. This technique is known as energy dispersive X-ray spectroscopy (EDX mapping). Figure 2.5 shows an EDX map of a single alloy gold-silver nanoparticle demonstrating the even distribution of the two metallic elements. The

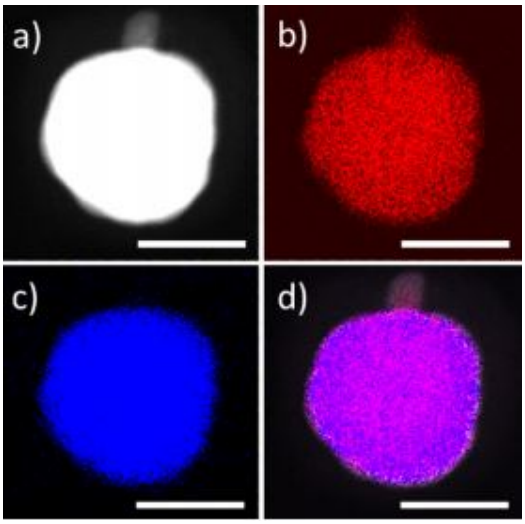

Figure 2.5: a) Dark-field TEM image of a gold–silver nanoparticle with the corresponding EDX maps for b) silver, c) gold, and d) the combined gold and silver map. Scale bars in all cases are 20 nm. [65]

main disadvantage of TEM is that upon drying nanoparticles often demonstrate agglomeration/aggregation behaviour and the imaging results may be not comparable to solution phase techniques. [67] In addition only a small fraction of the area of the sample can be imaged due to time constraints, the preparation is relatively complex and it is one of the most expensive experimental techniques. Environmental low vacuum TEM [68] and liquid-TEM [69] have been developed to allow imaging of the particles in a more natural environment and hold potential for future research. Currently such techniques are not widely available and expensive, thereby limiting access by researchers.

2.2 Light Scattering Techniques

In the present section four major methods are discussed: ultraviolet-visible spectroscopy, nanoparticle tracking analysis, dynamic light scattering and zeta potential measurements. Pros and cons of the individual techniques are discussed and applications highlighted.

2.2.1 Ultraviolet-Visible Spectroscopy

Ultraviolet-Visible spectroscopy uses photons of 190-1100 nm wavelengths to probe solution phase species. A collimated light beam is split into two parts and passed through the sample and a reference solution. The sample absorbance is measured relative to the reference solution. In the case of molecular species the absorbance A_{mol} can be described by the Beer-Lambert law [13]:

$$A_{mol} = \frac{I_0}{I} = \epsilon c^* L \tag{2.3}$$

where I_0 is the incident intensity, I is the transmitted intensity, ϵ is the molar extinction coefficient of the species, c^* is the bulk concentration, L is the beam path length. The use of a reference solution eliminates the contribution of the solvents absorbance and allows determination of the absorbance of the species of interest. The Beer-Lambert law predicts a linear relationship between the absorbance and concentration of the species. It involves the following assumptions: the species do not interact (low concentrations), the sample is non-fluorescent and does not scatter light. In the case of non-metallic nanoparticles limited absorption and/or scattering of light takes place as the size of the particles is below the wavelength of light.

However due to delocalised electrons metallic nanoparticles can interact with electromagnetic radiation and exhibit a phenomenon known as localised surface plasmon resonance (LSPR) at the metal-solution interface. [70] LSPR occurs due to a temporary separation of charge caused by oscillation of electrons in the conduction band in response to an external electric field and this strongly depends on the electronic structure of the material. The amplitude of the oscillation reaches a maximum at certain incident light wavelength and a peak in the absorption spectrum is observed. Theoretically the general electromagnetic wave-particle interaction can be understood using Maxwell's electromagnetic theory. [71] In 1908 Mie derived a rigorous general solution on the basis of Maxwell's theory. [72] This solution is now known as the Mie theory and allows us to compute the scattering caused by a homogeneous sphere of an arbitrary size in a homogeneous medium. The theory is applicable to multiple scatterers provided there are no coherent phase relations. [73] The applicability of Mie theory has been extended to other regular shapes such as spheroids and cylinders. [74] The development of fast modern computers has allowed us to determine the properties of arbitrary shaped particles via numeric approximations. [70] A metallic NP can exhibit a number of resonance modes based on its composition and geometry. For spherical nanoparticles of silver, copper and gold this dipole resonance occurs in the UV-Vis region and as a result can be detected by UV-vis spectroscopy as evidenced by a presence of a single peak in the absorption spectrum. For highly mono-disperse, sharply-distributed samples the absorption peak can be used to determine the size of the nanoparticles. [75, 76] For non-spherical nanoparticles multiple resonance modes can exist; a nano-rod can exhibit

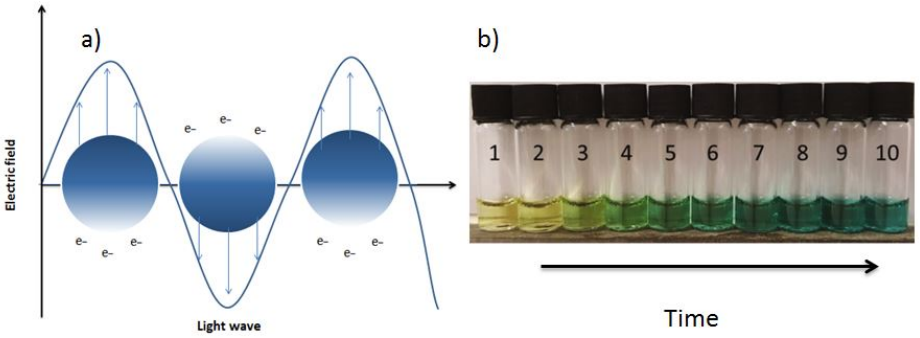

Figure 2.6: a) Schematic interaction of electromagnetic radiation with a nanoparticle b) Silver coloured nanoprisms solution at various growth stages due to changes in geometry leading to changes in surface plasmon resonance

longitudinal and transverse resonance modes, which results in appearance of two maxima in the UV-vis absorption spectra. [77] Figure 2.6a shows the schematic interaction of light with a nanoparticle, Figure 2.6b shows the solution of nanoprisms at different stages of the growth process and the resultant colours due to LSPR. Typically as the size of the particle increases the resonance will take place at longer wavelengths of light. As a result, UV-vis spectroscopy is sensitive to agglomeration and/or aggregation processes with the broadening of the maxima in the spectra and can be used to track the kinetics of such processes. [78] Consequently UV-vis is a powerful and relatively quick tool which allows us to study a suspension of nanoparticles.

2.2.2 Nanoparticle tracking analysis

Nanoparticles in solution are able to diffuse. The theoretical basis of diffusion is discussed in Section 1.5.1. The diffusion coefficient of a sphere can be predicted using the Stokes-Einstein-Sutherland equation [79, 80] at the slip

limit:

$$D = \frac{k_B T}{6\pi\eta r_{np}} \tag{2.4}$$

where k_B is the Bolzmann coefficient, η is the viscosity and r_{np} is the radius of a sphere. In order to calculate the diffusion coefficient of a nanoparticle in solution one needs to consider its hydrodynamic radius which is different to the solid NP radius as measured by electron microscopy. The hydrodynamic radius (r_{hr}) is given in accordance with:

$$r_{hr} = r_{core} + r_{cap} + r_{hs} \tag{2.5}$$

where r_{core} is the radius of the solid NP core, r_{cap} is the thickness of the capping agent and r_{hs} is the thickness of the hydration shell. Consequently the hydrodynamic radius is larger than the radius of the solid core. By measuring the diffusion coefficient of a particle its hydrodynamic radius can be estimated. Figure 2.7a shows the difference between core and hydrodynamic radii schematically. This relationship forms the basis of nanoparticle tracking analysis (NTA). [81] The technique involves a laser beam being passed through a thin volume cell containing suspended nanoparticles. NPs scatter light and appear as bright "dots", which can be imaged and recorded using an optical microscope with a charge-coupled device (CCD) camera. Figure 2.7b shows scattering of silver nanoparticles as imaged by NTA. The software algorithm then tracks the movement of individual nanoparticles in two dimensions and computes the mean-squared displacement of particles ($\overline{(x,y)^2}$). [81] The hydrodynamic radius of the particle can be determined in

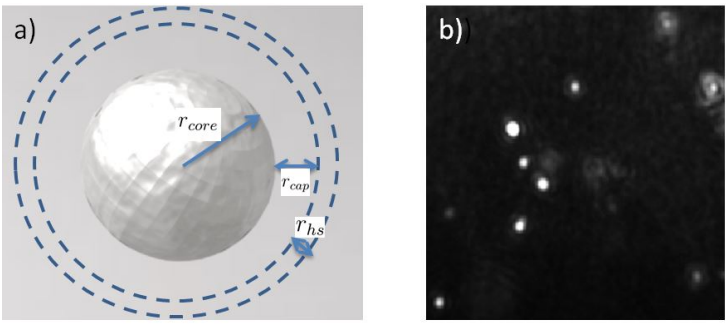

Figure 2.7: a) Schematic structure of a nanoparticle in solution, b)Scattering of light by silver nanoparticles, imaged by an optical microscope with a CCD camera.

accordance with the following relationship:

$$\overline{(x,y)^2} = \frac{2k_BT}{3r_{hr}\pi\eta} \tag{2.6}$$

NTA allows sizing of particles ranging from 10 to 2000 nm and operates in the concentration range of $10^6 - 10^9$ particles mL^{-1}. It has been applied to a diverse number of systems from metallic nanoparticles [82] to exosomes. [83] NTA is particularly useful for systems with high polydispersity and/or different scattering properties. The disadvantages include: requirement for a specific concentration range and inability to operate in optically opaque media, which is often encountered in environmentally-relevant samples.

2.2.3 Dynamic Light Scattering

Dynamic light scattering (DLS) operates by measuring the scattered light intensity caused by the solution containing nanoparticles as a function of time. [84, 85] For particles smaller than the wavelength of light, isotropic (Rayleigh) scattering is dominant. [84, 86] The scattered light intensity by a

sphere of radius r can be approximated by:

$$I = I_0 \frac{1 + cos^2\Theta}{2R^2} (\frac{2\pi}{\lambda})^4 (\frac{n^2 - 1}{n^2 + 2}) r^6 \tag{2.7}$$

where I_0 is the intensity of the incident beam, Θ is the scattering angle, R is the distance to the particle, λ is the wavelength of light, n is the refractive index, and r is the radius of a particle. In accordance with Equation 2.7 the scattered intensity is dependent on the radius of a particle:

$$I_0 \propto r^6 \tag{2.8}$$

As particles move in a laser beam due to Brownian motion, the scattered light intensity fluctuates. This fluctuation is due to either constructive or destructive interference of scattered light based on the position of the particle. The intensity $I(q,t)$ scattered to a point fluctuates fast if the particles are small and slowly if the particles are large. It is possible to extract the information about the particle size by defining a time correlation function and comparing the signal with a delayed version of the same signal:

$$G^{(2)}(q,\tau) = \langle I_S(q,0) I_S(q,\tau) \rangle \equiv \lim_{T\to\infty} \frac{1}{T} \int_0^T dt I_S(q,t) I_S(q,t+\tau) \tag{2.9}$$

In accordance with the expression, the signal is compared within the delayed version of the signal for a range of delay times τ. At zero time perfect correlation is observed, while at longer time scales the correlation decays to zero. It is possible to define the normalized time correlation function of the

scattered intensity [87]:

$$g^{(2)}(q,\tau) \equiv \frac{\langle I_S(q,0) I_S(q,r)\rangle}{\langle I_S(q)\rangle} \tag{2.10}$$

The normalized time correlation function of the scattered electric field is defined by:

$$g^{(1)}(q,r) \equiv \frac{\langle E_S(q,0) E_E(q,r)\rangle}{\langle I_S(q)\rangle} \tag{2.11}$$

The correlation function of the scattered electric field is impossible to measure directly. The Siegert relationship connects the two correlation functions [87]:

$$g^{(2)}(q,\tau) = A(1+\beta[g^{(1)}(q,\tau)]^2) \tag{2.12}$$

β is the intercept of the correlation function and will be dependent on the instrument and the size of the particles. The term A corresponds to the instrumental base line. As a result it is possible to use this relationship to convert the measured fluctuations in intensity to the field fluctuations. For mono-disperse samples the electric field decay rate follows a simple exponential decay $g^{(1)}(\tau) = e^{-\Gamma\tau}$ where Γ is decay rate. Hence expression 2.12 becomes:

$$g^{(2)}(q,\tau) = A(1+\beta[e^{-2\Gamma\tau}] \tag{2.13}$$

The decay rate is related to the diffusion coefficient of the particle by:

$$\Gamma = q^2 D \tag{2.14}$$

where q is the scattering vector, dependent on the optical geometry. For real-samples it is likely that multiple particle sizes are present. The total correlation function is then a sum of individual exponential functions for different particle sizes:

$$g^{(1)}(\tau) = \sum_{n=1}^{N} A_n e^{-\Gamma_n \tau} \tag{2.15}$$

where A_n are the intensity weighted contributions to the overall decay rate and will be dependent on the concentration of species. In order to quantify the particle size distributions, a polydispersity index (PdI) is used. For a sample which follows a Gaussian distribution the PdI relates the standard deviation of the sample with the hydrodynamic mean size:

$$PdI = \frac{\sigma^2}{Z_D^2} \tag{2.16}$$

where σ is the the standard deviation of the distribution, Z_D is the hydrodynamic mean. Practically the size distribution of the sample is determined by fitting multiple exponential decay functions using a numerical fitting algorithm, examples of common algorithms include: General Purpose fitting, CONTIN, and Multiple Narrow Mode. [84,87] Note that the above derivation assumes a lack of interaction between the particles. At higher concentrations this assumption is no longer true and as a result the determined hydrodynamic radius may contain significant errors. Equation 2.8 presents a fundamental limitation in application of the technique to mixtures containing multiple size distributions as the light scattered by the small particles will be extremely small in comparison to larger scatters due to the r^6 dependence and the resultant distribution would be skewed to larger particle sizes.

2.2.4 Zeta Potential Measurements

The stability of suspensions of nanoparticle is crucial for fundamental research and practical applications. In the present section processes which affect the stability of the particles and methods to counter the destabilization effects will be discussed.

Nanoparticles have high surface to volume ratios and as a result are thermodynamically favourable to clustering, which thereby reduces this ratio. Particles are also attracted by weak van der Waals forces due to temporary dipole formation. Particle clustering processes can be divided into two broad categories based on the nature of the process in accordance with the IUPAC definition: reversible agglomeration and irreversible aggregation. [7] Agglomerated particles can be re-dispersed via mechanical means or changes in the ionic strength, while during aggregation particles sinter together and cannot be re-suspended. [82] Two general stabilization routes are: steric [88, 89] and electrostatic stabilization. [90] The steric method involves the use of a bulky polymer, typically polyethylene glycol (PEG) to cap the particles. As a result particle cores are physically separated and agglomeration and/or aggregation is minimized. This method often leads to a significant increase in the hydrodynamic radius of the particle and affects the resultant mass transport of the particles. The electrostatic stabilization is achieved by functionalizing a particle with charged surface groups. Examples of common stabilization agents are citric acid used to cap silver NPs and cetyltrimethylammonium bromide (CTAB) for gold NPs. Like-charged particles repel and the resultant suspension is stable provided that the ionic strength is low. In a solution an

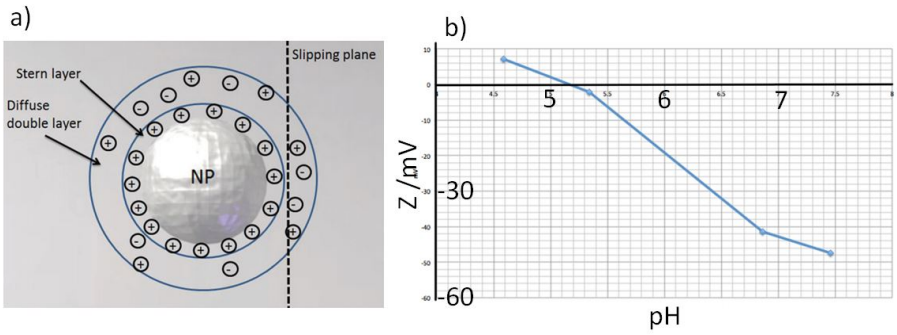

Figure 2.8: a) Schematic structure of the double layer surrounding a charged particle b) Zeta potential as a function of pH for APTES-modified silica nanoparticles as measured by the author

ionic double layer surrounding a charged nanoparticle is formed. Close to the particles surface the ions are tightly bound and move with the particle. This layer is known as the Stern layer. Further away from the particle, a dynamic diffuse layer is formed. Ions in the diffuse layer experience electrostatic forces caused by the presence of a charged particle but are free to move. The potential at the boundary of strongly-bound and freely-moving ions (slipping plane) is known as the zeta potential. [91, 92] The structure of the double layer surrounding a particle is shown schematically in Figure 2.8a

It is possible to determine the zeta potential through electrophoretic mobility measurements. The zeta potential can be expressed as:

$$Z = \mu_e \frac{3\eta}{2\varepsilon\varepsilon_0 f_H} \tag{2.17}$$

where μ_e is the electrophoretic mobility (v), ε is the dielectric constant, ε_0 is the permittivity of free space ($C^2\ N^{-1}\ m^{-2}$), Z is the zeta potential, η is the dynamic viscosity and f_H is the Henry's function. The value of the Henry's function is dependent on the media and ionic strength. For non-polar media

$f_H = 1$ and for polar media the value is $f_H = 1.5$. Zeta potentials provide a measure of the stability and particles with $z \geq 30\ mV$ are considered stable. [91] The surface charge of a particle (q_s) can be determined using the Stokes equation in conjunction with the electrophoretic mobility:

$$q_s = 6\pi r_{np} \eta \mu_e \tag{2.18}$$

Experimentally, electrophoretic mobility can be measured using a DLS instrument with an optical two-electrode cell. By applying a potential of $|80 - 150|\ V$ migration of the particles is induced and subsequently electrophoretic mobility determined. For many capping agents zeta potentials would be pH-dependent due to protonation/deprotonation of the chemical groups. Figure 2.8b shows the zeta potential as a function of pH for APTES-modified silica nanoparticles.

2.3 Particle characterization using electrochemical methods

In the present section, ensemble characterization such as stripping and dissolution voltammetry and single particle-electrode impact electrochemical methods will be discussed.

2.3.1 Stripping Voltammetry

Stripping voltammetry has been traditionally used to study adsorbed organic monolayers. For a Nernstian adsorbate layer at a planar macroelectrode the

peak current is predicted by [2]:

$$i_p = \frac{(nF)^2}{4RT} v A \Gamma c^* \tag{2.19}$$

where Γ is the surface coverage of the adsorbate. The peak current is directly proportional to the scan rate, due to the fact that the species are at the electrode surface and no diffusion takes place. Therefore the surface-confined process can be distinguished from a diffusional one by conducting a scan rate study. For electroactive particles, stripping voltammetry is a powerful technique allowing us to determine the identity of the particles based on their redox potentials. [93] The simple modification procedure involves drop-casting the dispersed nanoparticles on an electrode and allowing the solvent to evaporate. The functionalised electrode is then immersed in an electrolyte containing solution and linear-scan or cyclic voltammetry is performed. The resultant peaks in the voltammogram can be integrated to determine the overall charge transferred in accordance with:

$$Q = \frac{\int_{E_1}^{E_2} I dV}{v} \tag{2.20}$$

where E_1 and E_2 are the start and end potentials and v is the scan rate. As a result one can determine the total amount of material oxidised or reduced. If the size of the particle is known from alternative characterization methods, the number of particles deposited on the electrode can be deduced, assuming full oxidation or reduction takes place. The observed current response is more complex in comparison to molecular species and will be de-

pendent on the size of the particles [94], aggregation and/or agglomeration state [95], inter-particle distance [96] and the surface coverage [97,98]. To ensure quantitatively complete oxidation/reduction of particles sub-monolayer surface coverages should be used. Higher coverages may lead to incomplete stripping, and as a result, smaller current magnitudes in comparison to the theoretically predicted value. [95] For an irreversible system the peak potential is independent of the size of the adsorbed nanoparticle for sub monolayer coverages. [99] The potential shift dependence on the size of the particle in comparison to bulk metal can be predicted using the Plieth equation [100]:

$$\Delta_{E_D} = -\frac{2\gamma v_M}{zF}\frac{1}{r} \tag{2.21}$$

where Δ_{E_D} is the difference in equilibrium oxidation potential, γ is the surface tension,v_M is the molar volume, z is the number of electrons transferred, r_{np} is the radius of a particle. The observed response, if electrochemically reversible, is dependent on the concentration of the solution phase ions in accordance with the Nernst equation and the surface coverage of the particles.

2.3.2 Dissolution voltammetry

For analytical purposes in order to avoid complications due to surface coverages, agglomeration and/or aggregation processes, particles can be dissolved and traditional cyclic voltammetry performed on the resultant ionic species. [101, 102] By dissolving the particle one can determine their composition and respective concentrations but all sizing information is lost.

2.3.3 Particle-electrode impacts

It has been demonstrated previously that ensemble methods involve multiple experimental variables such as: particle surface coverages, inter-particle distances and agglomeration/aggregation phenomena. As a result properties of an ensemble may significantly differ from that of an individual particle. Consequently the ability to study electrochemical properties of single NPs has dramatically altered the field of electrochemistry.

Precursors to modern electrode-particle impacts are the early stirred microparticle suspension experiments by Micka [103] performed in 1956. The experiments involved insoluble CuS, PbS, HgS and Ag_2O compounds suspended in aqueous solvent. A cathodic peak in the damped polarographic wave was observed in a stirred solution, which corresponded to the multiple collisions of particles. The technique was subsequently modified and used industrially by E.I du Pont de Nemours & Company (Wilmington, Delaware, USA) to size grains of AgBr particles through a use of rotating turntable with the deposited particles and a needle electrode passing over the surface, thereby reducing the deposited particles. [104–106] Heyrovsky has used the electrode-particle impact method to study the catalytic reduction of H^+ at SnO_2, TiO_2 and Fe_2O_3 particles colliding with an electrode. [107–110] Earlier works have focused on the current response due to multiple simultaneous collisions; by contrast modern developments are aimed at studying individual collisions. Bard *et al.* first reported the collision of single platinum nanoparticles on carbon and benzenedimethanethiol-modified gold microelectrodes in proton containing-media. Upon a collision the proton reduction reaction is

catalyzed by an impacting particle, leading to an observation of 'spikes' and 'steps'. [111] The magnitude of a step is related to the radius of the particle, and assuming steady-state limiting current at a sphere on an infinite plane can be expressed as:

$$i_{np} = 4\pi(ln\ 2)nFDc^*r_{np} \tag{2.22}$$

where c^* is the concentration of the redox active species and r_{np} is the radius of a particle. This type of collision is referred to as mediated Faradaic impact. The process is shown schematically in Figure 2.9b. Generally electrode-particle impacts can be separated into four broad categories based on the nature of physical interaction taking place: direct Faradaic, mediated Faradaic, capacitative and blocking impacts. [112]

Direct Faradaic Impacts

Direct Faradaic impacts involve electron transfer between the electrode and the particle leading to subsequent oxidation/reduction of the particle and in some cases dissolution. Compton *et al.* demonstrated the use of direct-Faradaic impacts for quantitative sizing of individual silver nanoparticles. [113] The following electrochemical reaction takes place upon an impact:

$$Ag_{N(np)} - Ne^- \rightleftharpoons NAg^+_{(aq)} \tag{2.23}$$

In accordance with Faraday's law the charge transferred in a collision event is given by:

$$Q = \int_{t_1}^{t_2} Idt \tag{2.24}$$

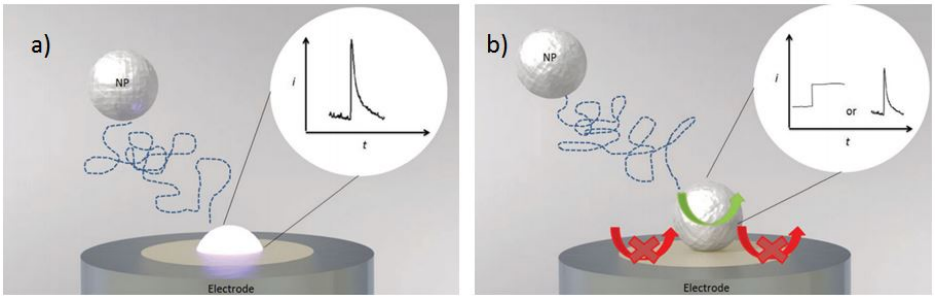

Figure 2.9: a) Direct Faradaic impact, leading to subsequent dissolution of the particle b) Mediated Faradaic impact, an impacting particle catalyzes the reaction at its surface

where t_1 and t_2 correspond to the spike duration. Under assumption of spherical geometry, provided that the density and number of electrons transferred is known, the size of the impacting particle can be deduced:

$$r_{np} = \sqrt[3]{\frac{3A_rQ}{4\pi nF\rho}} \tag{2.25}$$

where A_r is the atomic mass, and ρ is the bulk metal density. Excellent agreement was observed between the impact size distributions and the size distribution obtained via SEM imaging. The direct Faradaic approach has been extended to a wide range of systems such as: copper [114], nickel [115], gold [116], iron oxide [117] and indigo nanoparticles [118] in aqueous media. The method can also be used in non-aqueous media for example: in ionic liquids [119] and in an acetonitrile/n-methyl-2-pyrrolidone mixture [120]. The process taking place at a surface of microelectrode is shown schematically in Figure 2.9a.

Capacitative Impacts

Capacitative impacts can be separated into two further subclasses: either due to the displacement of charge from the electrode–electrolyte interface (double layer) or from the charging of an impacting nanoparticle. [112] In neither processes are electrons transferred to or from the solution at the electrode. The charge neutrality is maintained by the electrons either leaving or entering the bulk of the electrode in response to changes at the electrode/electrolyte interface. The capacitative impacts show distinct potential dependences and are affected by the surface area of the colliding particle. [121] As the potential approaches the potential of zero charge (PZC) of the particles the spike magnitude decreases and eventually no spikes are observed at PZC. [121]

Blocking Impacts

Blocking impacts were first reported by Lemay *et al.* [122], who used solution phase ferrocene methanol as a redox active marker and carboxylated micro- and nano-spheres. Upon an arrival of a microsphere, the electroactive area of the electrode decreased, leading to a corresponding decrease in the current and resulting in an apparent 'step'. [122] The step height can be used to determine the size of an adsorbed particle. The method has been used to detect and identify discrete adsorption events of antibodies, enzymes, and DNA molecules. [123] For further in-depth discussion of types of impacts and systems studied to date, the reader is referred to reviews by Rees *et al.* [124], Cheng *et al.* [125] and Compton *et al.* [112]

2.3.4 Present work

This thesis evaluates the assumptions used to study particles by the *direct* electrode-particle impact method. In particular the assumption of spherical geometry is relaxed and the method is extended to quasi-spherical particles, thereby allowing accurate quantitative sizing. The importance of agglomeration/aggregation processes is explored via a combination of electrochemical methods and light scattering. Numerical simulation is performed to quantify the rate constants in the agglomeration/de-agglomeration processes. The thermodynamic causes of agglomeration are explored using the entropy of mixing concept and used to predict entropy-only size distributions of the particles. In addition this thesis theoretically evaluates the use of forced convection to enhance mass transport to the electrode and highlights the importance of anisotropic diffusion of nanoparticles within a close proximity of the solid boundary. Finally the use of electrode-impact techniques in a wall-jet flow cell is demonstrated and the lowest limit of nanoparticle detection is reported. The next chapter covers the experimental methods and techniques used throughout the thesis.

Chapter 3

Experimental and Computational Methods

In the present chapter the chemical reagents and nanoparticles used in the present work are described. Details of equipment used are also provided.

3.1 Experimental

3.1.1 Chemicals

For convenience the chemicals used throughout the thesis are summarized in Table 3.1. Table 3.2 shows the NPs purchased from commercial suppliers. Table 3.3 provides the details of manufacturers and chemical suppliers.

Table 3.1: Chemical reagents used in the thesis

Formula	Chemical Name	Purity	Supplier	Section
KCl	Potassium Chloride	99.5%	Sigma Aldrich	4,5,7
NaOH	Sodium Hydroxide	97.0%	Sigma Aldrich	5
$[Ru(NH_3)_6]Cl_3$	Ruthenium Hexamine	98.0%	Sigma Aldrich	4,5
$K_4Fe(CN)_6$	Potassium Ferrocyanide	99.0%	BDH	8

Table 3.2: List of nanoparticles used in present work

Material	Diameter (nm)	Supplier	Section
Citrate-capped silver (aqueous suspension)	100	nano ComposiX	4,5,7
Citrate-capped silver (aqueous suspension)	25	nano ComposiX	8
Bismuth oxide (powder)	38	Nanophase	5,7

Table 3.3: List of instrument manufacturers and chemical suppliers

Company Name	Address
Alfa Aesar	Lancashire, UK
BDH	Poole, UK
Buehler	Coventry, UK
BASi	West Lafayette, USA
Fischer	Loughborough, UK
Goodfellow Ltd	Cambride, UK
nanoComposiX	San Diego, USA
Nanophase	Romeoville, USA
VWR	Soulbury, UK
Sigma Aldrich	Dorset, UK

Table 3.4: List of electrodes used in the present thesis. Abbreviations: working electrode (WE), reference electrode (RE), counter electrode (CE)

Electrode	Radius	Supplier	Section
Carbon fibre microdisk (WE)	3.5 μm	BASi	5
Glassy carbon macrodisk (WE)	1.5 mm	BASi	4,5,8
Random assembly of microelectrodes (WE)	6 mm (3.5μm per fibre)	Loughborough University	4,5,8
Graphite Rod (CE)	N/A	Sigma Aldrich	8
Platinum wire (CE)	N/A	Goodfellow Ltd.	4,5
Saturated calomel electrode (RE)	N/A	BASi	4,5,8
Mercury-mercurous sulfate electrode (RE)	N/A	BASi	5

3.1.2 Electrochemical Instrumentation

All electrochemical measurements were carried out in a thermostatted Faraday cage held at $25.0 \pm 0.1°C$. Aqueous solutions were prepared using Millipore water of resistivity 18.2 $M\Omega\ cm$ at 298 K and were purged with nitrogen prior to the experiments, unless stated otherwise. The working electrodes were polished using descending grades of alumina powder ($1\mu m$, $0.3\mu m$ and $0.05\mu m$) supplied by Buehler. Table 3.4 summarises the electrodes used in the present work. Autolab Type III potentiostat manufactured by Metrohm Autolab B.V. (Utrecht, Netherlands) was used with a three electrode cell for cyclic-voltammetry measurements. Nova 1.4 was used as a control software. For low noise impact measurements, an in-house manufactured potentiostat was used. [126] This potentiostat involves three main sections; the computer interface used for analog-to-digital and digital-to-analog conversion, the current amplifier circuit and the stabilised potentiostat. A Labjack U6 (Labjack corporation, Lakewood, CO. USA), with a Labjack tickDAC, was used for the computer interface. Connection to the Labjack was made via a standard USB but with the ground isolated from that of the PC (USB-ISO OLIMEX, Farnell, Leeds, UK). Control of the Labjack was performed using a script written in Python 2.7 and run through the IDE Canopy (Enthought, Austin,

TX USA). Measurement of the current at the working electrode (running to ground) was achieved with a low current-amplifier LCA-4K-1G (FEMTO, Messtechnik GmbH, Germany) and the bandwidth of the output of the current amplifier was limited using a 100 Hz 2-pole passive RC filter, Linear Technology DC338A-B (Farnell, Leeds, UK). The resulting analog signal was digitised using the Labjack at a stream rate of 4 kHz. Potentiostatic control was provided by a highly stabilised (1 kHz bandwidth) classic adder potentiostat. Importantly, first, for the reference buffer a high quality operational-amplifier LMC6001 (Farnell, Leeds, UK) with ultra low-input bias (25 fA) was used. Second, a high quality low-noise operational-amplifier, AD797 (Farnell, Leeds, UK), provided the control of the potential at the counter electrode. [126] For particle-electrode spike analysis in-house developed software Signal Counter developed by Dr Dario Omanović (Rudger Bošković Institute, Zagreb, Croatia) was used. Spike distributions were obtained using Origin 2015 (OriginLab Corp, Northampton, Massachusetts, USA)

3.1.3 Electron Imaging Instrumentation

Transmission electron microscopy

TEM imaging was performed in collaboration with Dr. N. P. Young (Materials Department, University of Oxford). For transmission electron microscopy, a JEOL JEM 3000-F instrument (Tokyo, Japan) equipped with field emission gun was used with typical acceleration voltages of 100-300 keV. The samples were dropcast on holey carbon grid and dried under nitrogen flow. A single tilt (±25 degrees) specimen holder was used. ImageJ

software was used for particle sizing (W.S.Rasband, ImageJ, US National Institutes of Health,Bethesda, Maryland, USA, http://imagej. nih.gov/ij/ 1997–2014). Size distributions were performed using Origin 2015 software (OriginLab Corp, Northampton, Massachusetts, USA).

Scanning electron microscopy

SEM imaging was performed in collaboration with Mrs. J. Holter and Dr. N. P. Young (Materials Department, University of Oxford). For particles larger than 1 μm in radius, a Zeiss EVO MA10 microscope (Zeiss, Jena, Germany) equipped with a tungsten source was used. Secondary electron imaging mode was used. Non-conductive samples were coated with a 3 nm layer of platinum to avoid surface charging and imaging artefacts. For particles smaller than 1 μm, a JEOL JSM-6500F microscope (Tokyo, Japan) was used equipped with a low voltage field emission gun operated between 1 and 30 kV. Secondary electron imaging mode was used. For size analysis ImageJ was used (W.S.Rasband, ImageJ, US National Institutes of Health, Bethesda, Maryland, USA, http://imagej. nih.gov/ij/ 1997–2014).

3.1.4 Light Scattering Instrumentation

Ultra-violet visible spectrometer

UV-Vis studies were performed using a UV-1800 instrument manufactured by Shimadzu (Kyoto,Japan). A quartz cell with 2-mm path length was used. The sampling was set to 1 nm frequency and bulb transition was chosen at 300 nm to avoid interference with plasmonic peaks.

Dynamic Light Scattering and Zeta Potential Measurements

DLS was performed with assistance from Dr. K. Jurkschat (Materials Department, University of Oxford). A Malvern Zetosizer Nano ZS (Malvern Instruments, Malvern, UK) equipped with 638 nm laser was used for dynamic light scattering. Samples were transferred to disposable plastic cuvettes. The temperature was maintained at $25.0 \pm 0.1\ C^{\circ}$. A general purpose fitting algorithm was used to obtain the particle size distributions. Data analysis was performed using Zetasizer Software. Zeta Potential measurements were performed using a folded capillary optical cell with two gold electrodes. Data analysis was performed using Zetasizer Software

Nanoparticle Tracking Analysis

NTA measurements were performed using a Nanosight LM10 instrument (Malvern Instruments, Malvern, UK) with assistance from Dr.K. Jurkschat (Materials Department, University of Oxford). The video was recorded for 60 seconds with a frame-rate of 30 $frames\, s^{-1}$. Tracking of the particles was done using NTA 2.3 software and the resultant size distributions used without further analysis. The temperature was maintained during the measurement at $25.0 \pm 0.1\, C^{\circ}$.

3.2 Computational Methods

Computations were performed using Mathematica 10.2 software (Wolfram Research, Inc., Champaign, IL, USA). Custom C++ code was written and compiled using Microsoft Visual Studio 2015 (Microsoft, Redmond, USA).

The software was run on a personal computer equipped with Intel Processor Core i5-3570 CPU @ 3.40 GHz and 4GB of RAM. Data visualisation was done in Origin 2015 software (Origin Lab Corporation)

Chapter 4

Sizing of quasi-spherical particles

Prior electrode-particle impacts reported in literature have exclusively focused on spherical nanoparticles. In this chapter the application of electrode-particle impact techniques is developed to account for non-sphericity and used to quantitatively size quasi-spherical citrate-capped silver nanoparticles. The results were corroborated with scanning electron microscopy imaging and accurate size distributions of the particles obtained. This work has been published in *Chemistry: A European Journal*. [127]

4.1 Introduction

Non-spherical nanoparticle geometries hold potential advantages due to unusual properties such as enhanced catalytic activity [128], additional surface plasmon resonance modes [77, 129], and stronger magnetic properties. [58]

Quasi-spherical particles are particularly important for catalytic applications. One example is the oxygen reduction reaction (ORR), [130] which is strongly influenced by the presence of Au (100) surface domains on Au nanoparticles; thus, the greatest catalytic activity is observed for particles that deviate from spherical geometry. Sizing such particles using electron microscopy is challenging as discussed in Section 3.1.3. The main advantage of electron microscopy sizing is that readily understandable visual shape information is obtained. However,the number of particles probed is generally small (1000 particles) and careful sample preparation is required for these techniques conducted in vacuum. In particular, particle aggregation during drying of the sample has to be avoided as far as possible. Light scattering methods provide the hydrodynamic radius information and involve spherical assumptions as stated in Section 2.2; as a result for quasi-spherical particles such techniques lack the sensitivity to detect subtle geometry changes. By contrast, electrode-particle impacts, provide atomic counting information and corresponding volume information for individual particles. Given that a statistically significant number of particles are analysed, it is also possible to obtain the distribution of sizes. In contrast to electron microscopy imaging, electrode-particle impacts can be conveniently performed in the solution phase, reducing the influence of aggregation effects and providing valuable in situ information.

4.2 Geometrical considerations

A metallic nanoparticle is a solid of certain dimensions and density (often assumed to be equal to the bulk value). A perfectly spherical particle can be fully described by its radius; if the radius is known, additional information such as volume and surface area can be immediately obtained, through elementary geometrical analysis. For electrode-particle impacts the spherical assumption is typically valid and greatly simplifies the data analysis as the particles can be described by their radii. Consequently the size distributions of particles are commonly reported in terms of the spherical radius or diameter. However the nanoparticles can deviate from a perfectly spherical geometry and can often be better described by polyhedra. A polyhedron is defined as a three dimensional solid, which possesses flat polygonal faces, straight edges and sharp vertices. [131] A sphere circumscribing a polyhedron can be used to approximate its properties. Geometrically this can be represented by a sphere touching each of the vertices of the polyhedron. By such an approximation a geometrically more complex nanoparticle can be described by the radius of that sphere. A solid is effectively circumscribed by a sphere. Figure 4.1 shows a circumscribing sphere and an arbitrary polyhedron. The circumscribing sphere always has a larger volume in comparison to the inscribed polyhedron. The ratio ($R_{circumscribed}$) between the volume of the solid and circumscribed sphere is given by:

$$R_{circumscribed} = \frac{V_{polyhedron}}{V_{sphere}} \tag{4.1}$$

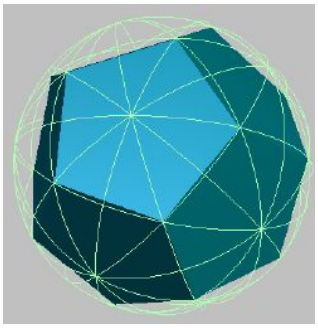

Figure 4.1: An arbitrary polyhedron and the corresponding circumscribing sphere

Electrode-particle impacts technique allows us to determine the number of atoms in an impacting particle by measuring charge transferred in a given collision event. If the density approximation is correct, the volume of a particle can be determined by considering the bulk density and atomic mass. The chosen 3-D geometry used to extract length-scale from volume may be the source of error when converting volumetric information to radius.

Typically particle sizes are reported in terms of a radius of a sphere. Hence, when the spherical approximation is used to convert volumetric information from electrode-particle impacts to determine the radii distribution of the particles, it may lead to an underestimation of the radius of a given particle in comparison to electron microscopy imaging. The isoperimetric quotient (IQ) is used to quantify the degree of sphericity of a three-dimensional solid:

$$IQ = 26\pi \frac{V^2}{S^3} \tag{4.2}$$

where V is the volume and S is the surface area. In the present work a special set of polyhedra solids are considered, namely the Platonic solids. These polyhedra have identical regular polygon faces, with all vertex angles being

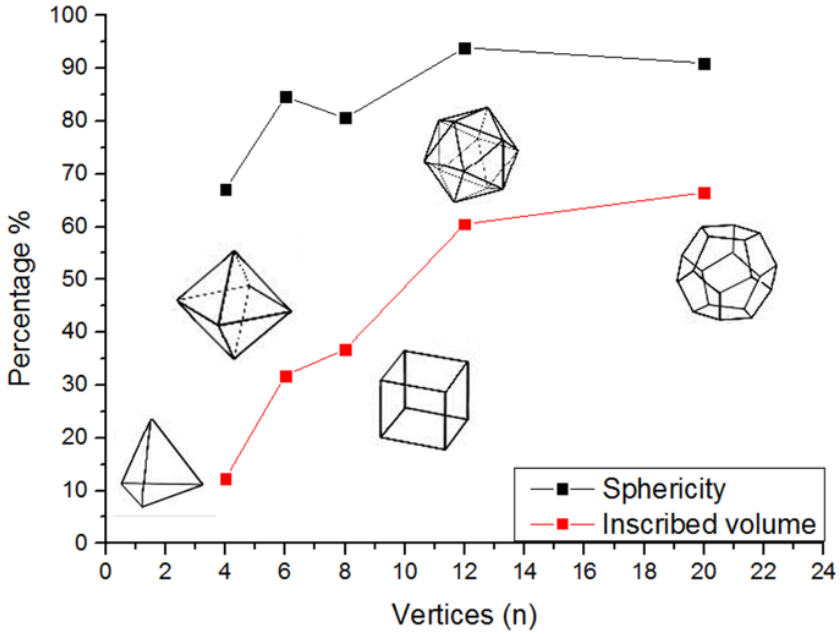

Figure 4.2: Percentage circumscribed volume and sphericity degree as a function of the number of vertices for five platonic solids

equal. As a result they possess a high degree of symmetry and are amenable to theoretical modelling. [131, 132] The circumscribed volumes and isoperimetric quotients as a function of number of the vertices for Platonic solids are shown in Figure 4.2 and this plot highlights the discrepancy between sphericity and the circumscribed volume. The general trend is that with increasing number of vertices an increase in inscribed volume is observed as a particle becomes more spherical. However, the increase in sphericity does not always correlate with the circumscribed volume as is the case for the icosahedron and dodecahedron. Consequently for quasi-spherical nanoparticles the spherical approximation is insufficient for accurate characterization and size determination.

4.3 Experimental

4.3.1 Electrochemical Measurements

Electrochemical measurements were performed using an Autolab Type II potentiostat. A random assembly of microelectrodes (RAM supplied by Prof. Dr. Stephen Fletcher, Department of Chemistry, Loughborough University) was used as a working electrode. Prior to electrode-particle impacts the RAM was characterised using ruthenium (III) hexamine chloride as a redox marker. In accordance with Section 1.7.2, a Case 2 array steady-state response was observed. Figure 4.3 shows the observed current response. The limiting current (i_{ss}) obtained can be related to the number of fibres using:

$$N_{fibre} = \frac{i_{ss}}{4r_e nFDc^*} \tag{4.3}$$

Using this equation the RAM was found to have 920 active fibres based on radius of an individual fibre assumed to be 3.5 μm as stated by the manufacturer. The oxidative potential of silver nanoparticles was determined by stripping voltammetry. A stock suspension of the commercial nanoparticles was drop cast on the electrode surface and dried under nitrogen. The resultant stripping voltammogram is shown in Figure 4.4. A clear silver stripping peak is observed at +0.145 V vs SCE. Subsequent electrode-impact experiments were conducted at a high potential of +0.6 V vs SCE to ensure complete oxidation of the impacting particles.

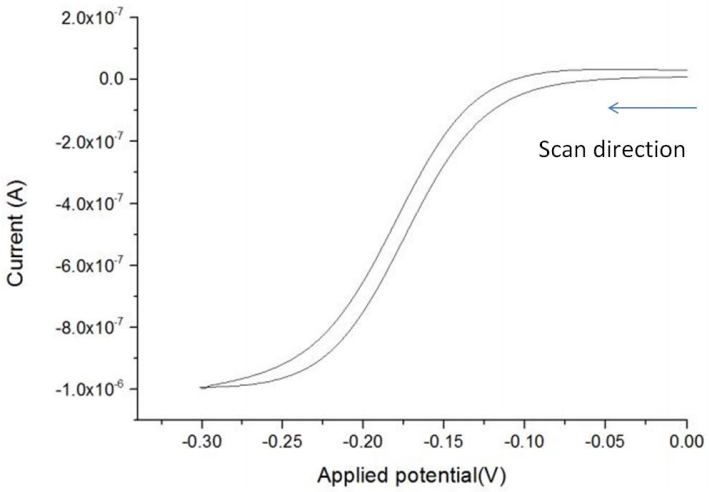

Figure 4.3: Cyclic voltammetry obtained for $Ru(NH_3)_6Cl_3$ on the RAM electrode in 0.1 M KCl, start potential=0.00 V vs SCE, scan rate of 100 mV s^{-1}

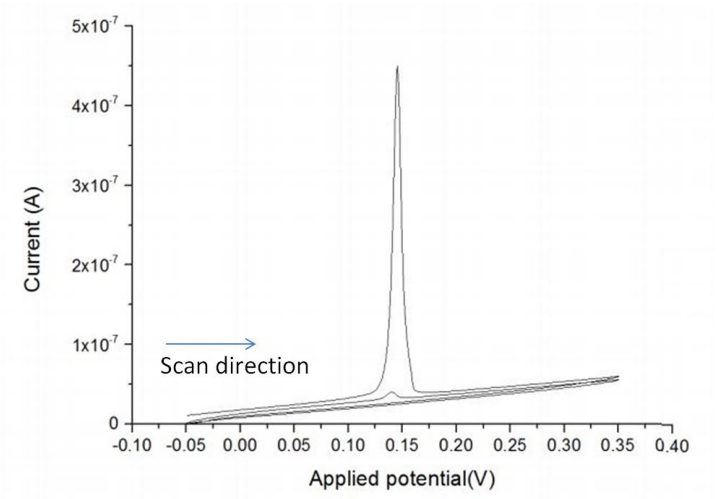

Figure 4.4: Cyclic voltammetry obtained for Ag NPs on the RAM electrode, 0.1 M KCl, start potential -0.05 V vs SCE, scan rate of 100 mV s^{-1}

4.3.2 Nanoparticle Characterisation

The commercial citrate-capped silver nanoparticles were characterised using scanning electron microscopy imaging. The stock solution was drop cast on a glassy carbon substrate and dried under nitrogen. The imaging was performed using Secondary Electron Imaging mode (see Section 3.1.3). It can be seen in the inset of Figure 4.5 that the particles have polyhedral geometry and appear hexagonal when imaged two dimensionally. Sizing of the particles was done using Image J software. The average spherical radii were determined in accordance with:

$$r_{average} = \sqrt{\frac{A}{\pi}} \tag{4.4}$$

where A is the area of the particle from the SEM image. Figure 4.5 shows the resultant size distribution and the characteristic images of the particles.The size distribution has the following characteristics: a mean radius of 50 nm and a standard deviation of 4 nm, hence the particles are mostly monodisperse.

4.4 Results and discussion

Having characterised the particles and established the oxidation potential, electrode-particle impact experiments were conducted. Figure 4.6 shows chronoamperograms in the absence and presence of the nanoparticles showing characteristic spikes. The difference in background current could be potentially attributed due to oxidation of the carbon fibers due to high applied potential of +0.60 V vs. SCE reference electrode. The charge per impact

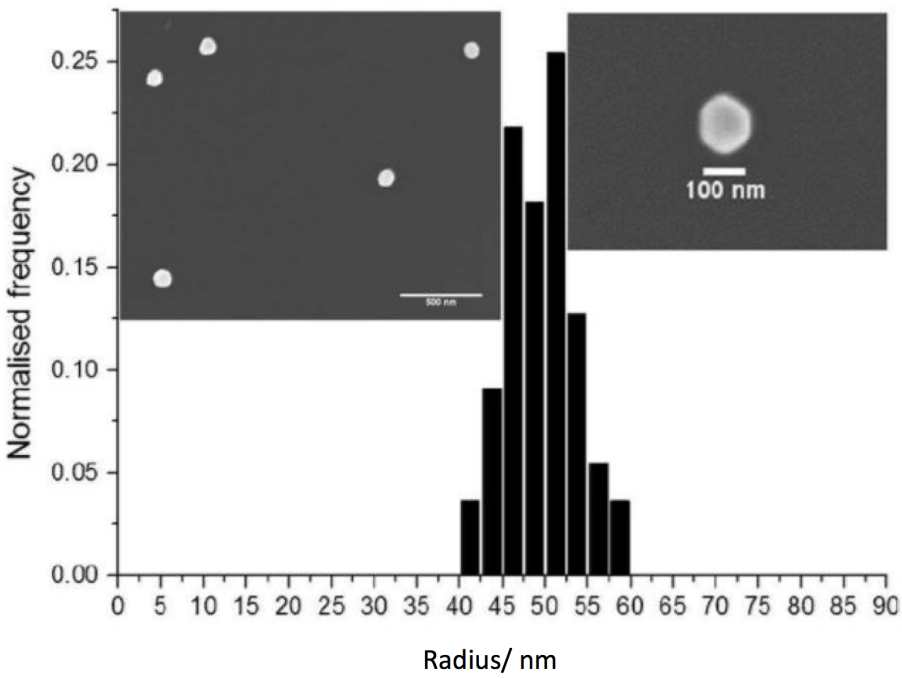

Figure 4.5: Size distribution of silver NPs as determined by SEM sizing (55 NPs counted).

was converted to radius to estimate the size of a particle under spherical approximation as discussed in Section 2.3.3. Inherent differences in diffusion coefficients need to be taken into account during size-distribution analysis as the smaller particles have a higher probability of collision with the electrode and as a result the distribution is skewed towards smaller radius nanoparticles. [133] Diffusion-corrected weighting compensates for the smaller number of larger particles being observed. The weighting is done by calculating the midpoint diffusion coefficient for each of the bars in the histogram and dividing the resulting diffusion coefficient by the diffusion coefficient of the smallest nanoparticles. As a result the individual bin count can be adjusted by the corresponding correction factor corresponding to the diffusion coefficient.The resultant distributions are shown in Figure 4.7 and compared to the SEM size distribution. The mean calculated nominal radius from impact experiments without the diffusional weighting is 40 nm, with a standard deviation of 10 nm. The use of diffusional correction shifts the mean to 41 nm with the standard deviation remaining constant. It is evident that the electrode-particle impacts show consistently smaller nanoparticle sizes in comparison to SEM (mean radius of 41 nm via nanoimpacts vs 50 nm via SEM) and the diffusional weighting does not account for the discrepancy. The wider standard deviation observed for the impact experiments can be rationalised by the fact that the electrode-particle impact technique probes a larger number of particles (several hundreds) vs 55 particles analysed via SEM. An explanation based on quasi-spherical geometry is proposed to explain the observed discrepancy. Using SEM images one can propose a geometry more consistent with the true geometry of the particles. A three-dimensional solid is required,

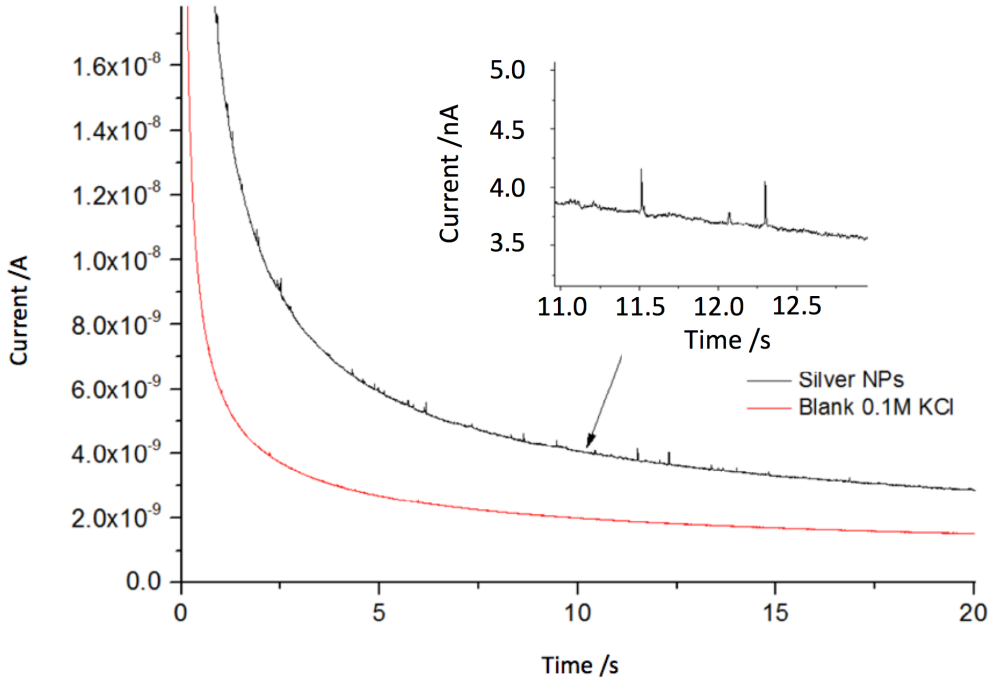

Figure 4.6: Chronoamperogram (black) obtained with nanoparticles present in the solution with RAM electrode and chronoamperogram (red) of a blank 0.1 M KCl solution without characteristic spikes.

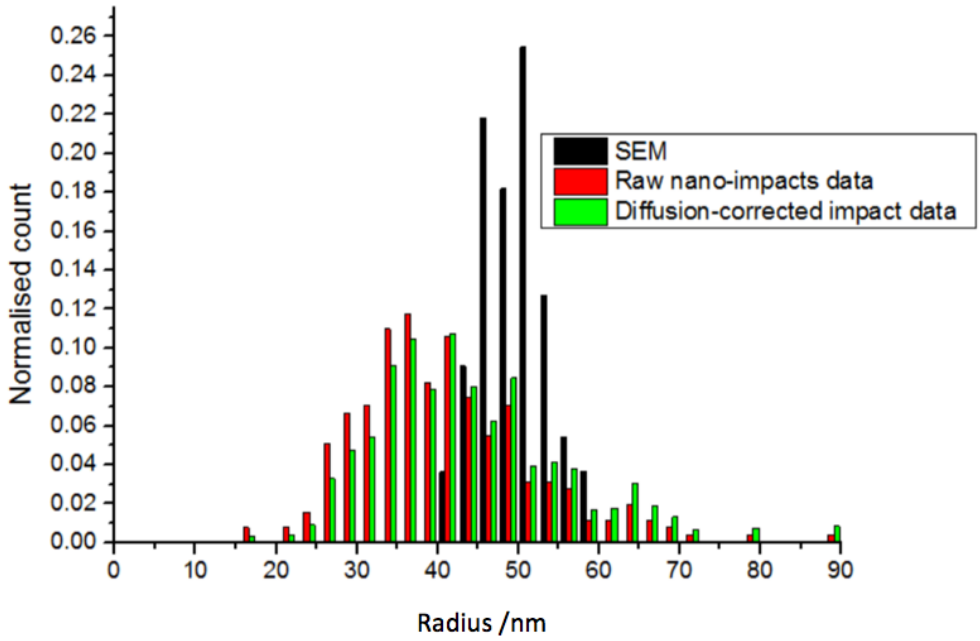

Figure 4.7: Comparison between size distributions obtained from SEM imaging (black bars) and nanoimpacts sizing without the diffusional weighting (red bars) with the diffusional weighting (green bars).

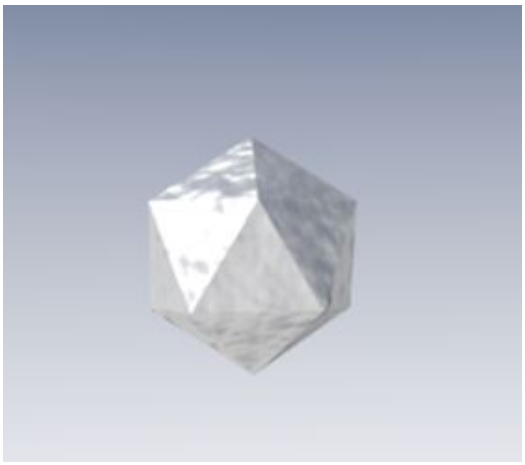

Figure 4.8: Geometry of an ideal icosahedron

which when viewed in two dimensions corresponds to an observed hexagonal shape. An icosahedron fits such requirements and is shown schematically in Figure 4.8. It has twelve vertices with twenty equilateral faces and it belongs to a set of platonic solids. [131] An icosahedron is likely to lie on its face provided that the SEM grid surface is locally smooth. As a result, when viewed from above, such lying icosahedron would appear as a hexagon. The volume of an icosahedron (V_{icos}) is given by:

$$V_{icos} = \frac{5(3+\sqrt{5})}{12}(\frac{d}{\sqrt{\Phi^2+1}})^3 \tag{4.5}$$

where the d is the length of diagonal of the hexagon, $\Phi \approx 1.61803399$ is the golden ratio. The diagonal of an icosahedron is equal to the diameter of the enclosing sphere. Hence in accordance with Equation 4.1 and Equation 4.5, for an icosahedron,the circumscribed volume is 60.5 % of a unit sphere. Hence, for an icosahedron circumscribed by a sphere of a radius of 50 nm, the corresponding charge would be almost 40% less than the charge

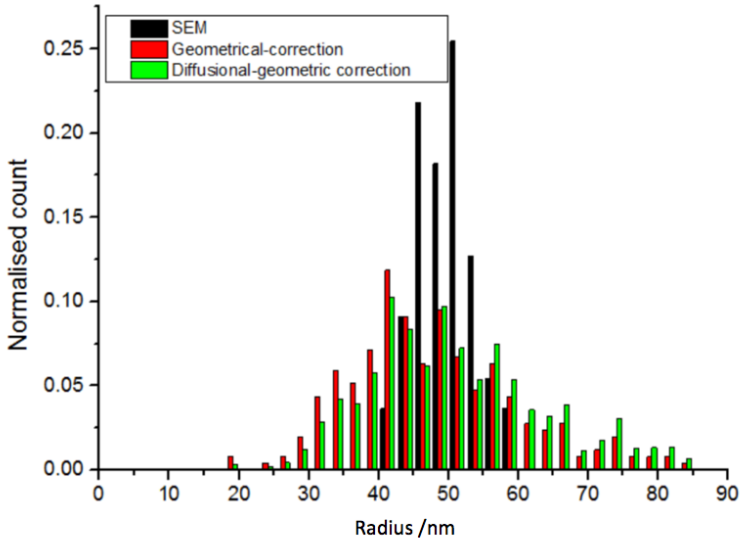

Figure 4.9: Normalised size distributions according to SEM imaging (black bars) and nanoimpacts with the applied geometric correction (red bars) and diffusionally weighted geometric correction (green bars)

for that sphere. As a result, when converting charge distribution obtained from nanoimpacts to a radius distribution of the circumscribed sphere, we need to include a correction of 40%, leading to a significant increase in the determined radius. An icosahedron has the highest degree of sphericity of 93.9% of all platonic solids in accordance with Equation 4.2. As a result, it appears almost spherical from two dimensional images,which can lead to significant sizing errors, if electron microscopy imaging is used as the only sizing technique. Hence, icosahedron-shaped particles can account for the missing charge relative to the spherical approximation. Figure 4.9 shows the shape-corrected size distributions. Excellent agreement is observed between electron microscopy size distributions ($\mu = 50\ nm,\ \sigma = 5\ nm$) and the shape-corrected electrode particle impact results ($\mu = 49\ nm,\ \sigma = 13\ nm$).

4.5 Conclusions

To correctly size a given quasi-spherical particle, electron microscopy imaging is insufficient due to the inherent limitations of a two dimensional view. Without corresponding volumetric information provided by nanoimpacts, the characterization is incomplete. A common pitfall in describing nanoparticle sizes is the use of the radius of the corresponding sphere, which in many cases provides an apparently good experimental agreement but fails in the case, for example, of icosahedral particles. Hence, accurate sizing electron microscopy should be ideally complemented with the electrochemical coulometric sizing technique. The above highlights the importance of the geometrical aspects of the quasi-spherical nanoparticles and allows the description of the actual shape of individual nanoparticles. This is the first time the quasi-spherical nanoparticles have been studied by the electrode-impact technique. The approach has been subsequently extended to other geometries such as a nano-cubes [134] and nano-rods. [64]

Chapter 5

Studying agglomeration and/or aggregation processes using electrode-particle impacts

In the previous chapter it was reported that the electrode-particle impact technique can be applied to accurately size quasi-spherical particles. In this chapter the importance of agglomeration and/or aggregation processes is evaluated experimentally through a combination of light scattering approaches and electrochemical methods. Systems of strongly charged citrate-capped silver nanoparticles and of uncapped weakly charged bismuth oxide nanoparticles were investigated. The joint use of the different techniques established that reversible agglomeration takes place for both systems. This observation is of general importance for all colloids as it provides a feasible analysis technique for a wide range of systems with an ability to distinguish subtly different processes. The work has been published in *Analytical Chem-*

istry [127] and *Chemistry: A European Journal.* [135]

5.1 Reversible or not? Distinguishing agglomeration and aggregation at the nanoscale

Nanoparticles are incorporated in a wide range of commercial products [128] and find a diverse range of medical applications. [58] As production increases, the release of such nanomaterials into the environment inevitably takes place. Surface and waste waters are typically characterized by high ionic strength, and as a result NPs often show a tendency to cluster as electrostatic repulsion is minimized as discussed in Section 3.1.3. The knowledge of the aggregation/agglomeration state and the corresponding physico-chemical behaviour is vital for the understanding of their fate and distribution in such complex systems.

In the present thesis we follow the IUPAC definition of agglomeration and aggregation. According to this an agglomerate corresponds to the case when the dispersed particles are held together by only weak physical interactions and the whole process is *reversible*. An aggregate is defined as comprising strongly bonded colloidal particles, and the clustering process is *irreversible*. [7] The distinction can be crucial for many practical applications as agglomerates can be re-suspended via mechanical means, while irreversible aggregates cannot. Electron microscopy (EM) has been traditionally used to study the nanoparticulate solutions ex situ due to readily interpretable two dimensional visual information. However the study of ag-

glomeration/aggregation process through EM methods is hindered by potential drying artefacts and inability to study the kinetics of the process. [67] Cryo [136] and liquid [137] EM techniques have been developed to overcome these limitations. By taking time-series images one can observe agglomeration and/or aggregation processes. It can be hard to distinguish slow reversible agglomeration and irreversible aggregation due to the time scales of the image acquisition. In addition, clustering process can occur due to beam damage, further complicating the analysis. [138] Additional disadvantages of such approaches include the high cost of the sample holders, extensive training requirements and complex sample preparation.

Light scattering methods have been previously used to study agglomeration and/or aggregation [78, 139]. Dynamic light scattering (DLS) is an ensemble technique which involves the deriving the correlation function for the ensemble of the particles present in the solution as discussed in Section 2.2. DLS has found a wide range of applications due to the simplicity of sample preparation and highly automated particle size distribution analysis. In Section 2.2 it was stated that the Rayleigh scattering is stronger for larger particles as the scattering intensity is proportional to r^6 ($I \propto r^6$). As a result, particularly for the dynamic light scattering (DLS), the presence of large scattering particles can 'hide' the existence of smaller ones. The smaller particles can potentially have higher reactivity due to their high surface to volume ratio and consequently potentially possess danger to living organisms. An alternative light scattering technique nanoparticle tracking analysis (NTA) discussed in greater detail in Section 2.2 involves tracking of the diffusion of *individual* nanoparticles. Consequently unlike DLS, it is

less affected by the presence of the large clusters and has yielded accurate results for various metallic nanoparticulate systems [140], polymeric particles [81] and proteins. [141] NTA has proved to be an excellent technique in the laboratory setting, but can be challenged by the complex opaque environmental media and a relatively narrow recommended concentration range of $10^7 - 10^9$ $particles\ mL^{-1}$ [81]. UV-vis spectroscopy is another common technique, which can indicate that aggregation and/or agglomeration processes are taking place by constructing a time-dependent UV-vis absorption signals. [142] Unfortunately the size of the particles can only be easily resolved for highly monodisperse samples, which is not the case when clustering takes place.

In Section 2.3.3 an electrochemical method of electrode-particle impacts (EPI) was discussed. The method involves a relatively simple three electrode experimental setup that includes a microelectrode held at a potential at which reaction of interest takes place, shielded by a Faraday cage, low noise potentiostat and an analysis software. Upon impact with a working electrode, a particle can undergo oxidation or reduction, leading to an observation of a spike in the chronoamperogram. Information about the nature of the process can be extracted from the observed spikes by theoretical modelling of the thermodynamics and kinetics of the process, as well as the potentiostat filter response as discussed in Section 2.3.3.

In the present chapter we use a combination of particle-electrode impacts and light scattering methods (DLS and NTA) to analyze the effect of the ionic strength on the particle aggregation/ agglomeration state. EPI and light scattering techniques are conducted in the solution phase which al-

lows a direct comparison of the resultant size distributions. Chloride ions are omnipresent in the environment and in order to be useful an analytical technique must be suitable for a range of potential conditions, and for this purpose a range of potassium chloride electrolytes was chosen. Finally, we demonstrate that this unified approach utilizing several state of the art analytical techniques allows differentiation between agglomeration/aggregation states of nanoparticles in colloidal suspensions of high ionic strength.

5.1.1 Experimental

Commercial quasi-spherical citrate-capped spherical nanoparticles of $r = 50\ nm$ were used. DLS and NTA measurements were performed to provide solution-phase characterisation in variable ionic strength of potassium chloride. A Malvern Zetasizer was used to conduct DLS measurements. A Nanosight LM10 instrument was used to track the nanoparticles. NTA analysis was performed using NTA 2.3 software. All experiments were conducted in a three electrode cell, in a thermostatted Faraday cage held at $25.0 \pm 0.1°C$ and solutions degassed with nitrogen. For stripping voltamograms, a commercial Autolab Type 3 potenstiostat was used. A low-noise custom made potentiostat described in detail in Section 3.1.2 was used for the electrode-particle impacts. A macro glassy carbon electrode of radius of 1.5 mm was used for the dropcast stripping experiments. A random assembly of microelectrodes (RAM, 920 active fibres of radius 3.5 μm) supplied by Prof. Dr. Stephen Fletcher, (Department of Chemistry, Loughborough University) was used as a working electrode for electrode particle impacts. The ends of the

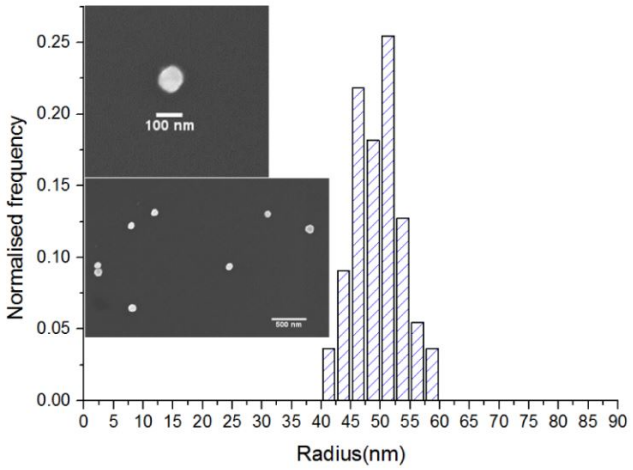

Figure 5.1: SEM images and the resultant size distributions for the silver nanoparticles.

fibers act as individual microdisks connected in parallel. The fibers are separated on average by 70 μm from each other in order to allow diffusional layer independence on the timescale of the experiment ($t < 60s$) and achieve a case 2 array response as discussed in Section 1.7. All potentials were measured against an SCE reference electrode.

5.1.2 Results and discussion

SEM images taken by a LEO Gemini 1530 microscope at 5 kV were used to size monomeric, non-aggregated nanoparticles ex situ in order to provide a starting point for the investigation. Image J software was used to produce the size-distributions. The resultant representative images and the size distribution are shown in Figure 5.1. The size distribution has the following characteristics: a mean radius of 50 nm and a standard deviation of 8 nm. The particles are mostly quasi-spherical and monodisperse.

Electrochemical Measurements

The oxidation potential of +0.14 V vs SCE for silver nanoparticles was established previously via stripping voltammetry in Section 4, Figure 4.4. Next electrode-particle impact experiments were conducted in variable concentrations of potassium chloride ranging from 20 mM to 2500 mM using the RAM as a working electrode held at a potential of +0.60 V vs SCE in order to ensure complete oxidation upon impact. A characteristic chronoamperogram is shown in Figure 5.2 for 100 mM KCl solution, no spikes were observed in the absence of particles (blue line). The observed spikes correspond to the oxidation of individual impacting particles (red line). The following reaction takes place upon collision:

$$Ag_{n(np)} \rightleftharpoons NAg^{+}_{(aq.)} + ne^{-} \tag{5.1}$$

where Ag_n is a silver nanoparticle comprised of n silver atoms and Ag^+ is a silver ion. The icosahedral shape correction was used in accordance with Section 4.2 to account for the deviation from the spherical geometry. Diffusional weighting in accordance with the Stokes-Einstein-Sutherland equation (see Section 4) was applied to the experimentally observed distributions in order to account for the higher probability of observation of particles with smaller radii due to faster diffusion of such particles.

In high ionic strength environments the particles are known to cluster, as the electrostatic repulsion is minimized due to the compression of the double layer around an individual particle. [143] The clustering process was induced by varying the concentration of supporting electrolyte (20-2500 mM).

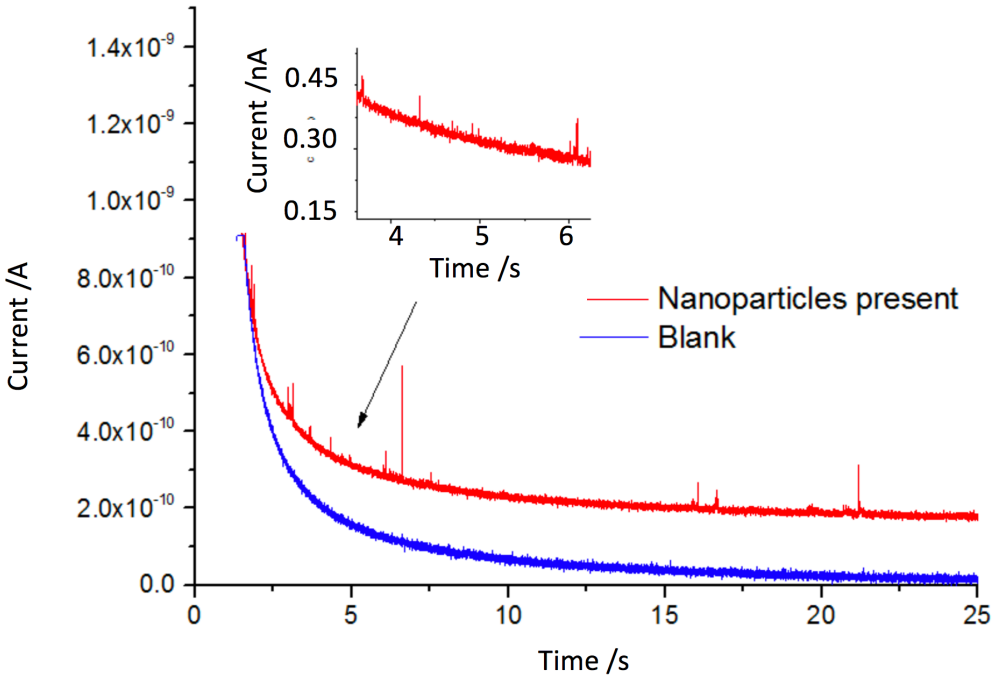

Figure 5.2: A typical chronoamperogram observed at a potential of +0.60 V vs SCE reference electrode in 100 mM KCl, in the presence and absence of nanoparticles, the curves have been offset by 1.5×10^{-10} A for clarity.

Particle-electrode impact experiments were performed and the resultant particle size distributions analyzed.

In a suspension, where an agglomeration/aggregation process takes place, the concentration of the diffusing species decreases, which in turn leads to a decreased number of the observed impacts. In order to test the hypothesis five scans were performed in succession with a 3 min pause between the scans. Figure 5.3 shows the observed number of impacts per scan as a function of number of scans. It can be seen that for 20 mM KCl concentration the number of impacts remains virtually constant. For higher concentrations (above 20 mM) of KCl, a rapid decrease in the number of impacts is observed after the first scan, indicative of a clustering process taking place. The variability between the scans arises due to the stochastic nature of the electrode-particle impacts. If the clustering process is reversible, the re-dispersion caused by mechanical agitation, such as bubbling an inert gas or sonication, will result in an increase in the observed number of impacts. This hypothesis was tested by recording the frequency of the impacts observed in a given scan in 100 mM potassium chloride and plotting it against the scan number as shown in Figure 5.4. This observation provides evidence for an aggregation/agglomeration process taking place. Initially, at the beginning of experiment, a sharp decline is observed; after the solution is bubbled with nitrogen an increase in the number of impacts per scan is observed.

The effect of the dispersion method was investigated by conducting a set of experiments using a sonic horn. The obtained size distributions by sonic horn and bubbling dispersion methods are shown in Figure 5.5 and appear almost identical. This indicates that the dispersion method does

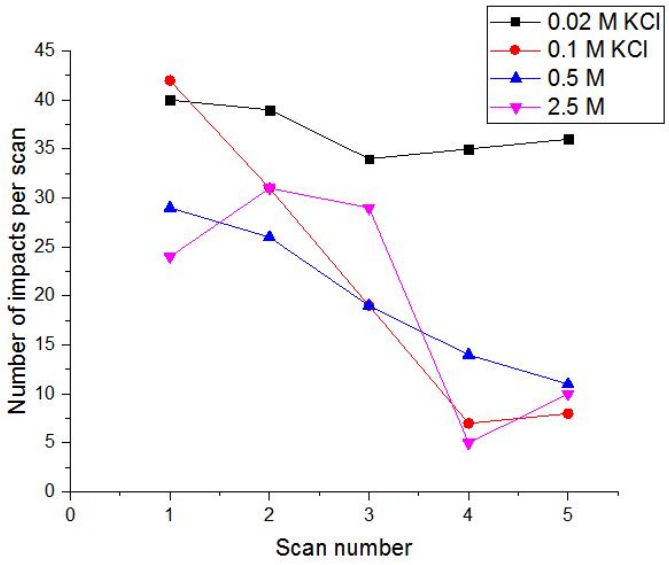

Figure 5.3: Frequency of impacts (averaged over three runs) observed over five consecutive scans with a 3 minute pause between the scans in different KCl concentrations, potential of +0.60 V vs. SCE,

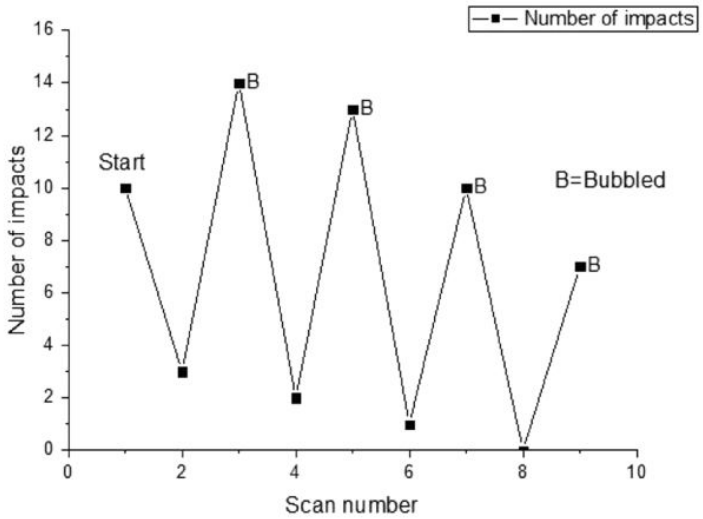

Figure 5.4: Observed frequency of the impacts (averaged over three runs) and the effect of nitrogen bubbling, potential of +0.60 V vs SCE reference electrode, 100 mM KCl

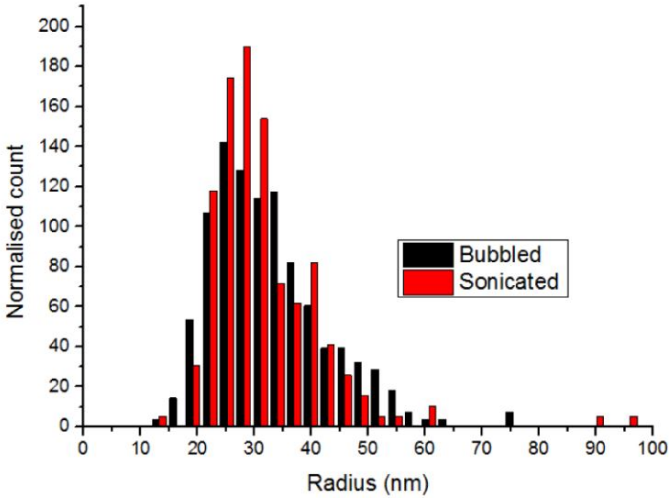

Figure 5.5: Size distributions obtained by nanoimpacts for nitrogen bubbling and sonication techniques at a potential of 0.60 V vs SCE reference electrode.

not significantly affect the size distributions as the resultant particles are of similar mean sizes. Consequently all further measurements were performed using nitrogen bubbling to re-disperse the particles.

The size distributions obtained from nano-impacts experiments at different ionic strengths are shown in Figure 5.6. The distributions generally show a significant number of small particles with a wide standard deviation and a general lack of expected large agglomerates. With increasing ionic strength of electrolyte, in accordance with the Derjaguin, Landau, Verwey, and Overbeek (DLVO) theory, increased aggregation/agglomeration is expected, [144–146] but is not observed experimentally by the nano-impacts technique. There is some variation within the distributions for increasing electrolyte concentration with higher ionic strength leading to an apparent decrease in the observed mean size. In particular for 500 and 2500 mM KCl the mean size of the nanoparticles is smaller compared to the monomeric size

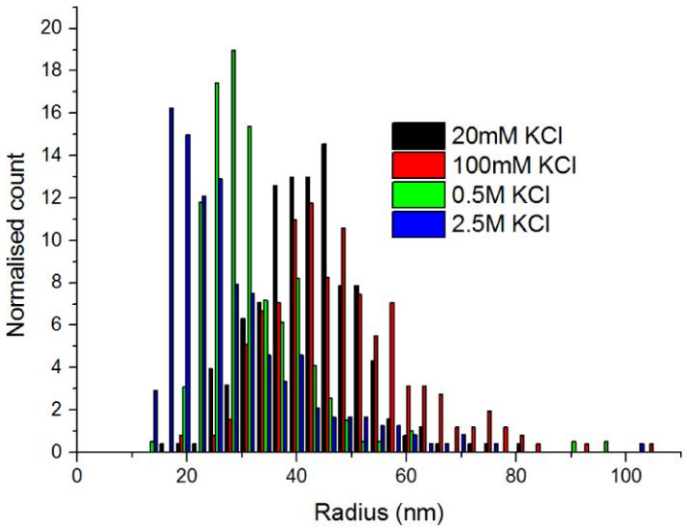

Figure 5.6: Size distributions obtained by nano-impacts for the different KCl concentrations, at a potential of 0.60 V vs SCE.

obtained from the SEM images. It should be considered that nano-impacts unlike light-scattering techniques are biased toward smaller NPs as discussed in Section 4. However despite the lower probability of large cluster collision, such events should be observable. Please note that the nanoimpact technique is able to detect single (unclustered) large particles ($r = 50\ nm$) as shown in the work by Bartlett *et al.* [66] and consequently should be capable of detecting large aggregates/agglomerates, but in our series of experiments, such particle clusters were rarely if ever detected, as evidenced by the observed size distributions.

Light Scattering Measurements

DLS and NTA were used to size the particles in 0, 20, 100 and 500 mM potassium chloride concentrations. The dynamic light scattering Z-average was used to characterise the distributions shown in Figure 5.7a. The sizing of

the particles in de-ionised water was comparable to the distribution obtained from SEM imaging with a Z-average of 50 nm and a standard deviation of 32 nm. As the concentration of electrolyte was increased a general increase in the Z-average value and a broadening of the distributions were observed. This observation is consistent with the DLVO theory and is indicative of a significant degree of cluster formation. DLS is inherently biased towards the detection of larger nanoparticles and in order to overcome this limitation, the suspensions were investigated using nanoparticle tracking analysis. In a solution of de-ionised water and 20 mM KCl, distributions comparable to SEM sizing were observed with respective means of 50 and 52 nm and standard deviations of 32 and 38 nm. Nanoparticles are known to stick to glass substrates and form clusters. The presence of such clusters can affect scattering of the laser beam and lead to errors in the DLS size distribution.

Nanoparticle tracking analysis is less affected by the sticking of such clusters as the algorithm compensates for the presence of stationery agglomerates or aggregates. The NTA experiment provided additional evidence of agglomeration and/or aggregation process taking place due to a shift in the mean size of the particles and a significant increase in the standard deviation of the distribution. DLS and NTA measurements yielded consistent size distribution indicative of the clustering process taking place in the solution phase and not at the glass walls.

The data obtained using electrode-particle impacts, light scattering methods and SEM, for convenience of the reader are summarised in Table 5.1.

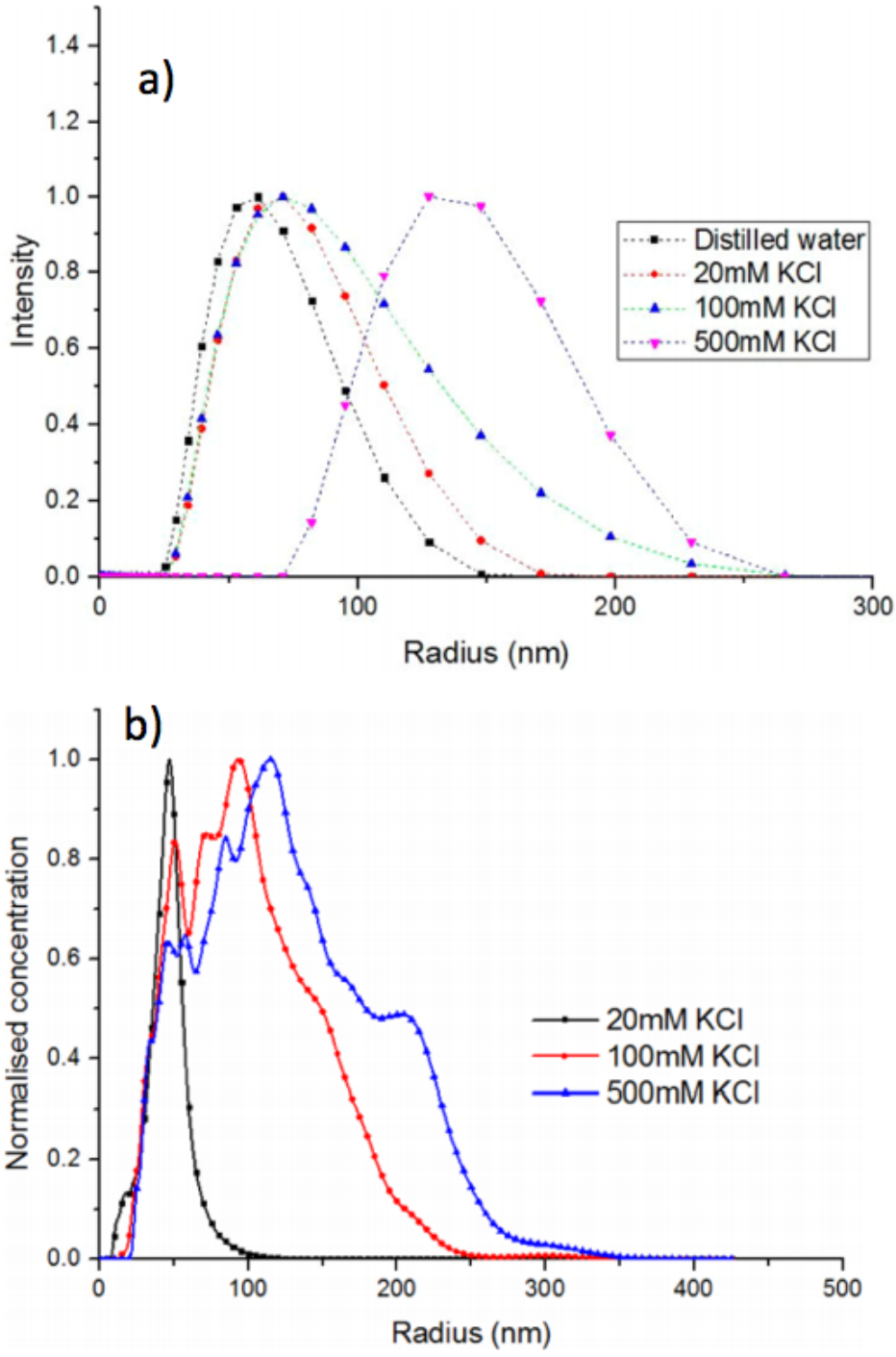

Figure 5.7: a) Normalized size distributions obtained for the different KCl concentrations using DLS b) Normalised size distributions obtained for the different KCl concentrations via NTA.

Table 5.1: Mean radius and standard deviation of the size distributions obtained using nano-impacts, NTA, DLS and SEM.

	Nano-impacts		NTA		DLS		SEM	
Electrolyte Concentration (mM)	Mean radius	Standard Deviaton	Mean radius	Standard Deviaton	(Z-ave)/2 (nm)	PdI	Mean radius	Standard Deviation
0	n/a	n/a	50	32	54	0.18	50	8
20	44	9	52	38	66.4	0.27	n/a	n/a
100	49	10	103	46	69.7	0.149	n/a	n/a
500	36	9	123	60	181.65	0.322	n/a	n/a
2500	30	11	N/A					

Proposed model

Nanoimpacts consistently yielded the particle size of 30-44 nm indicative of mostly monomeric species being detected. In contrast NTA and DLS provided evidence for the aggregation and/or agglomeration of the sample (50-180 nm) and the presence of large clusters. In order to understand the apparent difference in results the basis of the two techniques are evaluated. Nano-impacts sizing relies on a direct collision of a nanoparticle with an electrode, which allows subsequent oxidation to take place. The size distributions shown in Figure 5.6 show a prevalence of nanoparticle of smaller 30-44 nm radius. At 20 mM KCl concentration a lower radius is observed; a potential explanation is incomplete oxidation of the large silver particles due to lack of supporting electrolyte. While previous reports have shown that 20 mM KCl is sufficient for oxidation of smaller particles, this may not be the case for larger particles. At higher concentrations (above 100 mM KCl) the lower particle size can only be attributed to de-agglomeration of the large clusters into small, fast diffusing monomers as the conditions of the experiment are fully supported and large clusters are fully oxidised upon impact. [66]

On the other hand DLS and NTA both demonstrate an apparent presence of a large number of clusters with the whole size distribution skewed toward

such particles as shown in Figure 5.7. The fact that agitation of the electrolyte increases the frequency of the observed impacts as shown in Figure 5.4 for the nanoimpact experiments and the resultant size distribution is not affected by the dispersion technique involved suggests that the underlying clustering process is *reversible* and thus has to be agglomeration instead of *irreversible* aggregation. Based on the above evidence one can propose a mechanism for the reversible process taking place:

$$NM_n \rightleftharpoons (N-1)M_n + M \rightleftharpoons (N-2)M_n + 2M \rightleftharpoons further\ dissociation \quad (5.2)$$

where M is a monomeric particle, and M_n is a cluster composed of n monomers. An effective equilibrium develops between the agglomerated clusters and monomeric species in the bulk solution. Within the close proximity of the electrode, the equilibrium between monomeric and clustered species can be perturbed by electrolysis. The faster diffusing monomeric species are depleted due to electrolysis and the system aims to return to equilibrium via dissociation of larger clusters into monomers. Large agglomerates have low diffusion coefficients in accordance with the Stokes-Einstein-Sutherland equation (Equation 2.4), and as a result are rarely observed in the nanoimpacts experiment. By contrast the smaller particles with higher diffusion coefficient have a higher probability of collision and as a result dominate the observed distribution. At the electrode surface the concentration of nanoparticle monomers is thus depleted most, and as a result the equilibrium is shifted in favour of the smaller particles. By contrast light scattering techniques do not perturb such equilibrium, and the solution is consequently dominated

by the presence of large clusters. The position of such equilibria will be dependent on the ionic strength of the electrolyte, size, and coating of the nanoparticles.

5.1.3 Conclusions

This work has demonstrated that in order to distinguish between agglomeration and aggregation processes in high ionic strength environments, electron microscopy imaging and light scattering techniques are insufficient due to the inherent limitations. Without the corresponding size-distribution information provided by nanoimpacts the characterization is incomplete. Hence it is evidenced that the light scattering techniques such as DLS and NTA can be ideally complemented with the electrochemical coulometric sizing technique to gain hitherto non-accessible information on the agglomeration/aggregation state. It is important to note that the use of DLS as a stand-alone light scattering technique may lead to inaccurate size distributions due to the sticking of the nanoparticles to the walls of the measurement cell and subsequent clustering. Nanoparticle tracking analysis is capable of eliminating such problems and confirms that agglomeration takes place in the solution. The joint use of these techniques allowed for clearly identifying the presence of reversible clusters, that is agglomeration, instead of aggregation occurring in the system shown. Analysis performed in this work has been subsequently extended to a system of uncapped bismuth oxide nanoparticles and will be discussed in the next section.

5.2 Bi_2O_3 Nanoparticle Clusters: Reversible Agglomeration Revealed by Imaging and Nano-Impact Experiments

In the previous section the importance of reversible agglomeration has been demonstrated for metallic citrate-capped silver nanoparticles in high ionic strength environments. The capping provides electrostatic repulsion between the particles and stabilises the suspension. In the present section a system of uncapped bismuth oxide particle is studied. The absence of capping simplifies the experimental parameters and allows us to probe the kinetics of the agglomeration/deagglomeration process. Further microscopy evidence is presented in support of the proposed model of cluster dissociation. The generality of the reversible agglomeration is highlighted. Reversible agglomeration phenomenon provides a way of preparing highly monodisperse electrode arrays with minimal clustering. In addition bismuth, and its oxides find uses in a wide variety of industrial [147] and medical applications. [148] A particular example is barium potassium bismuth oxide, which is one of the highest-temperature oxide superconductors. [149] Understanding the behaviour of bismuth compounds on a single nanoparticle levels may provide further insights into its reactivity and provide directions for future research.

5.2.1 Experimental

Bismuth oxide nanoparticles were sized using nanoparticle tracking analysis (Nanosight LM10 instrument). Electrochemical measurements were per-

formed with assistance from Mr (now Dr) Thomas R. Bartlett (Department of Chemistry, University of Oxford). The potentiostat used was an Autolab PGSTAT 302N (Metrohm-Autolab, Netherlands) fitted with an ECD module. All experiments were conducted in a three electrode cell, in a thermostated Faraday cage held at $25.0 \pm 0.1°C$ and solutions degassed with nitrogen. All potentials were reported against the Mercury-mercurous sulfate electrode (MSE E=+0.64 V vs NHE) Stripping cyclic voltammetry was used to determine suitable potentials for the impact experiments. The Bi_2O_3 NPs suspension was prepared by sonicating de-ionised water with the NP powder for 10 minutes. A glassy carbon macro electrode ($r = 1.5\ mm$) was used as a working electrode, modified via dropcast with a known concentration of Bi_2O_3 to achieve a loading of 0.69 nmoles. The electrode was dried under nitrogen and stripping voltammetry performed in 0.1 M NaOH. The nanoparticles were electrochemically sized via the electrode-particle impact method using a carbon fibre microelectrode ($r = 3.5\mu m$). The resultant size distributions were critically analysed and compared to NTA results. Scanning electron microscopy was used to image the NP dropcast and nano deposits after the impact experiments and size the impacted particles.

5.2.2 Results and Discussion

Suspensions of Bi_2O_3 nanoparticles were dropcast on the glassy carbon electrode and allowed to dry under nitrogen. Cyclic voltammetry was performed in 0.1 M NaOH and the resultant typical voltammogram is shown in Figure 5.8. A clear sharp reductive peak (labelled C1) is observed at -1.33 V vs MSE

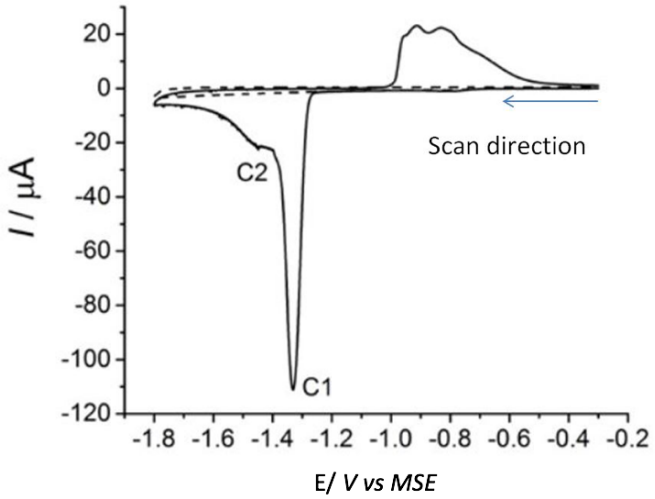

Figure 5.8: Cyclic stripping voltammetry in 0.10 M NaOH, start potential of -0.30 V vs MSE, at $50mV\ s^{-1}$ blank GC electrode (dashed line), 0.69 nmoles of Bi_2O_3 NP modified GC (solid line)

consistent with the previous reports [150] of an overall 3 electron reduction reaction of bismuth oxide to bismuth metal:

$$Bi_2O_{3(np)} + 2OH^- \rightleftharpoons 2BiO^-_{2(aq.)} + H_2O \ \ (slow\ process) \tag{5.3}$$

$$BiO^-_{2(aq.)} + 2H_2O + 3e^- \rightleftharpoons Bi_{(s)} + 4OH^- \ \ (C1) \tag{5.4}$$

The broad shoulder (labelled C2) at -1.45 V vs MSE was attributed to the further reduction of BiO_2^- species, which are continuously generated on the time scale of the scan via reaction 5.3 provided that the reaction 5.3 is slow in comparison to the experimental scan rate of 50 $mV\ s^{-1}$. The C2 process would not be present if the formation of the BiO_2^- species was fast. The

overall reaction is:

$$Bi_2O_{3(np)} + 3H_2O + 6e^- \rightleftharpoons 2Bi_{(s)} + 6OH^- \quad (C2) \tag{5.5}$$

The reaction pathway is dependent on the concentration of OH^- and the rate of BiO_2^- formation with a $3e^-$ reduction process being dominant under conditions of sufficient OH^- concentration and a $6e^-$ process occurring in the absence of hydroxide ions. Upon the reversal of the potential a broad oxidation ('stripping') peak is observed at -1.0 V vs MSE, which corresponds to bismuth metal oxidation and formation of BiO_2^- species. In accordance with Equations 5.4-5.5 the C2 process causes a release of hydroxide ions. The reaction pathway was investigated further by performing three consecutive stripping cycles. The resultant cyclic voltamograms are shown in Figure 5.9. The C2 process is no longer observable after the first scan, consistent with the production of BiO_2^- in the first scan (black line), reduction to Bi metal and subsequent oxidation to BiO_2^- allowing the dominance of the C1 process on the subsequent scans. During the scans, the size of the oxidation peak remains approximately constant, with the only significant change being the size of the reduction peak between scan 1 (black line) and scan 2 (red line), with this ending up equating to that of the oxidation peak. This strongly indicates that the occurring oxidation process is dominated by the reverse of the $3e^-$ process C1 and is consistent with the proposed hypothesis.

SEM images of the dropcast (shown in Figure 5.10), revealed presence of large agglomerate and/or aggregated clusters. This aggregates/agglomerates forming during drying can potentially inhibit the diffusion of the OH^- ions

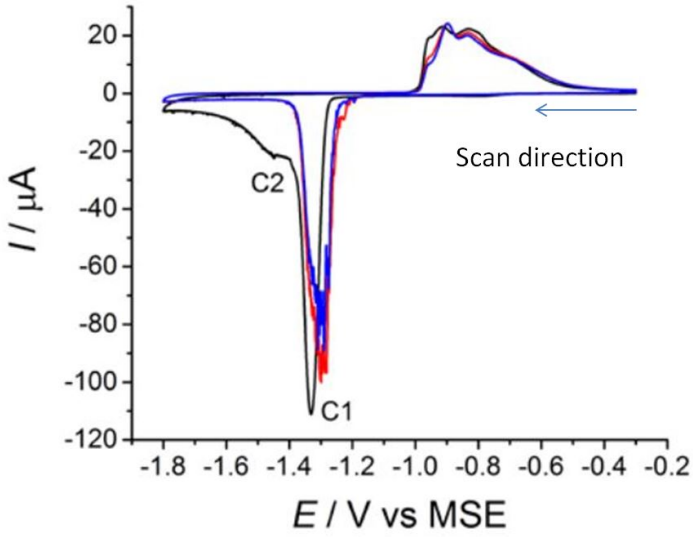

Figure 5.9: Consecutive scans of Bi_2O_3 modified glassy carbon electrode start potential of -0.30 V vs MSE, at $50mV\ s^{-1}$: scan 1 (black line), scan 2 (red line), scan 3 (blue line).

into the clusters on the first scan. As a result the hydroxide concentration is effectively limited, thereby allowing C2 process to take place. Upon further voltammetric cycles the process is no longer limited by the formation of BiO_2^- species and consequently only C1 peak is present.

Initially current-time transients were conducted at -1.70 V vs MSE with and without 40 pM NPs in 0.10 M NaOH. As seen in Figure 5.11, current spikes were observed only when NPs were present indicating the reduction of Bi_2O_3 NPs to metallic bismuth. Spherical approximation was used to determine the size of the particles in accordance with Equation 1.7.3 (Section 2.3.3). A $3e^-$ transfer was assumed due to high mass transport of OH^- ions to an impacting particle. [151] Particle-size potential dependence was investigated by running chronoamperometric measurements at different potentials. The resultant plot is shown in Figure 5.12. It can be seen that at poten-

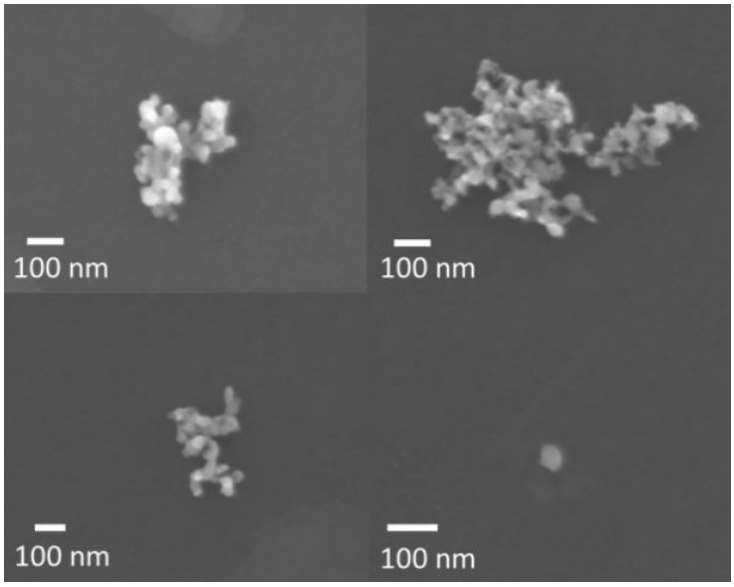

Figure 5.10: SEM of drop-cast NPs showing Bi_2O_3 clusters and monomer.

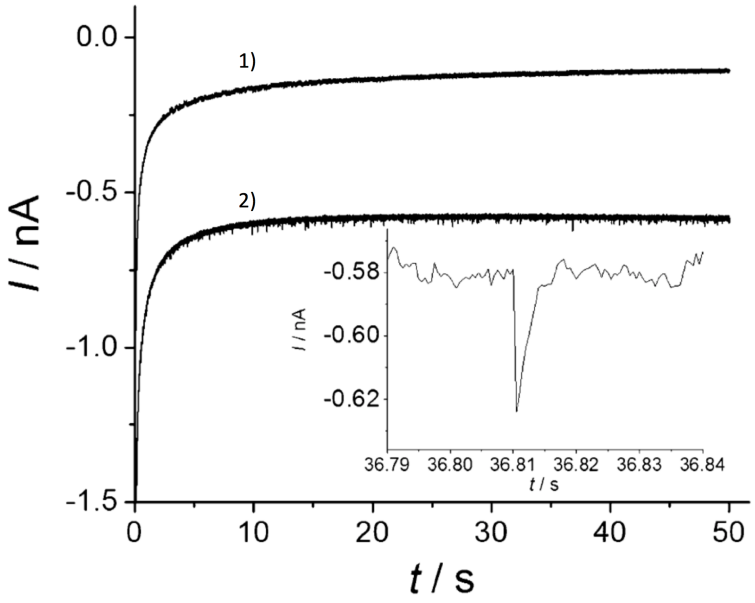

Figure 5.11: Current-time chronoamperogram at a CF microelectrode held at -1.70 V vs MSE in 0.10 M NaOH (black line 2) No NPs (black line 1) 40 pM Bi_2O_3 NPs. Increase in background current on addition of NPs attributed to reduction of small amounts of solubilised bismuth hydroxide species. Insert shows a zoomed in image of an example NP impact current trace.

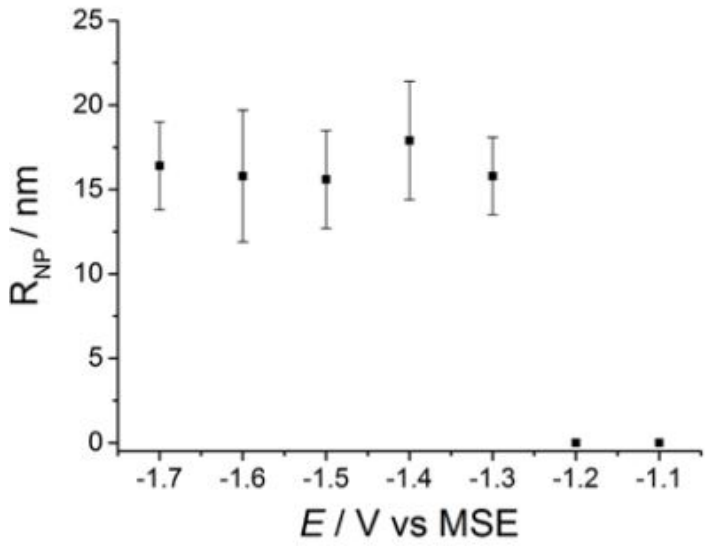

Figure 5.12: Average radius of NP as a function of held potential during current-time transient

tials more negative than -1.30 V vs MSE, the particle size remains constant ($r \approx 17\ nm$), thereby confirming that full reduction takes place.

The stability of the suspension was studied by Zeta Potential Measurements. Zeta potential measurements of the NPs in 0.10 M $NaNO_3$ showed the particles were negatively charged and have a zeta potential of -11 mV. This indicates that the suspension might become unstable in the long term as discussed in Section 2.2.4 and likely to agglomerate and/or aggregate over long periods of time.

To investigate the solution phase species further, NTA measurements were conducted under identical experimental conditions to the EPI experiments. Figure 5.13 shows the resultant size distributions. The modal value of $r = 19\ nm$ corresponds to the manufacturer's specification of the mean radius of 19 nm. By contrast to the electrode-particle impacts, NTA analysis indicated the presence of large clusters of particles with the mean radius be-

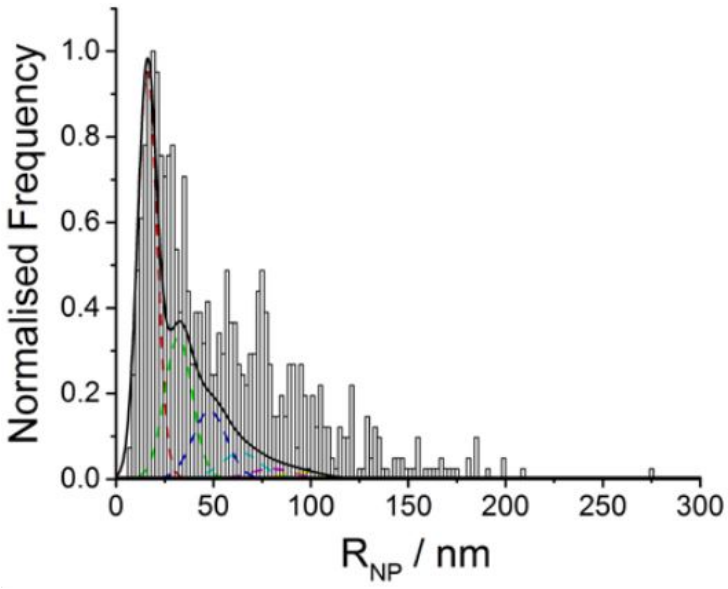

Figure 5.13: NP distribution as found from NTA, showing small deviations from the entropy only model

ing significantly larger. Note that the fitted curve corresponds to an entropy of mixing distribution and will be discussed in detail in Chapter 7. The presence of large clusters provides evidence for agglomeration/aggregation process taking place.

The time-dependence of the agglomeration and/or aggregation process was investigated by conducting electrode-particle voltammetry. The first scan was recorded 2 minutes after the addition of particles to the electrolyte. The resultant average size of the detected particles was plotted as a function of time and is shown in Figure 5.14. No significant change in the average NP radius can be observed across the 20 minute time period or during a single 50s chronoamperogram, with the average NP radius remaining constant at approximately 17 nm with a standard deviation of 3 nm. This suggests that the NPs detected by nano-impacts are confined to monomeric

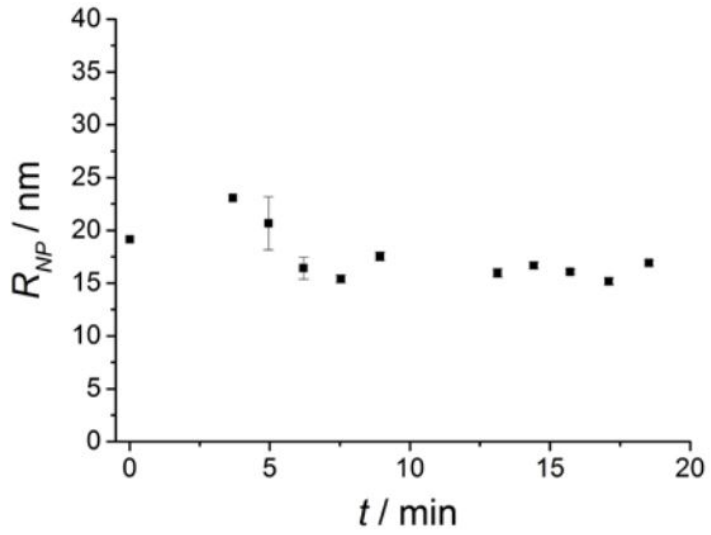

Figure 5.14: Mean radius of NP vs start time of 50 second current-time transient (approximately 30 impacts were recorded per data point)

NPs only, with no NP clusters detected. This is consistent with the modal size of the particles (19 nm) found by NTA analysis. This difference of 2 nm in radius matches that calculated for the loss of material by formation of some soluble $Bi(OH)_x^{3-x}$ species. The amount of material lost was calculated using Medusa equilibrium software (I. Puigdomenech, MEDUSA, available from: https://www.kth.se/en/che/medusa/downloads-1.386254.) at the concentrations and pH stated for nano-impacts experiments. The calculation assumes that equilibrium between Bi_2O_3 and $Bi(OH)_x^{3-x}$ species is reached prior to experimentation. As a result one can conclude that the observed mean particle size of 17 nm is consistent with the detection of monomeric species. This observation is contrasted by the NTA size distribution, which clearly shows presence of large clusters with larger mean radii. The observations can be rationalised by considering the particles to be in a dynamic equilibrium between the agglomerated clusters and monomeric species. Elec-

trolysis at the electrode surface disturbs the equilibrium. Similar to the case of citrate-capped silver nanoparticles as discussed previously, the population of fast-diffusing monomers is depleted and the equilibrium is shifted towards further release of monomeric species from the cluster. Large slow diffusing agglomerates have a low probability of a collision and are rarely, if ever, observed. The theoretical prediction of the expected number of impacts is further complicated by the near-wall hindered diffusion. In contrast to the electrochemical methods, NTA does not perturb this equilibrium and consequently shows the presence of large clusters.

Further evidence of reversible agglomeration were provided by ex situ imaging of a glassy carbon electrode substrate after the impact experiments were conducted. Glassy carbon substrate plate was used as a working electrode and immersed in a solution of 0.1 M NaOH containing 40 pM Bi_2O_3 nanoparticles and held at a potential of -1.60 V vs MSE. Upon impact Bi_2O_3 is reduced to metallic bismuth and the resultant nano-deposits were imaged via scanning electron microscopy. Figure 5.15a. shows that after the impacts, the GC electrode is covered with nanoscale bismuth deposits. Clearly monomeric particles are observed. The size distribution of these deposits is shown in Figure 5.15b (red bars) and the corresponding size distribution obtained via electrode-particle impact method (black bars). The mean size of the imaged nano-deposits was found to be 14 nm with a standard deviation of 3 nm, which is in good agreement with that calculated from the impact voltammetry ($\mu = 17\ nm$, $\sigma = 3\ nm$). Consequently due to the fact that no cluster were detected, it has been concluded that equilibria processes between agglomerated and monomeric species take place in accordance with

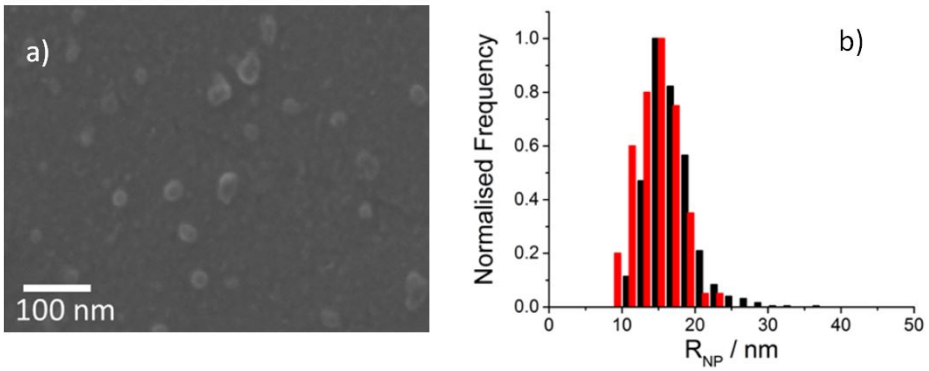

Figure 5.15: a) SEM image of GC surface after 5 min deposition of Bi_2O_3 NPs at -1.60 V vs MSE in 40 pM Bi_2O_3 and 0.10 M NaOH, b) Comparison of size distributions obtained from (black bars) NP impacts (red bars) SEM of nanodeposits

Equation 5.2 and the process is shown schematically in Figure 5.16. Fast-diffusing monomeric species are electrolysed at the electrode; consequently the equilibrium between the agglomerates and monomeric species is shifted towards generation of further monomers. The diffusion of large clusters is slow and consequently they are rarely, if ever, detected.

5.2.3 Conclusions

The rapid agglomeration/deagglomeration of uncapped bismuth oxide nanoparticles has been confirmed through electrode-particle impacts and light scattering methods. The joint use of techniques allowed distinguishing between irreversible aggregation and reversible agglomeration. It has been demonstrated that reversible agglomeration is a general phenomenon observed for the systems with different inter-particle forces at play and needs to be taken into account for practical sensor design. The non-observation of large clusters via electrochemical means is not always indicative of the absence of

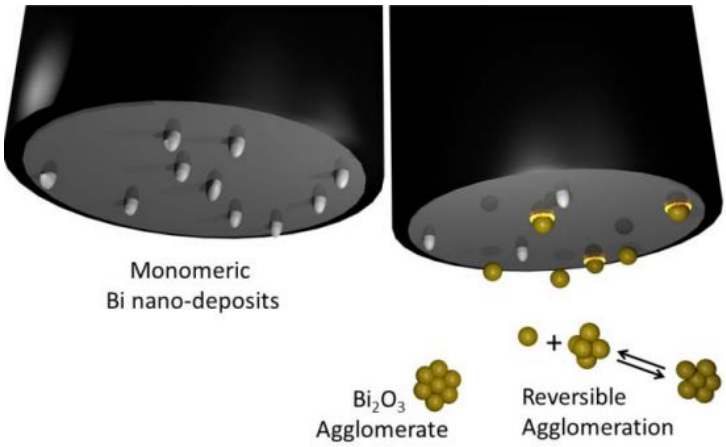

Figure 5.16: Reversible agglomeration of Bi_2O_3 NPs approaching the electrode, resulting in the deposition of monomeric Bi nano-deposits.

such clusters in the bulk solution. An additional important highlight of the work is that the deposited metallic particles are mostly monomeric on the electrode surface. As a result, a new way of producing electrode arrays is envisaged without aggregation/agglomeration of the particles. This is of significant importance as the mode of mass transport is significantly affected by the aggregation state of the particles as discussed in Section 1.7 and is a challenge for conventional deposition techniques. In the next chapter the thermodynamic driving force behind the agglomeration process will be investigated theoretically and the role of entropy of mixing will be demonstrated in determining the experimentally observed distributions.

Chapter 6

A Thermodynamic View of Agglomeration

The thesis has so far addressed reversible agglomeration observed experimentally for suspensions of capped and uncapped particles. In the present chapter the fundamental driving forces for agglomeration are discussed. We present a theoretical model based on the entropy of mixing of an agglomerating system. The clusters are treated as agglomeration states and are considered to be equivalent in terms of their energy. The resultant predicted distribution of monomers, dimers, trimers *etc.* is predicted and compared to the experimentally observed size distribution. The key finding is that some degree of agglomeration is expected even in the presence of mildly repulsive forces between the particles. The work has been performed in collaboration with Dr. Enno Kätelhön (University of Oxford, Department of Chemistry) and published in *Journal of Physical Chemistry C* using a numerical solution of the problem [152] and *ChemPhysChem* reporting an analytical solution. [153]

6.1 A thermodynamic view of agglomeration: numerical approach

Understanding agglomeration processes in nanoparticulate and colloidal systems is key to the development of future generation of nano-devices and biomedical drug carriers. Most previous approaches aimed at understanding this phenomenon have focused on the forces acting between the particles and the resultant stability of the suspensions. An example of such approach is the famous Derjaguin-Landau-Verwey-Overbeek (DLVO) theory. [154,155] It involves the consideration of long-range inter-particle electrostatic repulsions and van der Waals attractive forces and aims to predict the colloidal stability of a system with respect to agglomeration and aggregation. [145,156,157] The main disadvantage of such approaches is that while predicting the stability criteria, they offer limited information about the cluster size distributions of the agglomerating particles. With the advent of modern computers, potential mean force (PMF) method became feasible and allowed modelling of the temporal evolution of wide range of systems from graphene [158] to proteins [159]. The main limitations of the PMF method is that while providing highly accurate results, they feature an inherent complexity and can require exceedingly long computation times for large systems. In the present work we develop a simple model based on the thermodynamics of a system. The model is general and applicable to a wide range of systems as it involves minimal assumptions about the interaction between the particles.

The concept of maximum-entropy probability distribution has been applied to a diverse range of scientific [160] and economic problems. [161] In

accordance with the maximum-entropy principle, provided that some partial information about an experimental variable is known, a probability distribution must be chosen, which is consistent with the given information and has the maximum uncertainty associated with it. [162] Consequently in the absence of additional information the distribution with the highest degree of entropy will be the most probable. In the present work, we consider clustering system as having multiple states, corresponding to the agglomerates (dimer, trimer, *etc.*) comprised of multiple individual monomers. The entropy of mixing of the system is dependent on the population of the individual states and the overall configuration. Provided that the entropy for a given configuration can be evaluated, the most probable distribution of the particles in a system can be found in accordance with the maximum-entropy principle. In this way, presuming stability of the system, we are able to generate predictions of particle size distributions, specifically the number of monomer, dimer, trimer, etc. units which are in remarkably good agreement with experiments, and further explore the role of the enthalpy of formation of agglomerates in this process, where the entropy of mixing based approach shows that some agglomeration is expected even in the presence of mildly repulsive forces between the particles. The resultant maximum-entropy distribution is consistent with log-normal distribution shape, which is commonly observed in nature [163], hence we speculate that for such distributions, entropy may be at play.

6.1.1 Experimental

The nanoparticles were characterised ex situ using scanning electron microscopy. The particle suspension was sonicated for 10 s prior to dropcasting on a transmission electron microscope (TEM) sample holder that was modified to be used in the SEM. Figure 6.1a shows the representative images of the particles, which were used for particle size-determination. Image analysis was performed using the software ImageJ and yielded a mean size of 98.7 nm with a standard deviation of 17.0 nm, which is in good agreement with the manufacturer's specification of 100 nm as shown in Figure 6.1b.

In situ characterization was performed by nanoparticle tracking analysis. The Brownian motion of the particles was recorded for a period of 60 seconds at a temperature of at $25.00 \pm 0.05 °C$ using manual gain and shutter settings. Raw tracking data were obtained and analyzed through the NTA 2.3 software environment, which was used to construct the resulting size distribution histograms. Measurements were repeated three times, while different areas of the sample were chosen to ensure reliability and to obtain a representative view of the sample.

6.1.2 Theory

In this section a numerical method is used to evaluate the entropy of mixing of a nanoparticulate suspension. As a result a finite number of monomers (N_{init}) initially in the system is used. The monomers are able to reversibly form clusters up to i_{max} individual monomers and all clusters are equivalent in energy, a necessary assumption for a system where only entropy is present.

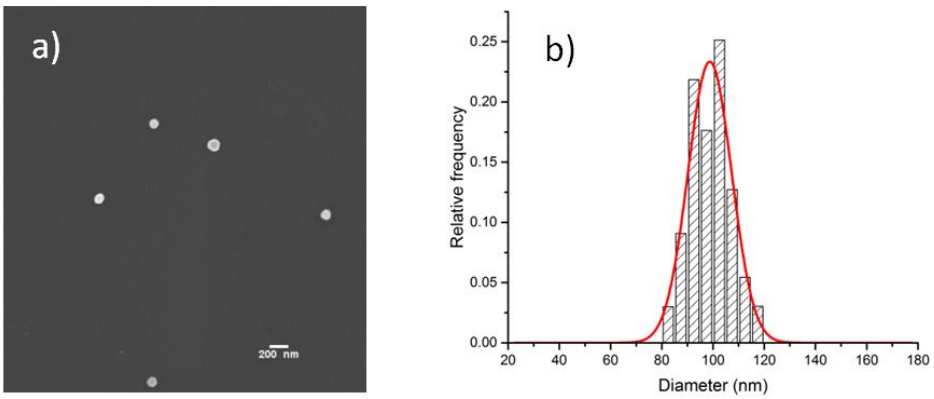

Figure 6.1: a) Scanning electron microscopy image of the citrate-capped silver nanoparticles, b) Size distribution obtained from the SEM image analysis using Image J software and the least-squares fitted Gaussian distribution (red line)

In the absence of interactive forces, the most probable distribution of agglomerate states will be the distribution that features the highest entropy of mixing. As a result the most probable distribution can be determined by maximizing the entropy, S, of the system [162, 164]:

$$max(S = -k_B N \sum_{i=1}^{i_{max}} x_i ln(x_i)) \tag{6.1}$$

where:

$$N = \sum_{i=1}^{i_{max}} N_i \tag{6.2}$$

and N is the total number of entities in solution after the agglomeration process, N_i is the number of agglomerates comprising i individual monomers (i.e., i = 2 for a dimer, i = 3 for a trimer, etc.), and $x_i = N_i N^{-1}$ is the mole fraction of each type of agglomerate present in the solution such that $\Sigma_i x_i = 1$. For a finite number of particles the entropy of each individual configuration

can be evaluated numerically (see Section Numerical Simulation for further details) subject to a constraint that the total number of particles in the system remains constant:

$$N_{init} = \sum_{i=1}^{i_{max}} iN_i \tag{6.3}$$

Perturbations arising from particle interactions

In non-ideal systems, interactions between particles take place. Consequently the most probable distribution no longer has the maximum entropy, but the minimum in Gibbs energy, G, needs to be considered. The definition of Gibbs energy is [13]:

$$G = H - TS \tag{6.4}$$

where H is the enthalpy and T is the temperature. Agglomeration causes a change in enthalpy of the system. One can regard the clustering process as the formation of virtual 'bonds' between the individual monomers. These 'bonds' are formed at the contact points between two monomers and may feature either positive or negative enthalpies for the cases of repulsive or attractive interactions, respectively. A dimer involves one contact point, trimers can involve two or three contact points, which is dependent on the agglomerate geometry, the complexity increases with the number of monomers in a cluster. The contact point can be assumed to have a constant energy value for the purpose of the present model and considering the total number of contact points present in each agglomeration state, the enthalpy of the system can be estimated:

$$H = \sum_{i=1}^{i_{max}} N_i H_b n_i \tag{6.5}$$

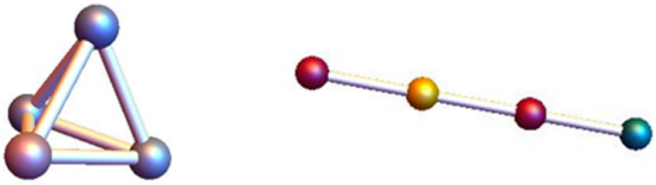

Figure 6.2: Two limiting agglomeration states of a tetramer. On the left, a close packed structure is shown featuring the maximum number of possible contact points; on the right, the case of the minimum number of contact points forming a chain-like structure is sketched.

where H_b is the enthalpy per contact point and n_i is the number of contact points for a given agglomerate state, which depends on the respective agglomeration model. It is difficult to determine the number of contact points n_i as it is a function of the strength of nanoparticle interaction. If we consider strongly attractively interacting particles, one would expect to observe closely packed structure with multiple contact points between the monomers. [165] While on the other hand, strong repulsive interaction would lead to fewer connections due to the associated energy cost and the resultant chain-like geometry. We investigate distributions for the case of a minimum number of contact points observed in chain-like structures and compare it to the case of the highest possible number of contact points that is observed in the case of close packing. These two extreme configurations are shown in Figure 6.2. Real systems are likely to adopt an intermediate between the two limiting cases. In Table 6.1 the number of contact points is shown for either model and various agglomerate states. The presented model is limited to the number of contact points between the monomers and does not take into account the shape effect.

Table 6.1: Number of contact points per agglomeration state for two different agglomeration models.

Agglomerate state	Number of contact points in the chain model (strong repulsion)	Number of contact points in the close packed model (weak repulsion)
Monomer	0	0
Dimer	1	1
Trimer	2	3
Tetramer	3	6
Pentamer	4	9
Hexamer	5	12
Octamer	7	18
Decamer	9	24

Scalability of results

The above analysis relies on a finite number of monomers (N_{init}) in order to calculate numerically the configuration with the highest entropy. For practical experiments this value is often uncertain or unknown. As a result it is crucial to demonstrate the independence of the observed distributions from the initial number of monomers. Equation 6.3 can be devided by N_{init} to express it in terms of molar fractions:

$$1 = \sum_{i=1}^{i_{max}} i x_i \tag{6.6}$$

The resultant expression is independent of N_{init} and hence can be applied to a system of any size. The second step of the proof involves the verification that the N of all monomers and agglomerates in solution (i.e., the sum of all monomers, dimers, etc.) and their distribution N_i is also independent of N_{init}. If a sufficiently large number of monomers is present in the solution, variables N and N_i can be treated as real numbers rather than integers. Each

microstate of a scalable system can then be expressed through a sequence of $i_{max} - 1$ coefficients c_i. The coefficients c_i represent the fraction of initial monomers that are bound in a certain agglomerate state. Consequently the distribution of the absolute numbers of agglomerates N_i can be expressed by:

$$N_i = c_i N_{init} i < i_{max} \tag{6.7}$$

and:

$$N_{i_{max}} = N_{init}(1 - \sum_{i=1}^{i_{max}-1} c_i) \tag{6.8}$$

The above expressions are all proportional to N_{init} and hence linearly scale with the number of initial monomers in the system. As a result, in accordance with Equation 6.2, N is also proportional to N_{init}. Having shown that N and N_i both linearly scale with N_{init}, we can conclude that the mole fractions $x_i = N_i/N$ of the agglomerates must be independent of N_{init} as well. Consequently the results of the simulation will be applicable to real systems.

Having demonstrated the scalability of the numerical results with respect to the entropy-only model we discuss the effect on the Gibbs energy of the system. The Gibbs energy per agglomerate is defined by dividing Equation 6.4 by N:

$$G' = \frac{G}{\sum_i N_i} = \sum_{i=1}^{i_{max}} x_i H_b n_i - k_B T \sum_{i=1}^{i_{max}} x_i \; ln(x_i) \tag{6.9}$$

As G' only depends on x_i and not on N_{init}, all distributions that are found via minimisation of G must be independent of N_{init} and therefore freely scalable.

6.1.3 Numerical simulation

Using the theory presented in the last section, numerical calculations were performed using a C++ code written by the author, compiled in Microsoft Visual Studio 2015. The full code is presented in the Appendix A. The programme systematically generates all possible configurations of cluster states and performs and exhaustive searches in a "generate and test" fashion. For example, initially the entropy of mixing is calculated in accordance with Equation 6.1 for a configuration, where all species are monomeric. Then the state where one dimer is present is considered and the rest of the species remain monomeric is considered, until all possible distributions are generated and the entropy of mixing of each individual distribution determined. Once all the configurations have been evaluated the one with maximum value of entropy of mixing is selected in the case of non-interacting particles.

For the non-ideal systems, the Gibbs energy of a given configuration is evaluated in accordance with Equations 6.4. The programme first evaluates entropy, S, (Equation 6.1) of a given configuration and then the enthalpy, H, in accordance with Equation 6.5. Once all the configurations have been evaluated the one with minimum of Gibbs energy is selected as the most probable distribution.

6.1.4 Results and discussion

Initially we considered the case of ideal non-interacting particles, followed by the discussion of repulsive and attractive interaction. Finally the entropy-only model was used to predict the distribution of agglomerates, using a

Gaussian distribution of the monomeric species as a starting point.

Entropy-only model

The C++ programme creates all possible state configurations and evaluates the entropy of a given configuration in accordance with Equation 6.1 and then determines the cluster distribution which corresponds to a maximum entropy of mixing. Initially the effect of the number of available agglomeration states was investigated and is shown in Figure 6.3, for the range of 2-10 monomers in a given cluster. It can be seen that as the number of available agglomeration states increases, the observed distribution converges to a unique overall distribution. In accordance with the entropy of mixing model, most agglomerates would not be comprised of more than 6 monomers. Higher agglomeration states will exist due to a large number of particles present in experimental systems, but would contribute little to the overall distribution. The number of available agglomeration states and the starting number of monomers in the system determines the computation times, required to determine the distribution with a maximum entropy of mixing. Table 6.2 provides the average simulation time for $N_{init} = 200$ and a range of available agglomeration states i_{max}. It can be seen that increasingly long times are required to evaluate the higher agglomeration states, with simulation times exceeding 750 minutes for agglomeration states $n_{max} > 11$. As a result for further simulations, the parameters used were $N_{init} = 200$ and $i_{max} = 10$.

The effect of the initial number of monomers (N_{init}) on the molar ratios of species was investigated numerically and is shown for the case where agglomerates up to tetramers are present, i.e., $i_{max} = 4$ in Figure 6.4. There

Table 6.2: Effect of the number of considered agglomeration states on the computation time for a starting population of 200 monomers.

i_{max}	Average computation time (min)
< 6	< 1
7	10
8	15
9	30
10	180
11	750

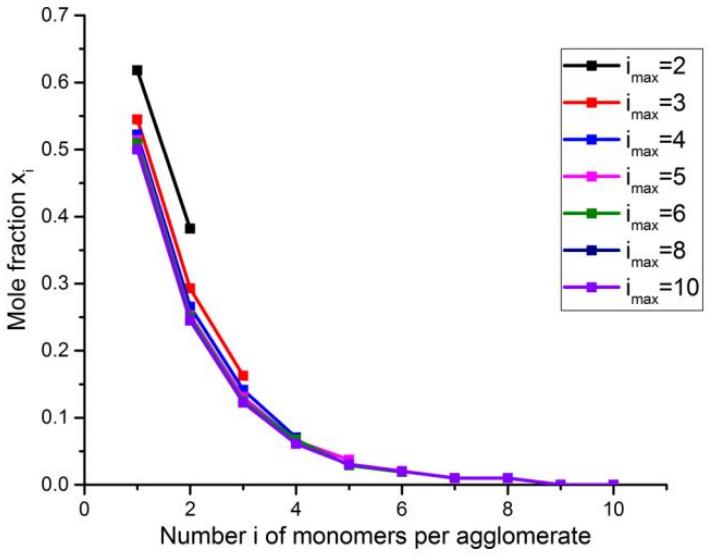

Figure 6.3: Effect of the number of available agglomeration states i_{max} on the resulting molar fractions of various types of agglomerates observed in the size distribution.

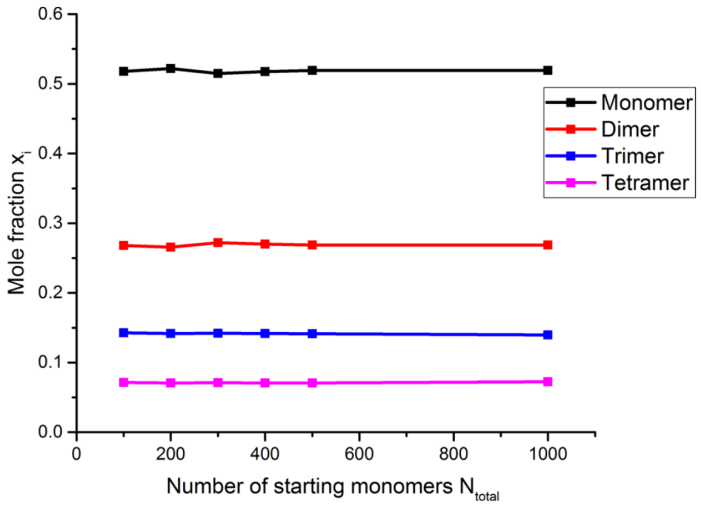

Figure 6.4: Effect of the total initial number of monomers N_{init} on the resulting mole fraction of species up to the tetramer state.

is no significant effect of N_{init} on the molar ratios of the species, the ratios of the agglomerates remain approximately constant, and the entropy of mixing scales with N_{init}. The slight variation is due to the discrete nature of the calculation. The total entropy of the system as a function of the highest agglomeration state is shown in Figure 6.5. With an increasing number of available states the total entropy increases before converging to a virtually constant value of 5.69 $J\ mol^{-1}\ K^{-1}$. As a result, if an experimentally observed distribution of particles deviates from the entropy of mixing-only model, this indicates the presence of energetically relevant interactions. Table 6.3 shows the mole fraction of each type of agglomerates in accordance with the maximisation of the entropy of mixing model and can be used to determine the entropic contribution for the experimental data and deviations due to inter-particle forces.

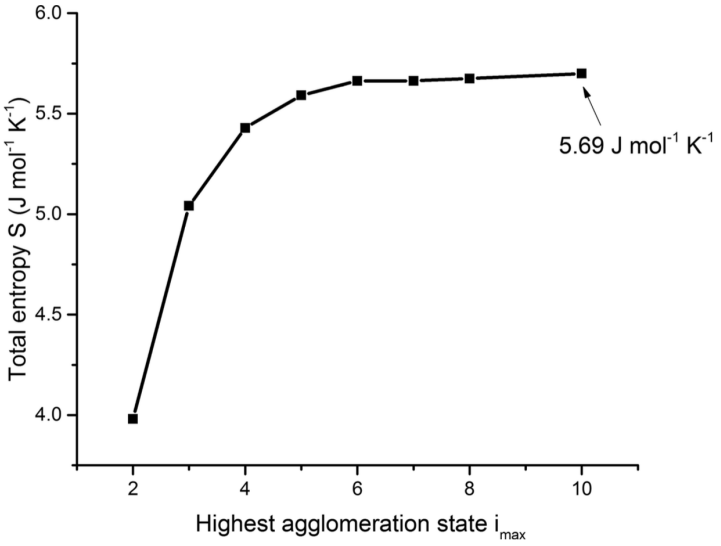

Figure 6.5: Dependency of the total entropy of mixing of the system on the number of available agglomeration states, calculated for various i_{max} and $N_{init} = 200$. The data are normalized to a mole of the initial monomer.

Table 6.3: Mole fractions of each type of agglomerate assuming an entropy of mixing-driven agglomeration process.

Number of monomers in agglomerate	Dimer	Trimer	Tetramer	Pentamer	Hexamer	Octamer	Decamer
1	0.618	0.545	0.522	0.514	0.510	0.500	0.500
2	0.382	0.293	0.265	0.252	0.250	0.245	0.245
3	x	0.163	0.142	0.131	0.125	0.122	0.122
4	x	x	0.071	0.065	0.067	0.061	0.061
5	x	x	x	0.037	0.029	0.031	0.031
6	x	x	x	x	0.019	0.020	0.020
7	x	x	x	x	x	0.010	0.010
8	x	x	x	x	x	0.010	0.010
9	x	x	x	x	x	x	0.000
10	x	x	x	x	x	x	0.000

Repulsive interactions

Nanoparticles often possess a charged coating in order to enhance the stability of the suspension as discussed in Section 2.2.4. Due to the charged coating, the particles repel each other, the agglomeration is energetically unfavourable and the solution is stable. Unlike the entropy-only case where we assume that all agglomerate states are equal in energy due to ideal behaviour of the particles, this assumption is no longer true for interacting particles. For repulsive interactions, higher agglomerate states will be higher in energy and the most probable equilibrium distribution will no longer have the highest entropy, but the system will instead adopt the state in which the Gibbs energy is minimized. The strength of interaction will be the determining factor for the observed agglomerate distribution. To investigate the effect of the strength of the interaction, different enthalpy values were evaluated in order to cover a range of potential interactions. In an entropy of mixing model the geometry of an agglomerate has no effect on the observed distribution of the clusters. By contrast for the cases where nanoparticle interaction takes place, the geometry and a number of contact points has significant impact on the particle size distributions. The determination of the number of contact points (n_i) is complicated as the observed behavior is strongly dependent on the strength of interparticle interaction. Particles experiencing strong attractive forces tend to form multiple contact points, which is energetically favourable and may result in closely packed structures if the change in enthalpy is large enough. By contrast, strongly repulsively interacting particles are less likely to form contact points due to the associated energetic costs

and the resulting structures are more chain-like. The present model assumes strongly bound capping agent and may lead to inaccuracies for cases where dynamic equilibrium exists between bound and unbound species. Table 6.1 shows the number of contact points for the two limiting cases of close-packed agglomerates and chain-like clusters.

We compared the effect of the geometry in the agglomeration model on the resultant distribution for the case of close-packed (see Figure 6.6a) and chain-like agglomeration (see Figure 6.6b). In the Figure 6.6a, it can be seen for the close-packed case with multiple contact points that, as the inter-particle interactions become stronger (higher repulsion), the resultant distribution of agglomerates tends to a monomeric distribution to minimize Gibbs energy. The chain-like agglomeration model has fewer contact points but a similar trend is observed in Figure 6.6, where we find that higher repulsion is required in order to observe identical population distributions as observed in the close-packing model. This prediction is consistent with experimental observations and the DLVO theory [154, 155], which demonstrates that highly negatively charged particles such as citrate-capped silver nanoparticles in a media of low ionic strength, form stable suspensions.

Attractive interactions

Having considered the case of repulsive interaction, the case of weakly attractive interaction is next considered. Experimentally this corresponds to uncoated particles, or suitably capped particles (for example citrate-capped silver nanoparticles or CTAB-capped gold nanoparticles) in strong ionic media. Attractive van der Waal forces exist between such particles and the

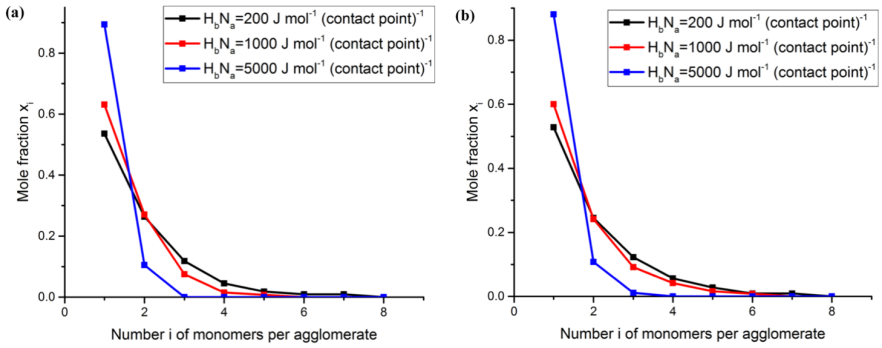

Figure 6.6: Agglomerate distributions obtained for the linear and close packed bonding models. (a) Impact of repulsive particle interactions on the distributions of agglomerate states for various enthalpies per contact point in the case of the close-packed agglomeration model. (b) Size distribution resulting from the chain-like agglomeration model for various contact point enthalpies in the case of repulsive interactions.

agglomeration process is likely to occur. As in the case of repulsive interaction the distribution of clusters will be affected by the magnitude of these interactions. The present model assigns fixed energy value per contact point, and as a result in the case of attractive interaction, agglomerates with the highest number of contact points would be energetically most favourable. Consequently the clusters are likely to be closely packed. Figure 6.7 shows the effect of the enthalpy per contact point for weakly attractive interaction of up to 120 $J\ mol^{-1}$. It can be seen that the resultant distribution is similar to the entropy of mixing case with only minor perturbations.

In the case of strong attraction the particles will tend to form large clusters. In order to provide an accurate distribution a very large number ($n \to \infty$) of agglomeration states will be required, as a result the present analysis is limited to weakly attractive particles with minimal perturbation to the entropy of mixing distribution.

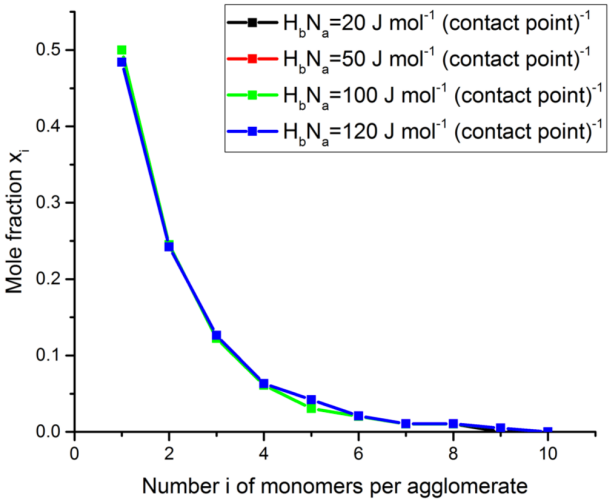

Figure 6.7: Effect of a weakly attractive contact point enthalpy on the agglomerate distribution.

Predicting size distribution of an agglomerated sample: Comparison with Gaussian and Log-Normal Distributions

The previous sections have described the molar fractions of agglomerates. In real experimental samples, Gaussian distributions of monomeric particles are common. In the present section using an arbitrary Gaussian monomeric sample with a mean particle size $\mu_{monomer}$ and the standard deviation $\sigma_{monomer}$ the resultant agglomerated size distribution is predicted. The overall distribution is a superposition of individual Gaussian distributions for each agglomerate:

$$\mu_{agglomerate} = i \times \mu_{monomer} \tag{6.10}$$

$$\sigma_{agglomerate} = \sqrt{i} \times \sigma_{monomer} \tag{6.11}$$

Table 6.4: Quality of the fits of Gaussian and log-normal distributions for the simulated agglomerate size distribution and a monomer size distribution featuring a standard deviation of $\sigma = 0.35 \cdot r_{monomer}$.

Fitted function	Reduced chi-square	Reduced r-square
Gaussian	7.1×10^{-9}	0.61
Log-normal	6.94×10^{-10}	0.94

where $\mu_{agglomerate}$ is the mean peak position of an agglomerate, i is the number of monomers in a given agglomerate, $\mu_{monomer}$ is the mean peak position of a monomer, $\sigma_{agglomerate}$ is the standard deviation of the agglomerate, and $\sigma_{monomer}$ is the standard deviation of the monomer. The integral of these superpositioned Gaussian distributions is proportional to the above-calculated respective molar fraction in the considered distribution and equals N. We can hence generate the expected agglomerate distribution starting from an arbitrary monomer with a mean radius of $\mu_{monomer}$ featuring a standard deviation $\sigma = 0.35 \times r_{monomer}$, where $r_{monomer}$ is the radius of a monomer. The generated resultant entropy of mixing distribution (blue line) is shown in Figure 6.8.

Experimentally it is common to fit either Gaussian or log-normal curves to the particle size distributions in order to describe the particle population. Least squares fitting (Levenberg-Marquardt method [166]) was used to fit such curves to an entropy of mixing distribution Table 6.4 shows the quality of fit for the two curves. A log-normal distribution exhibits the best agreement with the entropy of mixing model with the reduced χ^2 of 6.94×10^{-10} and reduced $r^2 = 0.94$ parameters in comparison to the Gaussian distribution. We hence speculate that this behaviour is general and may be the reason for

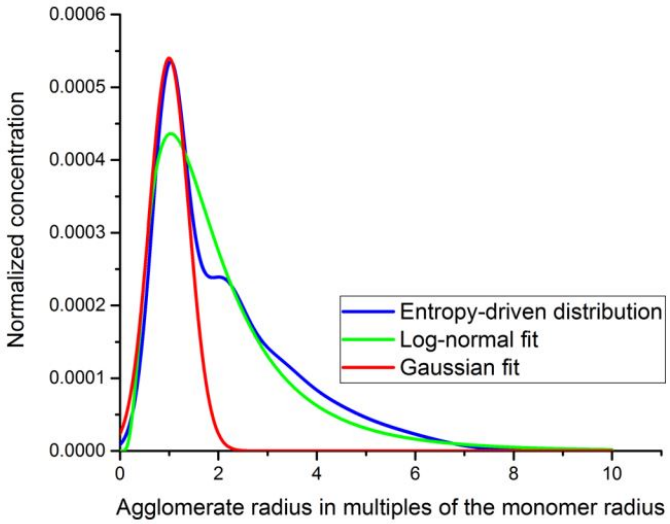

Figure 6.8: Fits to the distributions arising from an entropy-driven agglomeration process. The Levenberg-Marquardt method was used to fit Gaussian and log-normal distributions.

the fact that log-normal distributions are commonly observed in nature as a result of entropy-only processes. [163, 167, 168]

Comparing experimental data to the entropy of mixing model

In order to compare the proposed entropy-only model to a real-life system, we used data that was obtained via the nanoparticle tracking analysis of citrate-capped silver nanoparticles featuring a radius of approximately 100 nm. Using the procedure detailed in the experimental section, the distribution of the monomeric population (shown in Figure 6.9) was determined in distilled water, where the nanoparticles do not agglomerate and are known to be stable. [169] A Gaussian curve was fitted via least-squares algorithm (red line) with the following parameters: $\mu_{monomer} = 94\ nm$ and $\sigma_{monomer} = 54\ nm$ to characterize the monomeric population. Then a nanoparticle suspension con-

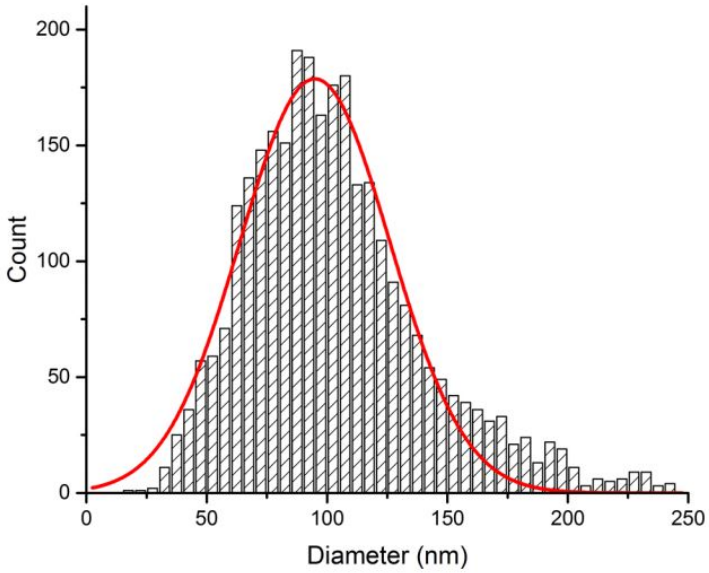

Figure 6.9: Size distribution of the monomeric sample in deionized water. The red line indicates a Gaussian fit.

taining 100 mM KCl electrolyte was prepared. High ionic strength facilitates agglomeration in accordance with the DLVO theory as discussed in Chapter 5. The agglomerated size distribution was measured using NTA and is shown in Figure 6.10. The distribution clearly shows the presence of large clusters, larger than the mean monomeric diameter of 94 nm. These parameters for the monomeric distribution ($\mu_{monomer} = 94\ nm$ and $\sigma_{monomer} = 54\ nm$) were used to calculate the size distributions of the agglomerated sample based on the entropy-only method and the approach detailed in the previous section. The only fitting parameter that was required to calculate the distribution of the agglomerate sample from the distribution of the monomer population was the concentration of the particles, represented by the overall area under the graph. An excellent agreement is observed between the predicted entropy of mixing model and the experimentally observed distributions. The devia-

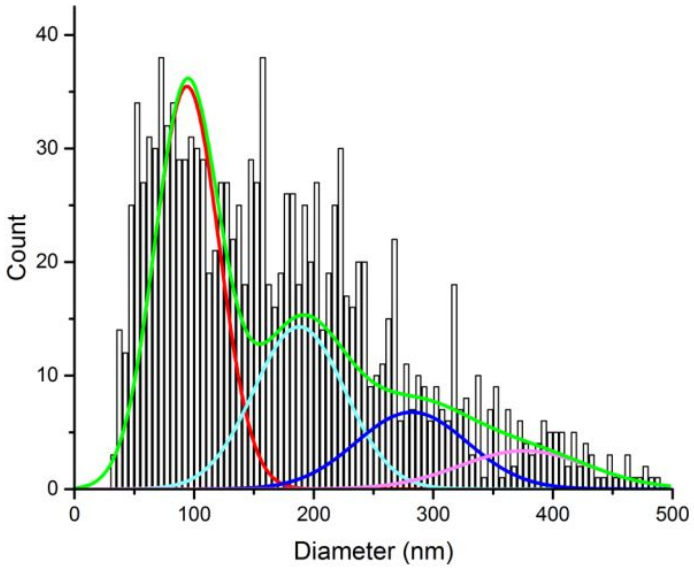

Figure 6.10: Size distribution of the agglomerated sample, obtained via NTA measurements. The green graph presents the distribution predicted via the maximization of the system's entropy. All the other graphs represent the contributions of the individual agglomeration states to the overall distribution (monomer, dimer, trimer e.t.c).

tions may be explained by variability of the repulsive coating on individual particles and hence variable stability, leading to an existence of inter-particle interaction.

6.1.5 Conclusions

We demonstrate that entropy of mixing may play a fundamental role in the agglomeration of nanoparticles. Using classical concepts from thermodynamics and statistical mechanics, we understand the agglomeration process of weakly interacting nanoparticles and validate our theory through an experimental system comprising citrate-capped silver nanoparticles, which shows excellent agreement with our simplistic entropy-only model. The analysis is

applicable to a variety of particle systems, as it does not require the knowledge of inter-particle interaction strength. It enables the prediction of agglomerate size distributions, even if the agglomeration process is perturbed by energetically relevant interactions between monomers in an agglomerate. It can be noted that the entropy of mixing contribution to the nanoparticle agglomeration process is always present in such systems and the distribution of monomers, dimers, trimers, etc. identified above provides an essential starting point for the understanding of other possible contributions to the thermodynamics. In addition to that, the maximum entropy of mixing approach allows the interpretation of experimentally frequently encountered log-normal distributions, which appear to be a direct consequence of entropy of mixing processes at play.

The present numerical analysis is constrained by the long computation times and in the next section, an analytical approach to the problem is discussed and an exact solution is provided for the entropy of mixing distribution for a system containing infinite possible agglomeration states.

6.2 Analytical Solution to the Maximization of Entropy Problem

In the last section numerical approach to the maximization of entropy of mixing problem was discussed. The resulting distributions were computationally found via exhaustive searches in a “generate and test” fashion, which prohibited the consideration of a larger number of possible agglomeration states

due to constraints in computational capacity and exceedingly long simulation times as shown in Table 6.2. Despite the limitations, excellent agreement was observed between the experimental results for the citrate-capped silver nanoparticles and the theoretical predictions. In the present section an analytical solution will be provided for a system with an infinite number of agglomeration states. This analytical solution was derived by Dr. Enno Kätelhön (University of Oxford, Department of Chemistry) using a numerical multi-dimensional Newton-Raphson method to form an initial 'guess' for the analytical form. According to this solution, a thermodynamic equilibrated system of particles will adopt an agglomerate distribution equal to a geometric progression with a common ratio of $\frac{1}{2}$, provided that there is negligible enthalpy contribution.

6.2.1 Experimental

Nanoparticle tracking analysis (NTA) was employed to measure the size distribution of individual citrate-capped Ag nanoparticles as well as the size distributions of agglomerates of the same particle population as well as of a system of uncapped Bi_2O_3 nanoparticles. To this end, citrate-capped silver nanoparticles were sized in deionized water in order to obtain a monomeric particle size distribution. The particles were then transferred into 0.10 M potassium chloride, which facilitates agglomeration by minimising electrostatic forces between adjacent particles as predicted by DLVO theory, and the distribution of now agglomerating particles was measured. In addition to that, we analogously measured the distribution of agglomerating Bi_2O_3

nanoparticles in the presence of 0.10 M sodium hydroxide. The Brownian motion of the particles was recorded for a period of 60 s at a temperature of at $25.00 \pm 0.05°C$ using manual gain and shutter settings. Raw tracking data were obtained and analysed through the NTA 2.3 software environment, which was used to construct the resultant size distributions. Measurements were repeated three times, while each time a different area of the sample was chosen to achieve a representative view of the sample and to confirm the stability of the distribution on the time scale of the experiments. Monomeric distributions of the Bi_2O_3 nanoparticles were gained by nano-impacts as discussed in Chapter 5.

6.2.2 Theory

The maximization of entropy variation problem is defined in accordance with the Equation 6.1. This equation can be re-expressed in terms of the molar fraction as:

$$max(S = -k_B \sum_{i=1}^{i_{max}} N_i ln(\frac{N_i}{\sum_{j=1}^{j_{max}} N_j})) \tag{6.12}$$

Note that the change of index variable is performed in accordance with $i_{max} = j_{max}$ subject to a constraint that the total number of monomeric units remains constant:

$$g(N_1, ..., N_{i_{max}}) = N_{init} - \sum_{i=1}^{i_{max}} iN_i = 0 \tag{6.13}$$

This optimisation problem can be transformed into a system of $i_{max}+1$ equations via the method of Lagrange multipliers, [170] maximising the function $g(N_1, ..., N_{i_{max}})$ subject to the constraint $g(N_1, ..., N_{i_{max}}) = 0$. To this end, we construct the corresponding Lagrange function from Equations 6.12 and

6.13 as follows:

$$\begin{aligned} L &= S(N_1, ..., N_{i_{max}}) + \lambda g(N_1, ..., N_{i_{max}}) \\ &= -k_B \sum_{i=1}^{i_{max}} N_i ln(\frac{N_i}{\sum_{j=1}^{j_{max}} N_j}) + \lambda(N_{init} - \sum_{i=1}^{i_{max}} iN_i) \end{aligned} \tag{6.14}$$

where λ is a real number known as the Lagrange multiplier. [171] The partial derivatives of the Lagrange function with respect N_i are calculated as:

$$\frac{\partial}{\partial N_i} = \lambda i - k_B ln(\frac{N_i}{\sum_{i=1}^{i_{max}} iN_i}) \tag{6.15}$$

Following the Lagrange formalism, the maximum value of S, that is, the ensembles' state featuring the maximum entropy, can be found by solving the following system of $i_{max} + 1$ equations with respect to N_i and λ:

$$\begin{aligned} &\frac{\partial}{\partial N_i} L = 0 \; with \; i \in [1, i_{max}] \\ &\frac{\partial}{\partial \lambda} L = g(N_1, ..., N_{i_{max}}) = 0 \end{aligned} \tag{6.16}$$

The resultant system of equations can be solved numerically via a multidimensional Newton-Raphson solver after conversion of the system equations to the appropriate form. For the solver to operate the system of equations must be of the form:

$$f_i(N_1, ..., N_{i_{max}}, \lambda) = 0 \tag{6.17}$$

Function, f, is such that $\mathbb{R}^{i_{max}+1} \rightarrow \mathbb{R}^{i_{max}+1}$. Exponential functions and the Boltzmann constant, k_B and can be substituted, in order to simplify the

numerical calculations by:

$$\phi = exp(\frac{\lambda}{K_B}) \in \mathbb{R}^+ \tag{6.18}$$

Consequently the system of Equation 6.16 is expressed as:

$$0 = f_i = \begin{cases} N_{init} - \sum_{k=1}^{k_{max}} iN_j \ for \ i = 0 \\ \frac{N_i}{\sum_{k=1}^{k_{max}}} - \phi^i \ for \ i \in [1, i_{max}] \end{cases} \tag{6.19}$$

The Newton-Raphson [172] solver is an iterative method and involves accuracy refinement, starting with an initial guess for all N_i and λ. The exact value is approached after n_{max} iterations. Effectively a system of equations is solved at each iteration n:

$$J_{i,j} \times \Delta N_j^n = f_i(N_i^n) \tag{6.20}$$

After each iterations the values N_i are updated:

$$N_i^{n+1} = N_i^n - \Delta N_i^n \tag{6.21}$$

$J_{i,j}$ is known as the Jacobian matrix of the function, f and is given by:

$$J = \begin{bmatrix} J_{0,0} & \dots & J_{0,j_{max}} \\ \vdots & J_{i,j} & \dots \\ J_{i_{max},0} & \dots & J_{i_{max},j_{max}} \end{bmatrix} = \begin{bmatrix} \partial_\lambda f_0 & \partial_{N_1} f_0 & \dots & \partial_{N_{i_{max}}} f_0 \\ \vdots & \vdots & \vdots & \vdots \\ \partial_\lambda f_{i_{max}} & \partial_{N_1} f_{i_{max}} & \dots & \partial_{N_{i_{max}}} f_{i_{max}} \end{bmatrix} \tag{6.22}$$

Table 6.5: Parameters used in the Newton-Raphson solver, when determining the distribution of agglomeration states for the case that agglomerates comprising up to 40 monomers may be present

Parameter	Description	Value
n_{max}	Number of iterations	1000
ϕ^0	Initial guess for ϕ^0	0.2
N_i	Initial guess for N_i	0.01

Using the system of Equations 6.19 the elements of J are calculated to be:

$$J_{i,j} = \partial_{N_i} f_i = \begin{cases} -j & \text{for} \quad i = 0,\ j \in [0, j_{max}] \\ -i\phi^{i-1} & \text{for} \quad i \in [1, i_{max},], j = 0 \\ -\frac{N_i}{\sum_{k=1}^{k_{max}} N_k)^2} & \text{for} \quad i, j \in [1, j_{max}], i \neq j \\ \frac{1}{\sum_{k=1}^{k_{max}} N_k} - \frac{N_i}{(\sum_{k=1}^{k_{max}} N_k)^2} & \text{for} \quad i, j \in [1, j_{max}], i = j \end{cases} \tag{6.23}$$

The numerical solver evaluates the distribution of N_i, that is defined through the system of equations (System of equations 6.19) generated within the Newton-Raphson method. During each iteration, the corrections to N_i, ΔN_j^n, are determined via the tridiagonal matrix decomposition of the Jacobian, J, and subsequent Gaussian elimination. Since the diagonal matrix element, $J_{0,0}$, however always equals zero, the two first rows of the system are swapped in order to avoid division through zero in the tridiagonal matrix decomposition. Custom C++ code was written to perform the above described operations and run on a standard personal computer. The simulation parameters are summarised in Table 6.5.

6.2.3 Results and discussion

The Newton-Raphson numerical calculations have yielded the values of N_i virtually identical to the geometric progression:

$$N_i = \frac{1}{2^{i+1}} \tag{6.24}$$

The closed form of the geometric series has the following properties:

$$a_0 \sum_{1=0}^{\infty} q^i = \frac{a_0}{1-q} \; for \; |q| < 1 \tag{6.25}$$

with $a_0 = 14$ and $q = 12$ and the identity the expression becomes:

$$\sum_{1=0}^{\infty} q^i = \frac{i}{2^i} = 2 \tag{6.26}$$

This analytical solution can be verified by the substitution of Equation 6.24 into the system of Equations 6.16, which reveals that it is indeed the true solution.

For comparison with the experimental data, the distribution of agglomerates can be expressed in terms of mole fractions x_i:

$$x_i = \frac{1}{2^i} \tag{6.27}$$

The derived analytical solution has been compared to the results of the Newton-Raphson calculation, discussed in the previous section and the previously reported results [152] are shown in Figure 6.11. Excellent agreement is observed between the different approaches. The deviations between the

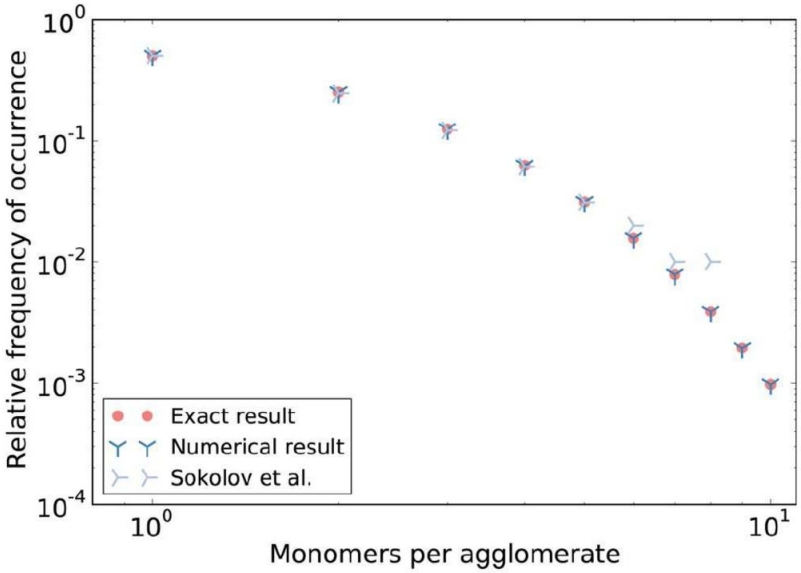

Figure 6.11: Normalised distributions of agglomerates found in the case of maximum entropy of mixing. Comparison between the exact, the numerical,and the previous result [152] for agglomerate comprising up to ten monomers. Please note that only ten agglomeration states are depicted in the figure and different approaches consider different maximum numbers of monomers per agglomerate.

present method and previous literature reports can be explained by the numerical discretization approximations used.

6.2.4 Comparing the model with experimental data

The theoretical model was compared to the two experimental systems: suspensions of Bi_2O_3 NPs and citrate-capped silver nanoparticles. Our model estimates an upper limit in terms of agglomerate radii in the size distribution on the basis of the monomers size distribution and Equation 6.27 via means of Gaussian progression of uncertainty, while a lower limit representing a close packaging of monomers in an agglomerate will yield a distribution

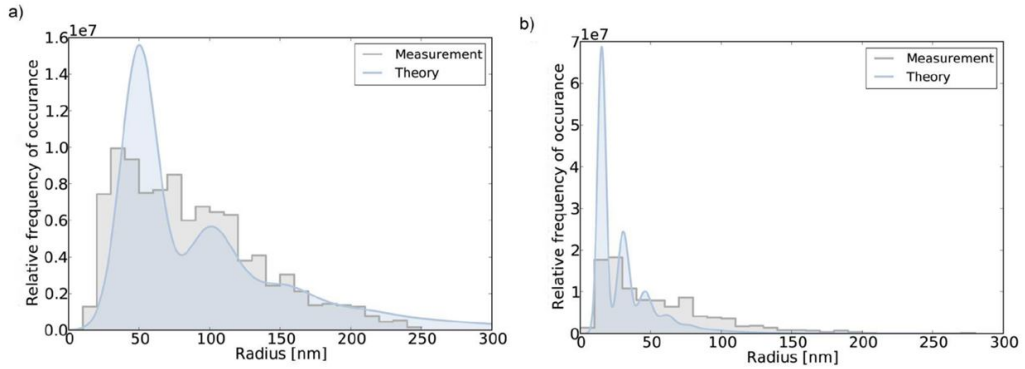

Figure 6.12: Comparison between the measured size distribution of agglomerating nanoparticle systems and corresponding theoretical preditions. a) NTA measurements of citrate-capped silver nanoparticles and b) NTAdata[5]of bismuth (III) oxide nanoparticles. In the presentation of the experimental data, multiple bins are combined to a bin width of 10 nm for a clearer presentation. The depicted theoretical model considers agglomerates states comprising up to a hundred monomers

more similar to the size distribution of monomers. Mathematically this can be expressed as a normalised, weighted distribution by a frequency of occurrence:

$$d(x) = \frac{1}{K} \sum_i \frac{f(x, u_{agglomerate}, \sigma_{agglomerate})}{2^i} \tag{6.28}$$

where

$$K = \int_0^\infty dx \sum_i \frac{f(x, \mu_{agglomerate}, \sigma_{agglomerate})}{2^i} \tag{6.29}$$

and

$$f(x, \mu, \sigma) = \frac{1}{\sigma\sqrt{2\pi}} exp(-\frac{(x-\mu)^2}{2\sigma^2}) \tag{6.30}$$

where $\mu_{agglomerate}$ and $\sigma_{agglomerate}$ are defined in accordance with Equations 6.10-6.11 respectively. The monomeric particle size distributions and the least-squares fitting of Gaussian curves for citrate-capped and bismuth oxide nanoparticles are shown in Figure 6.13. The mean values ($\mu_{monomer}$) of the

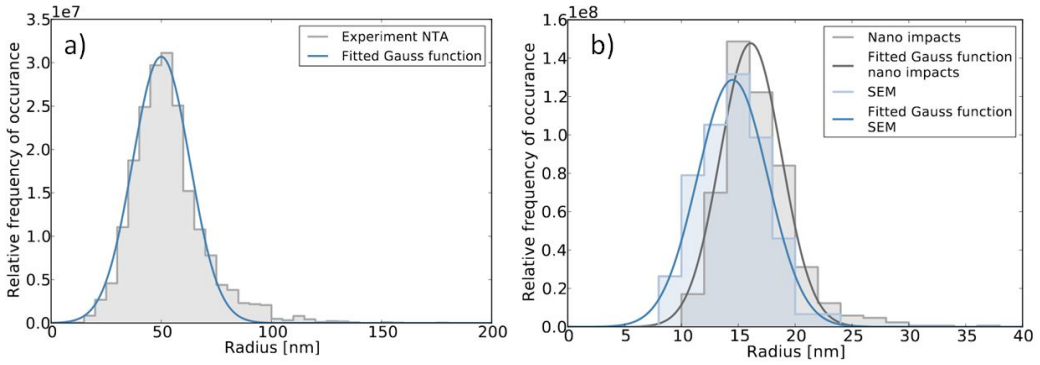

Figure 6.13: Measured size distribution of monomers in two different nanoparticle systems and corresponding Guassian fits, obtained via least-squares fitting. a) NTA data of citrate-capped Ag nanoparticles and b) Nano impacts and SEM data of Bi_2O_3 nanoparticles.

monomer radii and the related standard deviation ($\sigma_{monomer}$) were found to be 50.0 nm and 13.0 nm respectively, in the case of Ag nanoparticles (Figure 6.13a). For bismuth oxide a slight discrepancy was observed between the SEM microscopy size distribution and electrode-particle impacts method as discussed in the previous section, consequently an average of the two fits was used ($\mu_{monomer} = 15.3\ nm$ and $\sigma_{monomer} = 2.9\ nm$)

Figure 6.12 compares the predicted entropy of mixing distributions with the NTA data for both experimental systems. The measurements resemble the theoretically predicted distribution of agglomerate states. Silver nanoparticles show a good agreement with the theoretical prediction. On the other hand the bismuth oxide experiment shows deviations of the theoretical predictions, from the experimentally observed behaviour. Firstly, the distribution of Bi_2O_3 agglomerates tends towards larger clusters than expected and, secondly, the theoretical model shows clear presence of sharp multiple peaks for individual agglomeration states and experimental distribution is broader

and 'smoother'.

The deviations could be potentially accounted for, if we consider *reversible* agglomeration. [82] When a particle is tracked by NTA it can transition between monomeric and clustered state on the timescale of the measurement. Depending on the frequency of such transitions NTA tracking software may yield a diffusion coefficient of a particle which is an average of the intermediate states weighted by the duration. An additional complication is that agglomerates may also change shape during the clustering/de-clustering processes. The close packed agglomerate will have a markedly different diffusion coefficient to the chain-like structure and consequently the overall size distribution may be affected. Modelling such dynamic effects is inherently complex and is beyond the capabilities of the present entropy of mixing model.

6.2.5 Conclusions

Analytical solutions presented herein allows modelling agglomerating systems with an infinite number of agglomeration states. This result allows us to avoid complex numerical modelling and allows a fast comparison with experimental data. The use of the entropy of mixing model generally yields a good agreement with the experimental data and can be used to indicate deviations due to inter-particle interactions and/or instrumental artefacts.

Chapter 7

Near-wall Hindered Diffusion in Convective Systems: Transport Limitations in Colloidal and Nanoparticulate Systems

So far in this thesis, the inter-particle forces have been investigated and the effect of the reversible agglomeration on the size distributions studied via an electrode-particle impact method. In this chapter the convective-diffusional behaviour of nanoparticles is investigated using a finite difference numerical approach in the context of redox-flow cells. The effect of the near-wall hindered diffusion is investigated for a well-defined convective system. In particular, the rotating disk electrode is used as a model due to wide applicability of the technique for the battery testing and a well defined laminar flow, amicable to the theoretical modelling. A major influence of the near-

wall hindered diffusion is observed in the resulting concentration profiles of the nanoparticles (aqueous concentration as a function of distance from the electrode) and the current responses in the case of the colloidal suspensions. This finding is likely to have a significant impact on the understanding of physical processes underlying nanoparticulate systems which involve convective contributions. The work highlights that the theoretical assumptions commonly used for molecular species require re-evaluation in the case of colloidal suspensions and may be a source of error. The findings have been published in *Journal of Physical Chemistry C*. [173]

7.1 Introduction

The increased usage of renewable energy sources requires means for efficient, scalable and low cost storage of the generated energy. A wide range of potential solutions have been developed over the years from compressed air approaches to the state of the art superconducting magnetic energy storage. [174] Electrochemical methods may provide an attractive option due to their relative simplicity, potential scalability and low cost. [174–176] Redox flow batteries have been the subject of intense research due to the decoupled power/energy storage design. To date the main limitation of traditional redox flow systems is poor energy density due to low ion concentrations and limited operating cell-voltages. [177] A novel approach involves use of a colloidal suspension of electroactive nanoparticles as a "nanoelectrofuel" where the charge and discharge rates are enhanced due to the presence of nanoparticles, while the resultant increase in viscosity is negligible. [178, 179] Efficient practical

applications and further improvements in the efficiency require understanding of the physical processes which arise in such colloidal nanoparticulate systems. To date the Colloidal Filtration Theory (CFT), originally developed by *Yao et. al* [180], has been the main approach to modelling convective-diffusive systems. The CFT takes into account interactions of the molecular and solute nature in accordance with the DLVO theory [154, 155] and also considers the near-wall hydrodynamic effects. The CFT has been successfully applied to diverse systems ranging from colloidal suspensions [181] to movement of bacteria in a contaminated sandy aquifer. [182] Modern refinements of the CFT theory provide a superior treatment of the hydrodynamic effects and consequently demonstrate a high degree of accuracy. [157, 183–185] These models feature high degrees of complexity and in many cases require time-consuming numerical simulations. The aim of the present chapter is to provide a treatment of a convectional-diffusional system from an electrochemical point of view with the main aim of predicting the current response rather than the collector properties.

In Section 1.6.2 the design and theory of the rotating disk electrode (RDE) was discussed. The RDE has proved to be an invaluable tool [25, 186] for the study of electrochemical processes as evidenced by the large body of literature. The RDE technique has been successfully used to elucidate reaction mechanisms [187] and has found a wide variety of industrial applications (in particular battery testing) [188–190]. Recently the RDE was successfully applied to characterize the electrochemical behaviour of colloidal suspension of nanoparticles. [191–193] Advantages of the rotating disk are: the bulk solution is well-mixed and homogeneous, the rotation rate allows control of the

mass transport to the electrode surface, and most importantly the steady state current response allows accurate analysis of the systems and extraction of kinetic parameters. In addition the RDE electrode involves an electrode of macro-dimensions and the resulting high current signal does not require the setup to be shielded by a Faraday cage, unlike microelectrodes which often suffer from interferences due to the low current signal. [27]

In the next section, the hydrodynamics of the rotating disk electrode will be discussed. The concept of near-wall hindered diffusion will be introduced and applied in the context of an impacting nanoparticle. Butler-Volmer kinetics theory will be extended to account for the distributed electron tunnelling. Finally the current response will be predicted for a range of particle sizes at different rotation frequencies.

7.2 Theory

Initially we consider mass transport to the rotating disk electrode. In the derivation of the current expression at the rotating disk electrode, as shown in Section 1.6.2, Levich assumed an anisotropic diffusion coefficient. As a result the diffusion coefficient is independent of the distance from the electrode surface, x, an assumption which is usually exact for molecular species, but can potentially introduce inaccuracy in the case of nanoparticles, which are larger in size. [18, 194, 195] It has been demonstrated by Brenner [196] that a moving particle near a wall experiences a hindrance due to a hydrodynamic force. The effect is known as near-wall hindered diffusion and is significant for colloidal systems as demonstrated with a wide range of exper-

imental techniques [194, 195, 197–199]. The effect manifests itself in the apparent reduction of the diffusion coefficient within close proximity of the solid boundary. As a result a distance dependent correction factor, λ, is required for the diffusion coefficient. This correction factor will be discussed in the next section. In the present work we extend Levich's analysis of the rotating disk to a colloidal system. We consider a system of electroactive particles and solve the diffusion-convection equation for species of various sizes accounting for the near-wall hindrance term. For the solution of the mass transport to a rotating disk we use the analysis developed by Elimelech. [200] The mass transport problem and the corresponding convection-diffusion equation can be formulated mathematically by:

$$\frac{\partial c}{\partial t} = \frac{\partial}{\partial x'}(\lambda(x')D\frac{\partial c}{\partial x'}) - v_{x'}\frac{\partial c}{\partial x'} = 0 \tag{7.1}$$

$$x' = x - r \tag{7.2}$$

where c is the concentration of electroactive species, x' is the separation between the nanoparticle edge and the electrode, x is the normal distance between the particle's centre and the electrode surface, and r is the radius of a particle. In order to facilitate ease of analysis and reduce complexity of the analysis the Equation 7.1 is solved under steady-state condition.

7.2.1 Near-wall hindered diffusion

As a particle approaches a solid boundary it experiences reduced mobility and as a result the diffusion coefficient is no longer uniform and a correction

factor is needed. The detailed analysis has been provided by Brenner [196] and the solution was given in terms of an infinite series. An approximation was introduced by Bevan and Prieve [201] in order to facilitate ease of use and this expression has been used in the present work as shown in Equation 7.3:

$$\lambda = \frac{6x'^2 + 2rx'}{6x'^2 + 9rx' + 2r^2} \tag{7.3}$$

The resultant diffusion coefficients of the particles will depend on their position with respect to a boundary:

$$D_{x'} = D_{bulk}\lambda(x') \tag{7.4}$$

where D_x is the diffusion coefficient at a given distance from the electrode, and D_{bulk} is the bulk diffusion coefficient. For a RDE system which involves a planar electrode the most important parameter is the electrode/particle separation. As a result, unlike the case described by *Eral et al.*, [184] the angular component will be insignificant as it will not have an effect on the observed current response and the main contribution will be the normal component (x) of the diffusion.

Justification of applicability of near-wall hindered diffusion

The derivation obtained by Brenner [196] is only strictly valid for an unperturbed system and hence its application to the RDE requires justification. According to the solution for the velocities provided by Von Karman [34] and Cochrane [35] at the surface the azimuthal component is equal to unity, and both axial and radial components decay to zero. As a result, provided that

the flow to the disk is laminar a virtually stagnant layer is observed, which allows us to make use of the Brenner analysis. At very fast rotation rates (high Reynolds numbers, $Re = \frac{\omega r^2}{v} > 2000$) the flow will become turbulent and as a result the treatment presented in the present work would no longer be applicable. A particle in the solution with effective mass m^* (defined in accordance with Equation 7.5) will also experience a centrifugal force at the close proximity of the electrode. Consequently the radial velocity of the particle needs to be considered. The radial velocity of a particle v_{np} is given by Equation 7.6.

$$m^* = \frac{4}{3}\pi r_{np}^3(\rho_{np} - \rho_{solvent}) \tag{7.5}$$

$$v_{np} = \frac{m^*\omega^2 r}{6\pi\mu r_{np}} \tag{7.6}$$

where m^* is the effective mass, ρ is the respective densities of a particle and a solvent, v_{np} is the radial velocity of the particle, μ is the dynamic viscosity. The resultant radial velocity even for large nanoparticles, where $r \approx 50\ nm$, is small and does not lead to significant perturbations and as a result the near-wall hindered diffusion remains applicable as the dominant mass transport. Note also for such small particles their radius is tiny compared to the thickness of the hydrodynamic layer so that the mass transport enhancement seen for much larger particles is not significant. [202–205]

Due to the near-wall hindered diffusion, the diffusion coefficient at the electrode surface is zero. This leads to an apparent zero mass flux (f) for the simulation if the traditional flux [2, 206–208] measurement of the concentra-

tion gradient at the electrode surface is taken:

$$f = D_{x=0} \frac{dc}{dx}\bigg|_{x=0} = 0 \tag{7.7}$$

On the other hand if the electrical flux is measured at a small distance from the electrode where the diffusion coefficient is not zero, the electrical flux will change with the spatial variation of the diffusion coefficient. As a result an alternative approach is warranted in order to simulate the actual electrical flux of the species.

In reality the electron transfer takes within a zone close to the electrode surface where electron tunnelling is possible [22, 209] and as a result a more complex boundary condition is warranted for the solution of convection diffusion equation, which will be discussed in the further sections.

7.2.2 Electron tunnelling

In order to measure the simulated electrical flux and avoid the problems highlighted in the previous section, it is possible to incorporate electron tunnelling which is confined to a certain volume in close proximity to the electrode surface. [22, 209–211] Electron tunnelling is a distance dependent problem and its probability, P, is thought to fall off approximately exponentially with increasing distance in accordance with Equation 7.8:

$$P = ve^{-\beta x} \tag{7.8}$$

where v is a frequency factor (s^{-1}), and β is the electron-tunnelling decay factor (m^{-1}) which is dependent on the medium where the electron transfer takes place and for aqueous solvent is equal to 1.59 $\mathring{A}^{-1}$. [2, 212, 213]

7.2.3 Butler-Volmer Kinetics

The rate of electron transfer can be modelled at every point in the solution in accordance with the Butler-Volmer kinetic equation, [1,2] which describes the rate of electron transfer dependence on the potential applied. For a single electron transfer reaction, for a redox couple where both A and B have the same diffusion coefficients the Butler-Volmer concentration dependence is defined in accordance with Equation 7.12.

$$B \rightleftharpoons A + e^- \tag{7.9}$$

$$D_A = D_B \tag{7.10}$$

$$[B] = [A]_{bulk} - [A] \tag{7.11}$$

$$f_{BV} = ([A](x)e^{-\alpha\eta} + ([A](x) - [A]_{bulk})e^{(1-\alpha)\eta}) \tag{7.12}$$

$$\eta = \frac{F}{RT}(E - E_f^0) \tag{7.13}$$

where $[j]_a$ is the bulk concentration, $[j]$ is the concentration of a given species, α is the charge transfer coefficient (for many reactions $\alpha \approx 0.5$) [16, 17], k_0 is the standard electrochemical rate constant and η is the dimensionless potential with respect to the formal potential, E_f, for a given species couple, F is the Faraday constant, R is the gas constant and T is the temperature.

Table 7.1: Dimensionless parameters used for the simulation

Dimensional Parameter	Dimensionless Form
Velocity constant L	$L = (0.5102313(2\pi f)^{3/2}\upsilon^{-1/2}$
Time t	$T = (L^2 D_{bulk})^{1/3} t$
Space x	$W = (\frac{L}{D_{bulk}})^{1/3} x$
Concentration c	$C = \frac{c}{c_{bulk}}$
Tunnelling Constant β	$\beta^* = (\frac{L}{D_{bulk}})^{-1/3}\beta$
Radius of a particle r	$R = (\frac{L}{D_{bulk}})^{1/3} r$
Frequency factor v	$v^* = (\frac{L}{D_{bulk}})^{1/3} v$
Standard electrochemical rate constant k_0	$K = \frac{(\frac{L}{D_{bulk}})^{-1/3} k_0}{D_{bulk}}$
Butler-Volmer f_{bv}	$F_{BV} = (Ce^{-\alpha\eta} + (C-1))e^{(1-\alpha)\eta}$

In the absence of tunnelling the electrical flux is given in accordance with the ideal Butler-Volmer equation:

$$f = k_0 f_{BV}|_{x=0} \tag{7.14}$$

Dimensionless Parameters

The use of dimensionless parameters allows us to simplify the convection-diffusion equations. Conventional dimensionless parameters [25, 208] were chosen in order to combine the angular velocity and the diffusion coefficient of the particles. Equations (ODEs) were converted to a dimensionless form using the parameters described in Table 7.1. The relationship between di-

Table 7.2: Conversion between dimensional and dimensionless parameters

	Dimensional Value	Dimensionless Value at 10 Hz		Dimensionless Value at 50 Hz	
Parameter		$r_{np} = 1\ nm$	$r_{np} = 50\ nm$	$r_{np} = 1\ nm$	$r_{np} = 50\ nm$
β	$1.57 \times 10^{10} m^{-1}$	1.6×10^5	0.45×10^5	0.7×10^5	0.19×10^5
v	$0.001 - 1\ s^{-1}$	$6.3 \times 10^6 - 2.3 \times 10^7$	$6.3 \times 10^9 - 2.3 \times 10^{10}$	$1.2 \times 10^6 - 4.6 \times 10^6$	$6.3 \times 10^9 - 2.3 \times 10^{10}$
$E - E_f$	0.25 to -0.38 V	10 to -15	10 to -15	10 to -15	10 to -15

mensional and dimensionless values used in the simulations is given in Table 7.2 for two sizes of particles; $r = 1\ nm$ and $r = 50\ nm$ and the two rotations frequencies of 10 Hz and 50 Hz.

Extension of Butler-Volmer Kinetics applied to the RDE

Levich solved the convection-diffusion equation (Equation 1.44) under the conditions of infinite kinetics (in accordance with the boundary condition $c_{x=0,t} = 0$). It is possible to extend the solution by assuming that the surface concentration of species is controlled by Butler-Volmer kinetics and altering the boundary condition. Hence the following equation must be solved:

$$D\frac{d^2c}{dx^2} - v_x\frac{dc}{dx} = 0 \tag{7.15}$$

subject to the boundary conditions at the electrode surface and in the bulk:

$$D\frac{dc}{dx}\bigg|_{x=0} = k_0 f_{BV} \ \ and \ \ c_{x=\infty} = c_{bulk} \tag{7.16}$$

The analytical solution for the concentration profile with the finite Butler-Volmer kinetics was obtained using Mathematica Software (Wolfram Research, Inc., Mathematica, Version 10.3, Champaign, IL (2016).) and is

given in accordance with Equation 7.17 in dimensionless form:

$$C(W) = \frac{3e^{\alpha\eta} + \sqrt[3]{3}K\Gamma\left(\frac{1}{3}\right)e^{\alpha\eta} - \sqrt[3]{3}K\gamma\left(\frac{1}{3}, \frac{W^3}{3}\right) + \sqrt[3]{3}K\Gamma\left(\frac{1}{3}\right)}{3e^{\alpha\eta} + \sqrt[3]{3}K\Gamma\left(\frac{1}{3}\right)e^{\alpha\eta} + \sqrt[3]{3}K\Gamma\left(\frac{1}{3}\right)} \tag{7.17}$$

where K is the dimensionless heterogeneous rate constant. At high negative potentials the expression becomes equivalent to the Levich concentration profile which is consistent with the assumptions of zero concentration at the electrode surface used by Levich, while at high positive potentials the concentration is uniform as no depletion of the reactants takes place.

$$\lim_{\eta\to-\infty} C(W) \to 1 - \frac{\gamma\left(\frac{1}{3}, \frac{W^3}{3}\right)}{\Gamma\left(\frac{1}{3}\right)} \tag{7.18}$$

$$\lim_{\eta\to\infty} C(W) \to 1 \tag{7.19}$$

By evaluating the derivative of Equation 7.17 at the electrode surface the electrical flux response can be evaluated in accordance with Equation 7.20.

$$F = \frac{3K}{3e^{\alpha\eta} + \sqrt[3]{3}K\Gamma\left(\frac{1}{3}\right)e^{2\alpha\eta} + \sqrt[3]{3}K\Gamma\left(\frac{1}{3}\right)} \tag{7.20}$$

where F is the dimensionless electrical flux. This equation can be used to predict the flux at an RDE within the framework of the Butler-Volmer theory.

7.2.4 Combining tunnelling and the convection-diffusion equations

The concentration profile of electroactive species will generally be time dependent, however in the present work we consider the steady-state case. [22, 214] At steady state the concentration profile does not change with time and we can equate the tunnelling terms and convection-diffusion equations in order to yield Equation 7.21 in the case of an isotropic diffusion coefficient and Equation 7.22 for the near-wall hindered diffusion, which is required to be solved in order to obtain the steady-state concentration profile ($\frac{\partial[A]}{\partial t} = 0$) and calculate the resulting electrical flux.

$$0 = \frac{\partial[A]}{\partial t} = \frac{\partial}{\partial x}(D\frac{\partial[A]}{\partial x}) - v_x\frac{\partial[A]}{\partial x} - \upsilon e^{-\beta x} f_{BV}(x) \tag{7.21}$$

$$0 = \frac{\partial[A]}{\partial t} = \frac{\partial}{\partial x'}(\lambda(x')D\frac{\partial[A]}{\partial x'}) - v_x'\frac{\partial[A]}{\partial x'} - \upsilon e^{-\beta x'} f_{BV}(x) \tag{7.22}$$

subject to the boundary condition, where f_{BV} is the function of x:

$$\left.\frac{dc}{dx}\right|_{x=0} = \left.\frac{dc}{dx'}\right|_{x'=0} = 0 \tag{7.23}$$

The dimensionless form of Equations 7.21-7.22 is given below:

$$\frac{dC}{dT} = \frac{d^2C}{\partial W^2} + W^2\frac{dC}{dW} - \upsilon^* e^{-\beta^* W} F_{BV}(W) = 0 \tag{7.24}$$

$$\frac{d^2C}{dW^2} + (\frac{dln(\lambda(W))}{dW}(\lambda(W) + \frac{W^2}{\lambda(W)})\frac{dC}{dW} - \frac{\upsilon^* e^{-\beta^* W}}{\lambda(W)} F_{BV}(W) = 0 \quad (7.25)$$

They were solved subject to the boundary condition:

$$\left.\frac{\partial C}{\partial W}\right|_{W=0} = 0 \quad (7.26)$$

7.2.5 Flux and current output

The electron transfer can take place at any point in the solution with the probability given with Equation 7.8, and as a result the overall electrical flux will correspond to the sum of all flux contributions at every spatial point. The current I is proportional to the area of the electrode and is given in accordance with:

$$I = FAc^* v \int_0^\infty e^{-\beta x} f_{BV}(x)\, dx \quad (7.27)$$

7.2.6 Full model of the system

By combining knowledge of the mass transport of nanoparticles which involves convection and diffusion and the kinetics of heterogeneous electron transfer which takes place once the particles are in close proximity to the electrode (accounted by the standard Butler-Volmer model and electron tunnelling) it is possible to derive the resultant current response of the system and predict the behaviour of the colloidal suspension, which will depend on the above components. The electron tunnelling was included to allow realistic modelling of the electron transfer taking place and to avoid the apparent zero flux caused by the reduction of the diffusion coefficient at the electrode. The model is represented schematically in Figure 7.1 which shows the rotat-

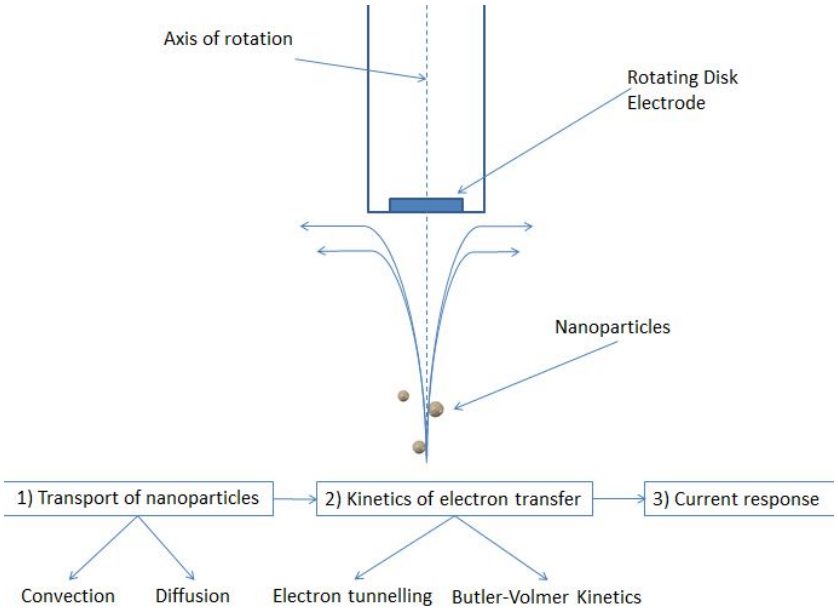

Figure 7.1: Schematic representation of the rotating disk system and the components of the theoretical model, which include mass transport of the particles, kinetic model of the electron transfer and the overall current response

ing disk electrode and the theoretical parts of the model. As the particles collide with the electrode surface they are electrolytically destroyed and as a result do not perturb the local concentration at the electrode.

7.3 Simulation

The presented model cannot be solved analytically and so numerical simulation was essential to predict the current response. The following section gives the details of the numerical algorithm and validates the presented model against previously established results.

7.3.1 Discretization and Numerical Algorithm

The Equations 7.24-7.25 were discretized, solved and plotted using Mathematica software (Wolfram Research, Inc., Mathematica, Version 10.2, Champaign, IL (2015)). The explicit Runge-Kutta method was trialled initially, but showed poor stability and excessive calculation times. Hence an implicit Runge-Kutta method [215] was used for the resolution of the numerical problem with an adaptive spatial grid through the use of the built-in solver. An expanding-adaptive grid was used for discretization. Within close proximity to the electrode the grid step-size was kept to machine level of precision (2×10^{-16}) in order to ensure accuracy of representation of the exponential decay term. The algorithm uses the previous step in order to evaluate the next step size within the specified error tolerance by comparing between several orders of Runge-Kutta methods (Orders 2-8) used to estimate the local error and adjusts the step size accordingly. Figure 7.2 shows a logarithmic plot of the step size used against the distance from the electrode, a generally high sampling density is observed in the region of close proximity to the electrode with a relatively sparse grid in the bulk in order to ensure high accuracy of the simulation in the regions where significant concentration change takes place.

7.3.2 Comparison

The numerical solution to Equation 7.21 was tested against the limiting case analytical solutions by Levich [37] for the concentration profile and steady-state limiting current(Equations 1.45-1.46) for infinitesimally small particles.

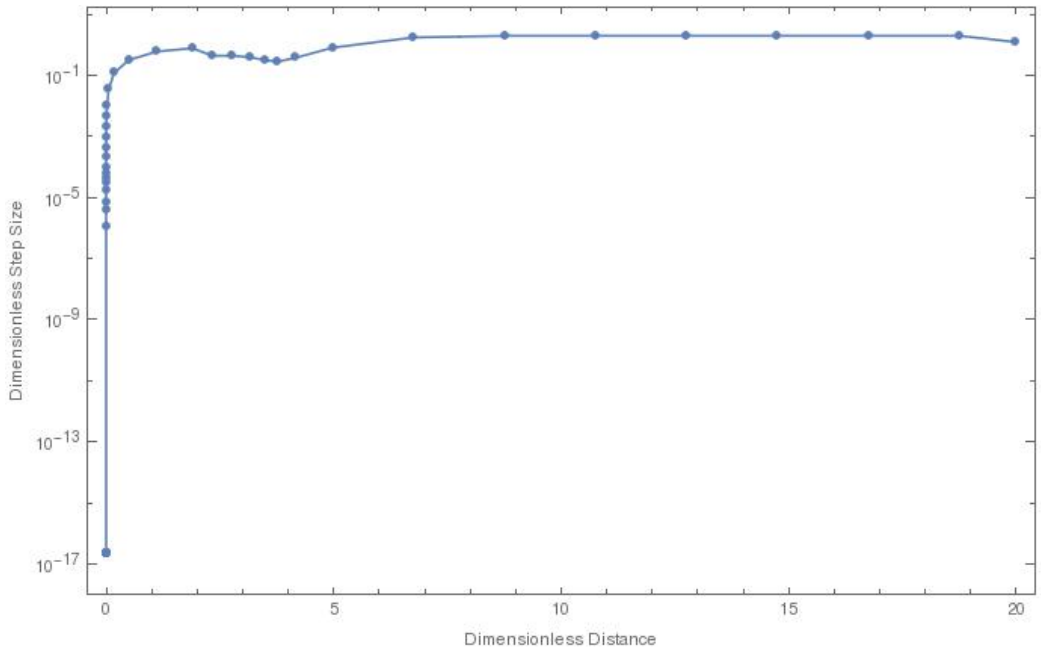

Figure 7.2: Logarithmic plot of the numerical algorithm step size as a function of distance from the electrode surface.

For convenience the Levich expression for the concentration profile was converted to dimensionless form in order to facilitate ease of comparison:

$$C(W) = 1 - \frac{\gamma\left(\frac{1}{3}, \frac{W^3}{3}\right)}{\Gamma\left(\frac{1}{3}\right)} \tag{7.28}$$

Figure 7.3 shows the resulting concentration profiles obtained analytically (solid red line) and numerically with electron tunnelling at high overpotential (dashed blue line) assuming infinitesimally small particles and hence no hindered diffusion. An excellent agreement is observed between the two calculations. The difference between the two concentration profiles is only apparent in the region close to the electrode surface as shown in the inset, where in accordance with the analytical solution the concentration decreases

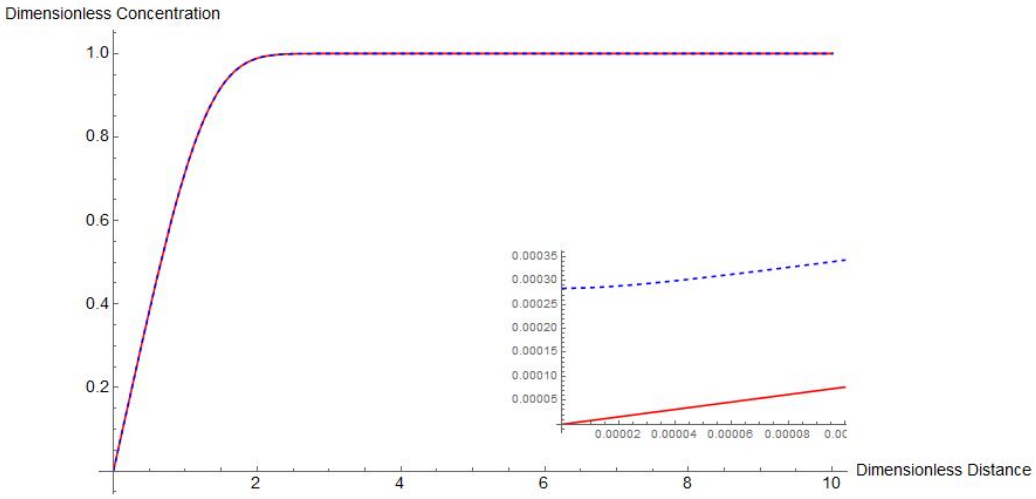

Figure 7.3: Comparison of the concentration profiles obtained analytically in the absence of electron tunnelling (solid red line) and numerically with electron tunnelling at high overpotential (dashed blue line). Equations 7.24 and 7.28 were used to calculate the concentration profiles

to zero at the electrode surface, while the simulation shows a finite concentration gradient. It is a result of a difference in terms of boundary conditions used to obtain the solutions. In the case of an analytical solution, infinite kinetics is assumed and as a result the concentration at the electrode surface is zero but for the case of electron tunnelling the boundary condition only requires the concentration gradient to be zero and as a result zero concentration will only be observed at infinite overpotential. At rotation rates orresponding to the typical experimental practice ($f = 10\ Hz$), the discrepancy in the limiting steady state current between the analytical and numerical values was found not to exceed 0.07%. In addition the effects of the heterogeneous rate constant and transfer coefficients were tested through use of Tafel analysis. The resultant plots of i_c (defined by Equation 7.29) against the overpotential, are shown in Figure 7.4 for the two limiting cases.

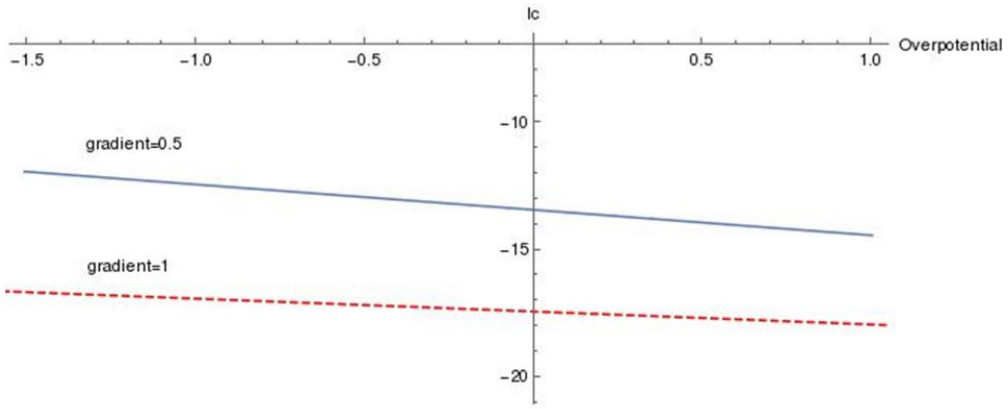

Figure 7.4: Comparison of Tafel plots obtained for reversible (blue line) and irreversible reactions (red line) and the corresponding α values

The dashed red line shows the plot for a highly electrochemically irreversible process with a dimensionless frequency constant $v^* = 6.3 \times 10^4$ and the blue line shows a highly electrochemically reversible process with an artificially high frequency constant $v^* = 6.3 \times 10^8$. (Simulation parameters used for dimensionless conversion: $R = 1 \times 10^{-4}$, $\alpha = 0.5$, $v^* = 6.3 \times 10^4$ for the irreversible case, $v^* = 6.3 \times 10^8$ for the reversible case, $\beta^* = 1.57 * 10^5$, $\eta = -15$, corresponding physical values are given in Table 7.2)

$$\ln i_c = \ln[\frac{1}{i} - \frac{1}{i_l}] \tag{7.29}$$

where i is the measured current and i_l is the limiting current. For fast kinetics ($v^* = 6.3 \times 10^8$) the gradient of the must coincide with the Nernstian limit and be equal to 1 while for the slow kinetics the gradient is determined by the α value, which in this case is equal to 0.5. Excellent agreement is observed between the theoretical values and the simulation used in the present work.

The Heterogeneous rate constant and the frequency factor relationship

The relationship between "standard" Butler-Volmer kinetics and the case of electron tunnelling was tested by taking a range of β^* values and frequency factors v^* and least square fitting of the analytical Butler-Volmer result (Equation 7.20) to the resultant plots. Figure 7.5 shows an example of steady-state voltammogram obtained using the tunnelling model and the resultant fit of the classic BV model (Parameters used: $\alpha = 0.5$, $v* = 10^8$, $R = 1 \times 10^{-4}$). A linear relationship was observed between the fitted K values and v^*, the gradient of each of the lines is close to β^*. Accordingly as suggested by Dickinson [22]:

$$v = k_0 \beta \tag{7.30}$$

Unification of electron tunnelling and the traditional Butler-Volmer Model

The simulation presented above justifies the approach used in previous works [22], where Butler-Volmer kinetics determines the rate of electron transfer, while the probability of electron transfer is guided by the the exponential fall-off and a frequency factor. As the electron tunnelling takes place the overall electrical flux is the sum of all contributions from each spatial point and can be represented by an integral defined in Equation 7.31.

$$f = \int_0^\infty v f_{BV} e^{-\beta x} dx \approx \frac{v f_{BV}}{\beta} \tag{7.31}$$

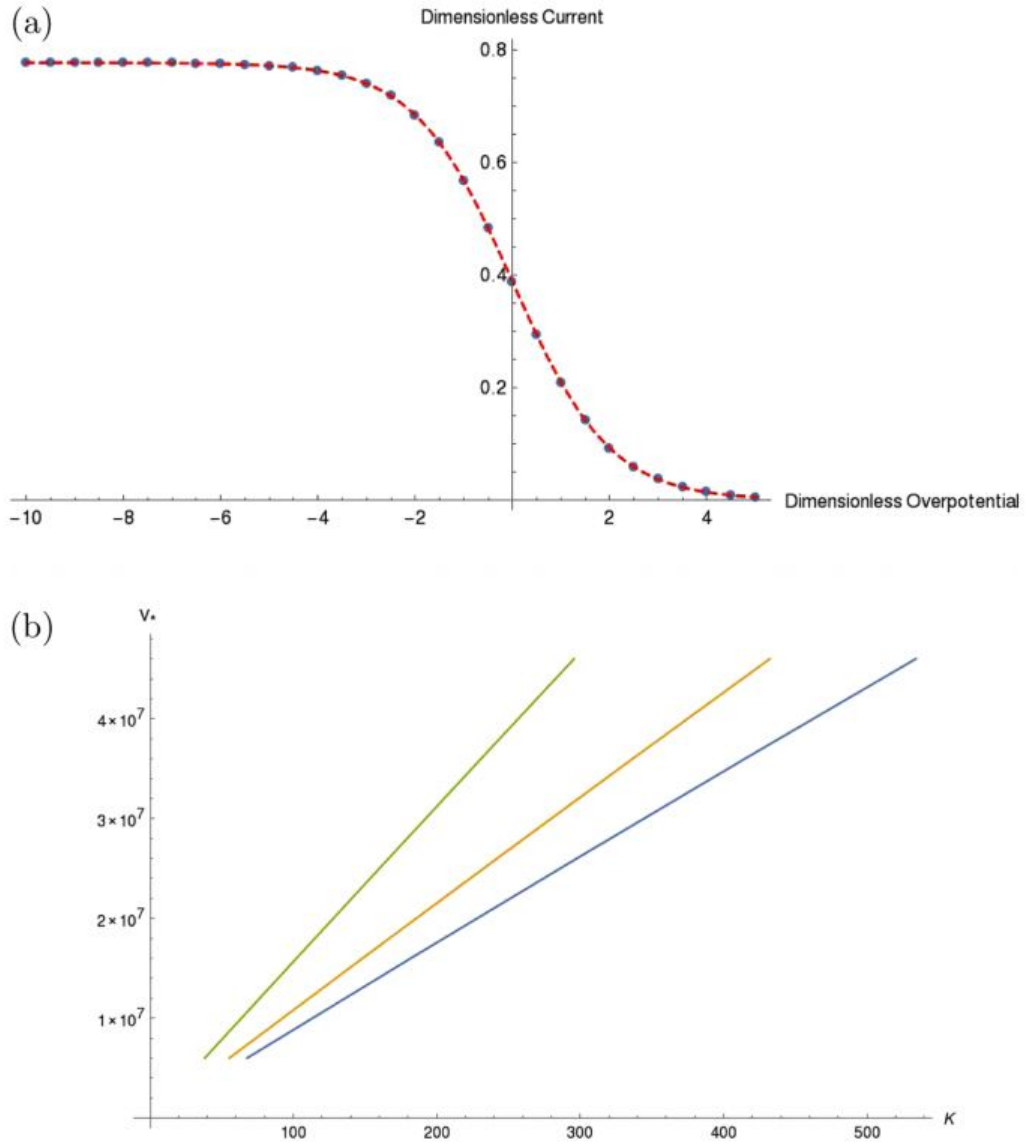

Figure 7.5: Two numerical solutions (a) Example of least squares fitting of the analytical BV model to the tunnelling simulation, red dashed line is the analytical fit and blue dotted line represent the tunnelling simulation. Parameters used: $\alpha = 0.5$, $v* = 1 \times 10^8$ (b) Dimensionlss rate constant and frequency factor relationship fitting for the two models relationship between the two values. Dimensionless Parameters: $R = 1\times10^{-4}$, $\beta^* = 8.8\times10^4$, 1.1×10^5, 1.57×10^5, $\alpha = 0.5$, $v^* = 1 \times 10^6$ to 4.5×10^7, Equations 7.20 and 7.24 were used to calculate the resultant fluxes.

β is the decay constant and f_{BV} can be taken as almost constant since the scale of tunnelling is tiny compared to the distance over which the concentration changes in the solution.

7.4 Results and Discussion

In this section we first report the concentration profiles obtained for the uniform and near-wall hindered diffusion, obtained through the solution of Equations 7.24-7.25. We then investigate the spatially distributed tunnelling current contributions for the two cases. Last the effect of the rotation rate on the resultant limiting current is taken into account and shown in terms of modified "Levich plots". The significant differences for the two cases reflect a significant reduction in the current response for the case of near-wall hindered diffusion.

7.4.1 Concentration Profiles

It is insightful to compare **simulated** concentration profiles obtained for a range of overpotentials for the uniform diffusion case and for the near-wall hindered diffusion in order to develop an understanding of the underlying physical processes. It can be clearly observed that near-wall hindered diffusion (Figure 7.6b) leads to a lower depletion of the species within close proximity to the electrode in contrast to the uniform case (Figure 7.6a). The reduced depletion is caused by the reduction in the diffusion coefficient caused by the presence of the solid boundary. The insets on both graphs show that the boundary condition (Equation 7.23) is satisfied for both cases

within close proximity to the electrode.

Figure 7.7 shows the differences between the two concentration profiles obtained where $c_{uniform} - c_{hindered}$, where $c_{uniform}$ is the uniform diffusion concentration profile and $c_{hindered}$ is the near wall hindered concentration profile. It can be seen that at high overpotential a depletion is present in close proximity to the electrode with a relatively higher concentration further away due to depletion of the layer.

7.4.2 Flux comparison for the uniform and near-wall hindered diffusion cases

Spatial dependence of the current contribution

A knowledge of the steady-state concentration profile allows the calculation of the current contribution at each point in the solution and is given in accordance with Equation 7.31. Figure 7.8 shows the distance-dependent current profile for the species for the uniform (Figure 7.8a) and near-wall hindered case (Figure 7.8b). A sharp decay is observed for the case of the uniform diffusion, which is consistent with the sharp decay of tunnelling probability. At high negative overpotentials higher current contribution are observed within close proximity to the electrode. In both cases the electron transfer process is confined to a finite tunnelling zone and decreases to zero with increasing distance. Surprisingly for the near-wall hindered case a peak appears at high negative overpotentials. Its appearance can be ascribed to the depletion of the species in close proximity to the electrode which results in an overall low contribution to the electrical flux. Further evidence is

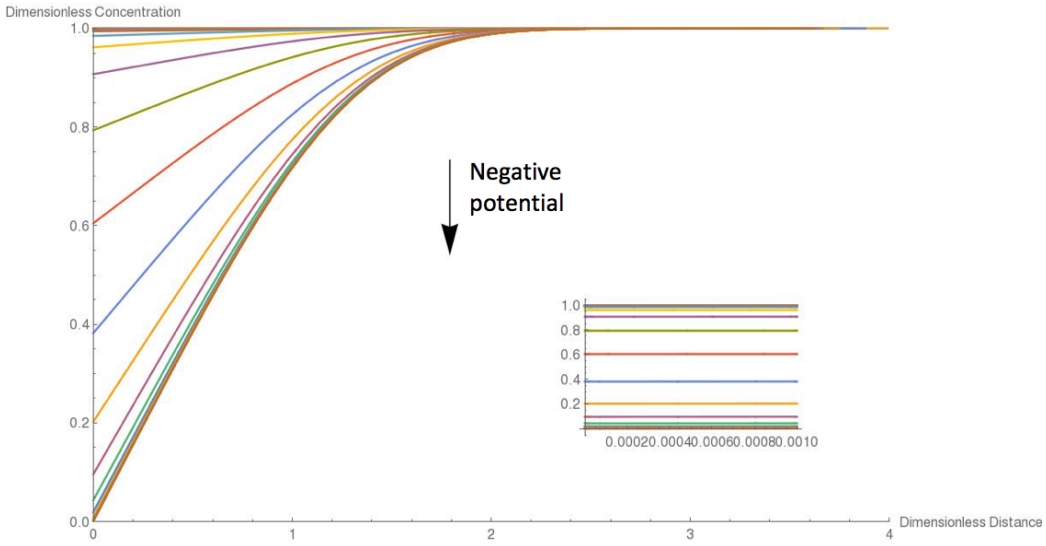

(a)

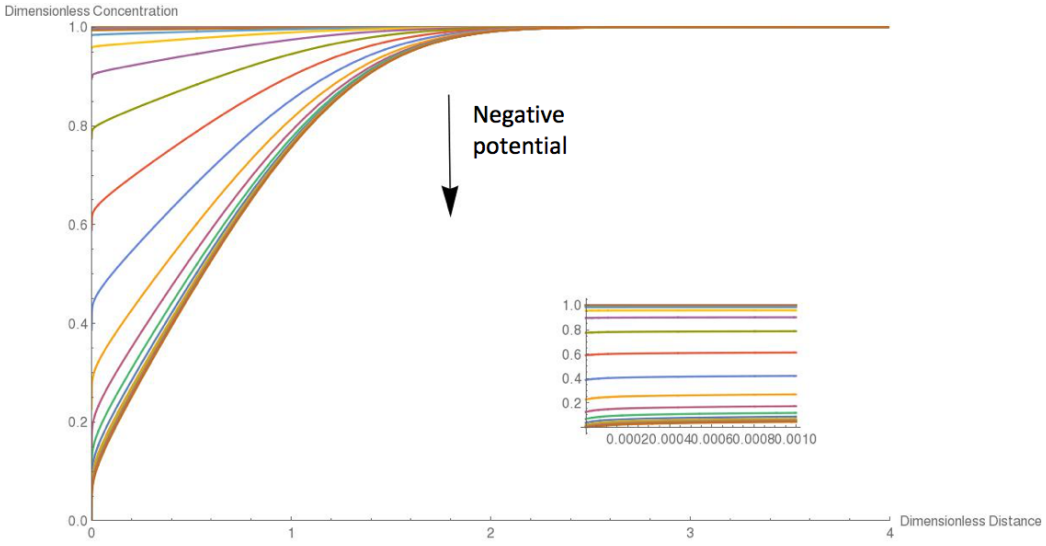

(b)

Figure 7.6: (a) Uniform diffusion concentration profile for dimensionless potentials -15 to +10, inset shows region within close proximity of the electrode (b) Near-wall hindrance concentration profile for overpotentials -15 to +10, inset shows region within close proximity of the electrode. Dimensionless Parameters: $R = 1.86 \times 10^{-2}$, $\alpha = 0.5$, $v* = 2.3 \times 10^{7}$, $\beta^{*} = 0.42 \times 10^{5}$. Equations 7.24 and 7.25 were used to calculate the resultant concentration profiles.

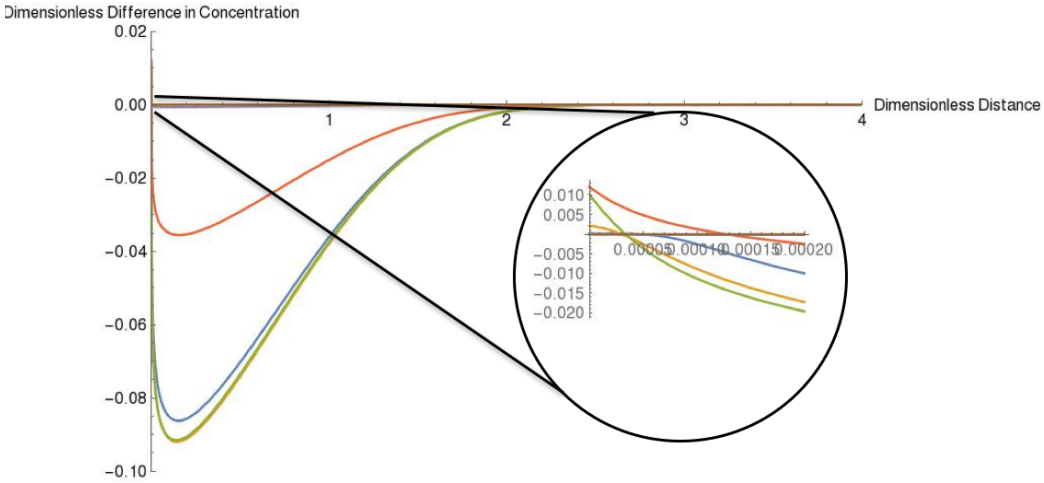

Figure 7.7: Difference of the concentration profiles obtained for uniform and near-wall hindered diffusion. Dimensionless Parameters: $R = 1.86 \times 10^{-2}$, $\alpha = 0.5$, $v^* = 2.3 \times 10^7$, $\beta^* = 0.42 \times 10^5$. Equations 7.24 and 7.25 were used to calculate the resultant concentration profiles and the curves correspond to different potentials.

the fact that at higher potentials the maximum current contribution shifts further away from the electrode as the depletion layer increases. (Note that this observation might also be attributed to the physical unreality of the Butler-Volmer model at highly negative potentials where infinite rates of electron transfer are predicted; for such cases Marcus-Hush theory may be more realistic.)

Steady state voltammetry response for the uniform and near-wall hindered diffusion

In accordance with Equation 7.27 the current output was calculated and the following parameters were used for the conversion to the dimensional form: $A = 7.85 \times 10^{-5}\ m^2$, $c = 1 \times 10^{-3}\ mol\ m^{-3}$. Figure 7.9 show the steady-

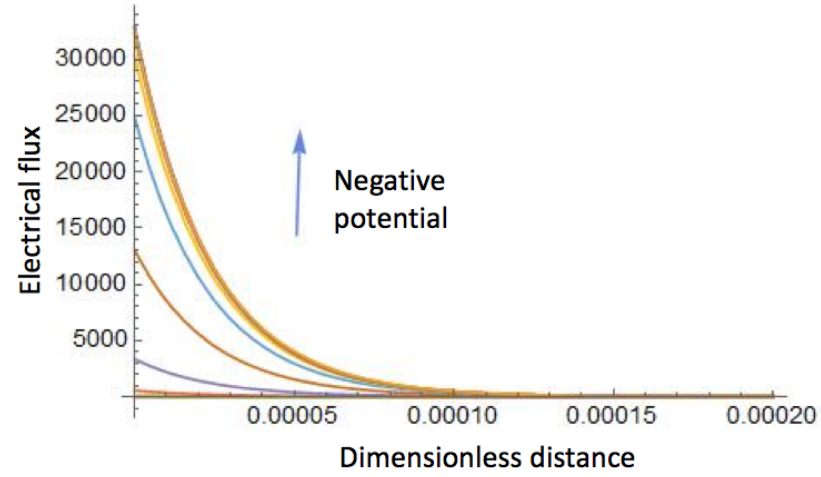

(a)

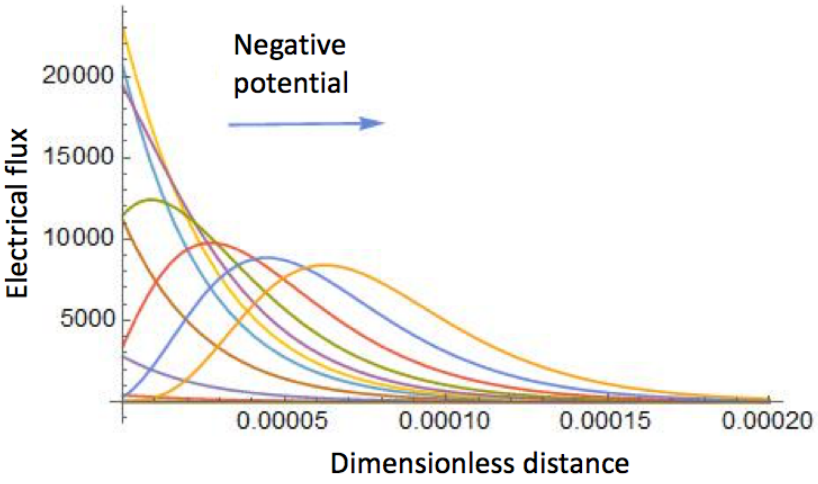

(b)

Figure 7.8: (a) Uniform spatial electrical flux contribution for overpotentials -15 to +10 (b) Near-wall hindrance electrical flux contribution for overpotentials -15 to +10. Dimensionless Parameters: $R = 1.86 \times 10^{-2}$, $\alpha = 0.5$, $v^* = 2.3 \times 10^7$, $\beta^* = 0.42 \times 10^5$. Equations 7.24, 7.25 and 7.31, were used to calculate the resultant concentration profiles and the curves correspond to different potentials.

state voltammograms in the presence and absence of the near-wall hindrance. There is a clear difference between the predicted current responses for the two cases. For low positive dimensionless overpotentials ($\approx 2-10$) the effect of near-wall hindrance is not significant due to the fact that the current response is limited kinetically and not by the mass transport of the species. However it can be clearly seen that the effect becomes increasingly important at high potentials due to depletion of the diffusion layer at the electrode and significant deviations are observed for large particles.The effect is size-dependent and the discrepancy increases with increasing size of a particle.

7.4.3 Effect of the rotation rate on the limiting current response

The rotation speed of the disk has an effect on the thickness of the hydrodynamic layer in accordance with the Equation 1.41 and as a result at higher rotation rate the limiting current is expected to be proportional to the square root of the rotation rate in accordance with the Equation 1.46. As a result a linear relationship is expected for the uniform diffusion coefficient but deviations are expected for the case of hindered diffusion. The plot of limiting current against $\sqrt{\omega}$ is known as a 'Levich plot'. Figures 7.10a-7.10b shows Levich plots for particle sizes of 10 and 50 nm. For the 10 nm particle a small deviation is observed at higher rotation but an overall increasing trend is seen as for uniform diffusion. However for the larger 50 nm nanoparticles a significant deviation is observed at higher rotation rates and the plot is

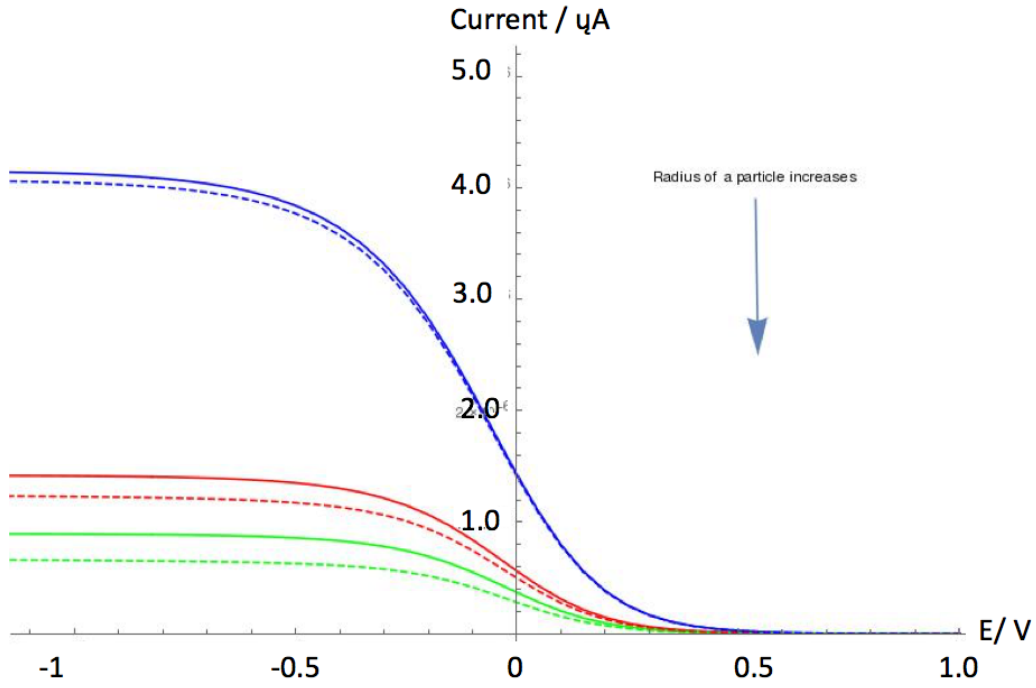

Figure 7.9: Comparison of linear scan voltammograms for the uniform (solid line) and near-wall hindered (dashed line) cases. The particle radii used in the simulation are 10, 50 and 100 nm respectively. Simulation parameters used $f = 10\ Hz$, $\alpha = 0.5$, $\beta = 1.57 \times 10^{10}\ m^{-1}$, $k_0 = 0.001\ ms^{-1}$, Equations 7.24 and 7.25 were used to calculate the resultant concentration profiles.

non-linear. For the case of 10 nm particle the calculated adjusted R^2 value for linear fit was found to be 0.999875, which is indicative of a closely linear fit. By contrast for the case of 50 nm the calculated adjusted R^2 was 0.996945, which is indicative of the deviation from linearity. As the particle size increases the deviations from linearity increase.

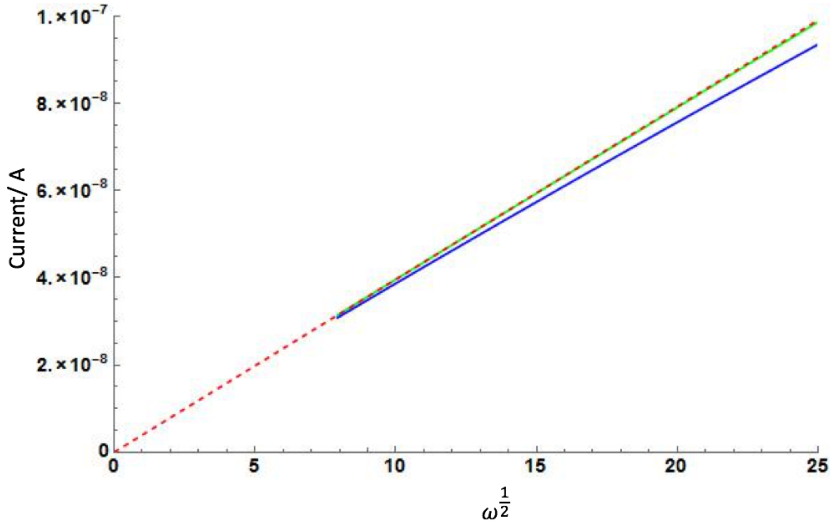

(a)

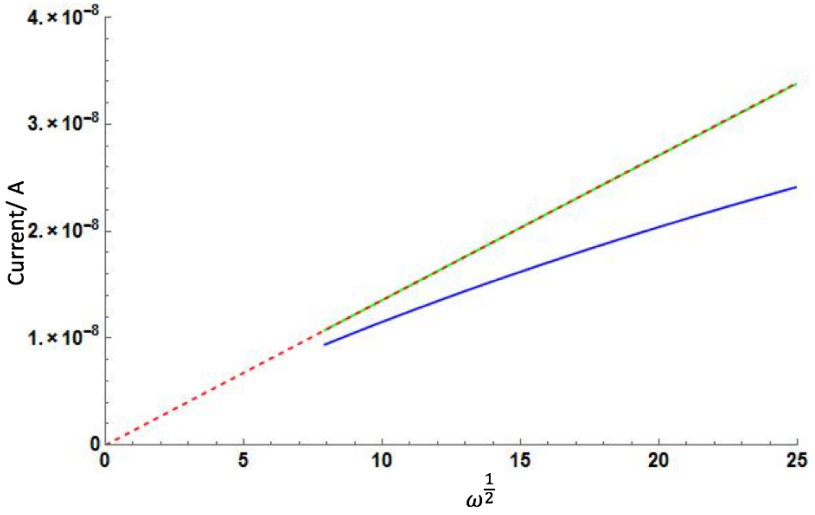

(b)

Figure 7.10: (a) Levich plots for a particle with a radius of 10 nm: analytical solution (dashed red line), uniform diffusion coefficient with tunnelling (green line) and near-wall hindered diffusion (blue line)(b) Levich plots for a particle with a radius of 50 nm, same color lines were used. Other parameters Simulation parameters used $f = 10\ Hz$, $\alpha = 0.5$, $\beta^* = 1.57 \times 10^{10}\ m^{-1}$, $k_0 = 0.001\ ms^{-1}$, $\eta = 15$. Equations 1.46, 7.24 and 7.25 were used to calculate the electrical flux response.

7.5 Conclusions

In the case of a convective system a significant impact on mass transport is caused by the near-wall hindrance. The effect is particularly significant for the development of nanoparticle sensors and novel-battery technologies. For a rotating disk, the near-wall hindrance becomes significant at high overpotentials and high rotation rates and will have a significant effect on applications which rely on these characteristics. Design of the novel nanoparticle sensors and applications such as fuel cells and batteries requires rethinking of the traditional approach to the electrochemical simulations, as approximations valid for molecules are no longer accurate for the case of colloidal suspensions and as a result may lead to a significant error. In addition, analysis of the near-wall diffusion hindrance requires the introduction of distance-dependent, electron-tunnelling and the traditional measurement of the electrical flux in terms of the concentration gradient at the electrode is invalid. In the next chapter the use of forced convection for practical nanoparticle detection will be discussed in a wall-jet flow cell and an array of microelectrodes. The resulting limit of detection is more than 2 orders of magnitude smaller than the previous detection limit for direct-impact voltammetry (900 fM [47]), and is more than 30 times smaller than the previous detection limit for mediated-impact voltammetry (83 fM [216]).

Chapter 8

Femtomolar Detection of Silver Nanoparticles by Flow-Enhanced Direct-Impact Voltammetry at a Microelectrode Array

In Section (1.7) various nanoparticle detection techniques were discussed. The particle-electrode impacts technique was discussed as a cheap, alternative to common light scattering methods such as dynamic light scattering or nanoparticle tracking analysis. In the present chapter a purpose-built flow cell coupled with a random assembly of microelectrodes is presented. A femtomolar limit of detection is achieved for a system of citrate-capped silver nanoparticles. The work was performed in collaboration with Mr. (now Dr.)

Thomas R. Bartlett (University of Oxford, Department of Chemistry), who jointly conducted particle-electrode impact experiments and data analysis. Dynamic lights scattering measurements were performed by the author. The outcome has been published in Analytical Chemistry [217].

8.1 Introduction

Nanoparticles find applications in a wide range of industrial [128] and medical applications. [58] Often these materials are used as slurries or aqueous suspensions. The properties of the nanoparticles are size-dependent. For example the surface plasmon resonance for metallic nanoparticles [77], UV absorption power of TiO_2 particles [218] and magnetic properties of Fe_3O_4 NPs [219], all vary as a function of nanoparticles size. Light scattering techniques are traditionally the dominant means of sizing nanoparticles.The particular advantages of these techniques being: ease of sample preparation, in situ sample characterization and fast measurement times. The most common optical methods are: UV-vis spectroscopy, dynamic light scattering and nanoparticle tracking analysis. UV-vis spectroscopy allows for the detection of monodisperse metallic NP samples; yet, it is limited by inaccuracies in measuring polydisperse systems and the requirement of the surface plasmon resonance. [220] In addition the determination of concentration via UV-vis requires calibration and consequently is difficult for unknown samples. Dynamic light scattering is capable of sizing large range of particle sizes but is known to be affected by the presence of the large clusters due to the intensity scattering scaling with the radius $I \propto r^6$ as discussed in Section 2.2.

Consequently the size distribution may be skewed towards larger particle sizes. Further DLS does not provide concentration information. Nanoparticle tracking analysis operates by tracking the diffusion of individual particles on a frame by frame basis and consequently is less affected by polydispersity. By counting the number of particles in a given time frame the concentration of the sample can be estimated. NTA can operate with samples consisting of $10^7 - 10^9$ particles per mL, which is equivalent to a lower limit of detection of 16.6 fM. [81]. All light scattering techniques are unable to operate in optically opaque media, which is a significant disadvantage for the environmentally relevant samples.

Electrochemical approaches to nanoparticle sensing offer an attractive alternative and can operate in environmentally-relevant media. [221] Traditional "sticking and stripping" [222, 223] can provide information regarding the chemical identity of the particles, but lack the insights about the particle size distributions. The experimental interpretations are also complicated by incomplete oxidation/reduction of the particles due to surface aggregation and/or agglomeration upon drying and the effects of the capping agent. [95, 224, 225] The particle-electrode impacts method overcomes this limitation and allows sizing of individual nanoparticles as discussed in depth in Section 2.3.3. Two strategies have been employed to date: direct Faradaic impacts and mediated catalytic impacts. Direct-Faradaic impacts have been conducted in stationary electrolyte solutions and under these sets of conditions the use of microwires electrodes is preferable due to the increased surface area and has been shown to achieve a detection limit of 900 fM. [47] An alternative mediated impact approach has been demonstrated

by Crooks *et al.* who used silver nanoparticle functionalised magnetic microbeads to enhance the collision rate at the electrode. The reported silver detection limit was 61 fM. [226] For real-world practical applications, sensors require low operating costs, simplicity of operation and a fast response. Mediated and magnetically guided bead/particle impacts while interesting from a research point of view, challenge these requirements and an alternative is warranted. In the present work, we focus on direct-impact electrochemistry and extend the direct Faradaic approach to convective systems.

In Section 1.6.2 the use of forced convection was discussed from an analytical point of view. Hydrodynamic electrodes allow the compression of the diffusion layer at the electrode surface, which leads to a steeper concentration gradient and consequently enhanced mass transport. RDE electrodes and wall-jet cells have been the two common approaches used to date. The RDE has a significant advantage of uniform accessibility [36, 37], which a wall-jet cell lacks. As a result more complex two dimensional modelling is required to account for the variability of the diffusion layer thickness as a function of distance from the impinging jet. [41] However for practical applications a wall jet electrode cell comprised of a a fully sealed unit with a large flow throughput may be advantageous due to the fast in situ detection capabilities. Consequently flow cells have found applications in both research and industry with examples of study biological redox processes [227] and heavy metal detection. [228, 229]

In addition to using forced convection, the limit of detection can be lowered by increasing the electroactive area of the detector. The capacitative noise scales with the square root of the electroactive area ($N \propto \sqrt{A}$) [230]

and as a result macro-electrodes are not suitable for particle electrode impacts. Microwire electrodes demonstrate high signal to noise ratios and large electroactive areas. [47, 230] However in order to be used in conjunction with a forced convection regime of mass transport, the electrode needs to be stable under a flow regime. Consequently the application of microwire electrodes in flow systems is challenging. Therefore, an alternative is sought that provides an inherently high signal to noise ratio while measuring the collision frequency under flow to allow low limits of detection. Arrays of gold (Au) microelectrodes with 25 μm for the smaller diameter and $30-180$ μm for the larger diameter have been adapted from conventional electronic integrated circuit chips. [231, 232] However, these are rather large, and smaller carbon electrodes are preferred for the present purposes of single nanoparticle detection. For this reason, we use the random array of microelectrodes (RAM) approach pioneered by Fletcher and Horne. [52] These RAMs consists of hundreds of carbon fibers connected in parallel to a current collector. This arrangement provides current amplification proportional to the number of active fibers, while maintaining radial diffusion. RAMs can also be repolished to provide a clean and reproducible surface, facilitating ease of use and maximizing applicability to real systems.

The ultimate limit of detection in impact electrochemistry is a single entity; however, the technique suffers because the time that is required for the entity to reach the probe by random walk alone can be of the order of tens of thousands of seconds for extremely dilute samples. [18] In the present chapter we describe a method to increase the rate with which entities collide with an electrode by invoking convective mass transfer using a flow cell,

allowing for the analysis of femtomolar levels of Ag NPs. The flow response of the system is first characterized by the molecular redox species potassium ferrocyanide. This is then extended to the concurrent detection and sizing of citrate-capped Ag NPs at femtomolar concentrations with the effect of volumetric flow rate on the frequency of impacts reported.

8.2 Experimental

8.2.1 Nanoparticle Characterization

Citrate-capped Ag NPs were characterized by DLS analysis (Malvern Zetasizer, Malvern, U.K.) using general purpose sizing mode and were found to be 58 ± 18 nm in diameter with a Ag content of 0.02 $mg\ mL^{-1}$, stated by the manufacturer. The stock solution was therefore estimated to have a Ag NP concentration of 31.0 pM under the assumption of the spherical nanoparticle geometry.

8.2.2 Electrodes

Two RAMs were used as working electrodes for experiments, consisting of hundreds of carbon fibers ($r = 3.5\mu m$) insulated with cured epoxy resin and having an average electrode separation of $70\mu m$. While different RAMs were used in various experiments, the results were normalized by the number of active fibers for each RAM to allow direct comparison. The number of active fibers varies between RAMs, because of the manufacturing process, and was calculated as follows. Cyclic voltammetry of the RAMs was conducted

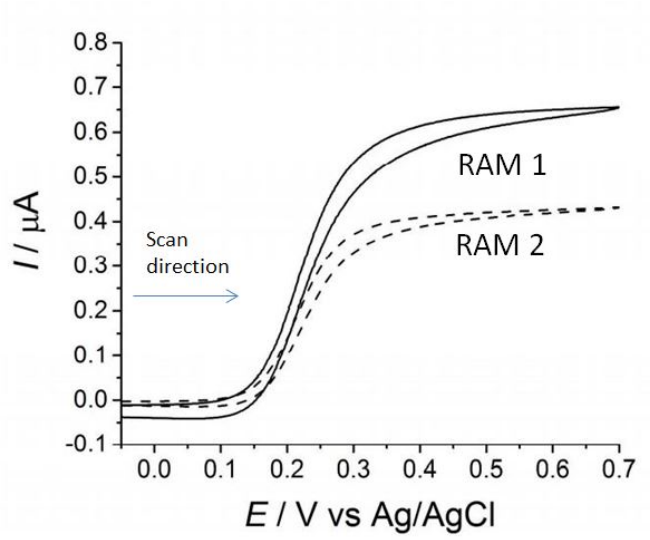

Figure 8.1: Characterization of the two RAMs used for experiments in 1mM $K_4Fe(CN)_6$ in 0.10 M KCl. Start potential of -0.05 V vs Ag/AgCl at a scan rate of 100 $mV\ s^{-1}$.

under stationary conditions in 1 mM $K_4Fe(CN)_6$ and 0.10 M KCl at 100 $mV\ s^{-1}$ and is reported in Figure 8.1. The diffusion layer thickness around an individual fibre for a 60 second measurement and a $K_4Fe(CN)_6$ diffusion coefficient of $0.66 \times 10^{-5}\ cm^2 s^{-1}$ [233] can be estimated in accordance with $\delta \approx \sqrt{Dt} \approx 80\ \mu m$ [1] . The individual fibres are separated by 70 μm and consequently given the timescale of the measurements ($t < 60\ s$) can be considered approximately diffusionally independent. This is evidenced by the observed steady-state response for both RAMs in Figure 8.1

The limiting current obtained can be related to the number of active fibers (N_{fib}), assuming a fiber radius of $3.5\mu m$ and a microdisk geometry:

$$N_{fib} = \frac{I_{lim}}{4 r_{fibre} n F D c^*} \tag{8.1}$$

where I_{lim} is the limiting current, r_{fibre} the radius of the fiber, D the diffusion coefficient, and c^* the concentration of $K_4Fe(CN)_6$. Using this equation, the RAMs were found to have 663 ± 5 and 436 ± 3 functional fibers, respectively.

8.2.3 Flow cell design

The flow cell was designed and built in-house with an assistance from Mr. Peter Fair (University of Oxford, Physical and Theoretical Chemistry Laboratory Workshop). It allows the interchange of working electrodes, with a washer allowing control over the inlet- working electrode distance. A schematic design is shown in Figure 8.2, and full schematics are reported in the Appendix B. shows the demountable flow cell system, which is built from three separate sections that are bolted together. In order to ensure chemical stability, the three main cell components were manufactured from polyether ether ketone (PEEK), with Delrin used for the reference and working electrode holder. During operation, the solution is flowed through the cell, using a computer-controlled Fusion 100 Chemyx syringe pump (USA), and is injected onto the electrode surface through a 0.5 mm diameter inlet hole. The inlet-electrode distance can be altered by using different washer thicknesses; however, the distance was maintained at 2 mm for all experiments conducted herein. The flow is then strained by the central component through 8 pores, each 0.5 mm in diameter, before passing into a pressure-equalizing well containing the counter and reference electrodes. The positioning of the electrodes in this cell ensures that the electroactive solution components cannot be affected by the counter electrode before reaching the

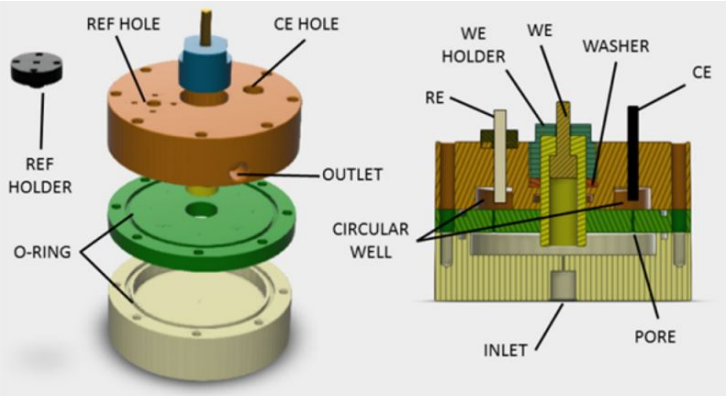

Figure 8.2: Expanded and cross-sectional views of the home-built flow cell working electrode.

8.2.4 Mass transport characterization using macro-electrode

Traditionally wall-jet cells used macro-electrodes as a working electrode. Most of the theoretical derivations are hence applicable to such systems. The electrochemical behaviour of the in-house designed flow cell was determined via linear sweep voltammetry of 1 mM $K_4Fe(CN)_6$ in 100 mM KCl at a scan rate of 1 $mV\ s^{-1}$. The resultant voltammograms for different flow rates are shown in Figure 8.3. Due to the convective mass transport steady state behaviour is observed. Steady-state limiting current values (I_{lim}) were plotted as $log_{10}(I_{lim})$ vs $log_{10}(flow\ rate)$, as shown in Figure 8.4. The gradient of the resultant line was determined via least-squares fitting to obtain a slope of 0.74 ± 0.08. This is in excellent agreement with the theoretical prediction in accordance with the Levich equation for a wall jet [1] with $I_{lim} \propto V_f^{\frac{3}{4}}$:

$$I_{lim} = 1.35nFD^{\frac{2}{3}}v^{-\frac{5}{12}}a^{-\frac{1}{2}}r_e^{\frac{3}{4}}V_f^{\frac{3}{4}}c^* \tag{8.2}$$

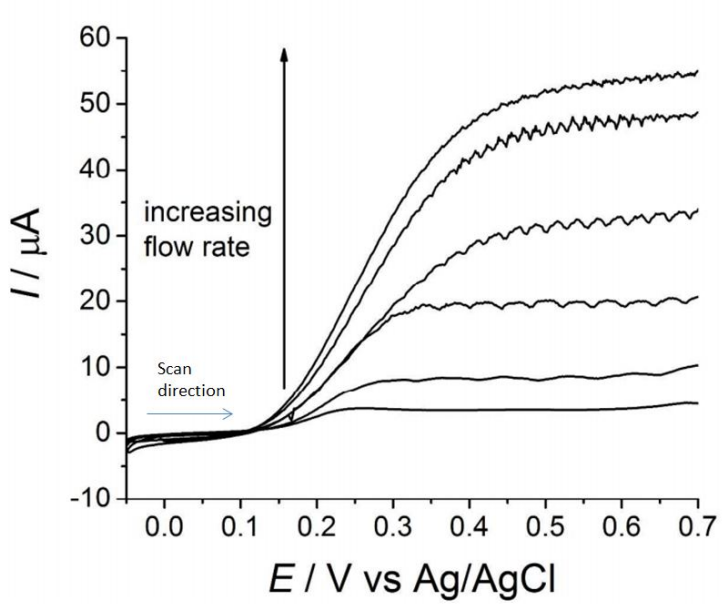

Figure 8.3: Flow dependence of GC macroelectrode in 1mM $K_4Fe(CN)_6$ in 100 mM KCl, start potential of -0.05 V vs Ag/AgCl at a scan rate of 1 $mV\ s^{-1}$ at 0, 0.5, 1.0, 1.5, 2.5, 3.0 $mL\ min^{-1}$

where v is the kinematic viscosity (for water $v = 1.004 \times 10^{-6}\ m^2 s^{-1}$ at $25°C$), a is the diameter of the jet nozzle ($a = 2 \times 10^{-3}\ m$), V_f is the volumetric flow rate. As a result the observed flow behaviour is consistent with the expected theoretical response.

8.2.5 Mass transport characterization using a RAM electrode

Having confirmed the wall-jet behaviour of the manufactured cell using a macro-electrode, the effects of flow on the response for molecular species was studied using a RAM working electrode. This provided an estimate of the possible decrease in detection limit achievable by this system. Linear sweep

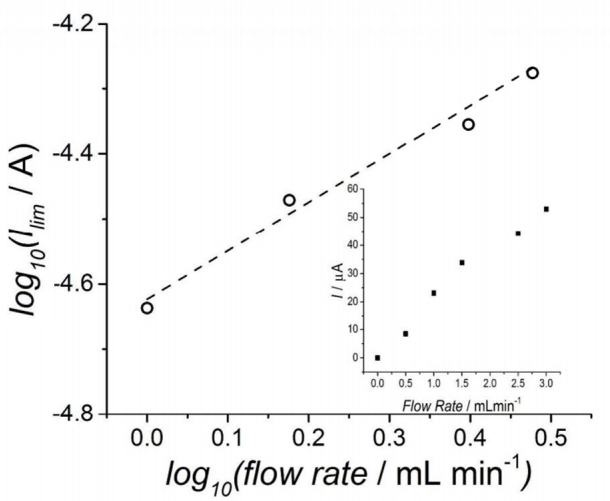

Figure 8.4: Log/log plot of I_{lim} vs volumetric flow rate for GC macroelectrode in 1mM $K_4Fe(CN)_6$ in 100 mM KCl , start potential of -0.05 V vs Ag/AgCl at a scan rate of 1 $mV\ s^{-1}$ Fitting shows a slope of 0.74 ± 0.08 for flows of 1 to 3 $mL\ min^{-1}$ consistent with wall-jet behaviour at flow rates greater than 1 $mL\ min^{-1}$

voltammetry was conducted in 1 mM $K_4Fe(CN)_6$ and 100 mM KCl from -0.05 V to +0.70 V vs Ag/AgCl at 100 $mV\ s^{-1}$ across a range of flow rates. Figure 8.5 shows the resultant steady-state voltamogramms obtained at 0, 6, 20, 35, and 50 $mL\ min^{-1}$. A steady-state response is observed both under stationary and flow conditions, confirming the diffusional independence of the individual microfibers in the RAM. As the volumetric flow increases, the steady-state response is maintained, along with an increase of the I_{lim}. Figure 8.6 shows a 'Levich' plot of $log_{10}(I_{lim})$ vs $log_{10}(flow\ rate)$ for a range of flows from 0 to 50 $mL\ min^{-1}$. A clear linear trend is observed with a slope of 0.41±0.01. The dependence of the transport limited current at the RAM with flow rate is less than that observed for the GC macroelectrode (gradient= 0.74 ± 0.08). This reflects the changed electrode geometry and indicates that the RAM is comprised of many microelectrodes, each of which has a

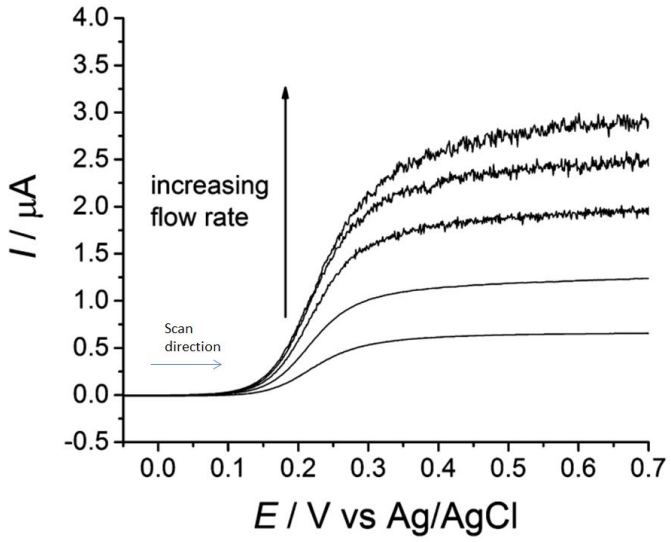

Figure 8.5: Flow dependence of RAM in 1 mM $K_4Fe(CN)_6$ in 100 mM KCl, start potential of -0.05 V vs Ag/AgCl at a scan rate of 100 $mV\ s^{-1}$ at 0, 6, 20, 35, and 50 $mL\ min^{-1}$.

lower sensitivity to flow, compared to a macroelectrode. The increase in the limiting current from a diffusional-only regime to the maximum volumetric flow rate used of 50 $mL\ min^{-1}$ was found to be from 0.63 μA to 2.90 μA, equivalent to an enhancement of signal of almost five times.

8.3 Results and discussion

Having characterised the mass transport characteristics of the designed cell, particle-electrode impact experiments were conducted. Current transients were recorded for twenty seconds at a potential of +0.60 V vs Ag/AgCl at a NP concentration of 6.2 fM in 40 mM KCl across the experimental flow range of 0-50 $mL\ min^{-1}$. Figure 8.7 shows the resultant chronoamperograms for a range of flow rates and the enlarged spike observed in the presence of the

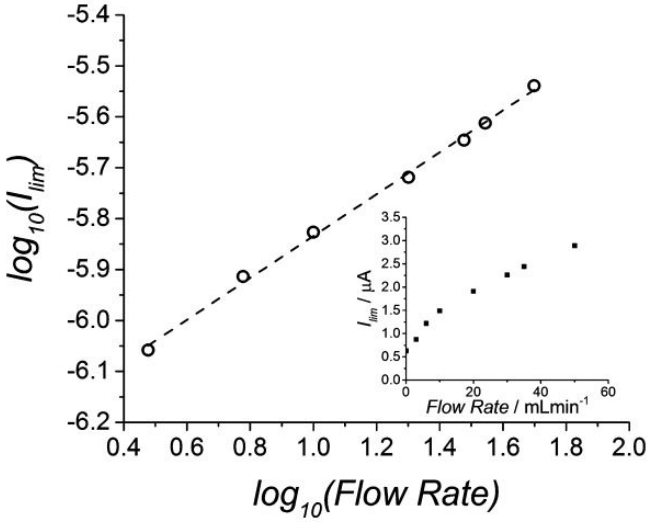

Figure 8.6: Log/log plot of I_{lim} vs volumetric flow rate for a RAM in 1 mM $K_4Fe(CN)_6$ in 100 mM KCl, at a scan rate of 100 $mV\ s^{-1}$ with a slope of 0.41 ± 0.01. Inset shows a plot of I_{lim} versus the volumetric flow rate.

silver nanoparticles. This potential was chosen because it is suitable for the complete oxidation of Ag NPs up to 100 nm in diameter. [234]. No impacts were observed under stationary flow, because of the low concentration. When the NP suspension was flowed at 10 $mL\ min^{-1}$, current spikes were detected, indicative of Ag NP oxidation. The frequency of spikes was observed to increase with increasing volumetric flow rate. The noise of the system was not significantly affected by flow rate and remained below 100 pA, even at the highest flow rate of 50 $mL\ min^{-1}$, allowing clear, unambiguous detection of the current spikes. The observed increase in the background current is likely due to surface oxidation of the RAM electrodes and/or residual citrate used for capping the particles. The frequency of the observed impacts scales linearly with the flow rate as shown in Figure 8.8.

In order to test the sensitivity of the detection method a lower concen-

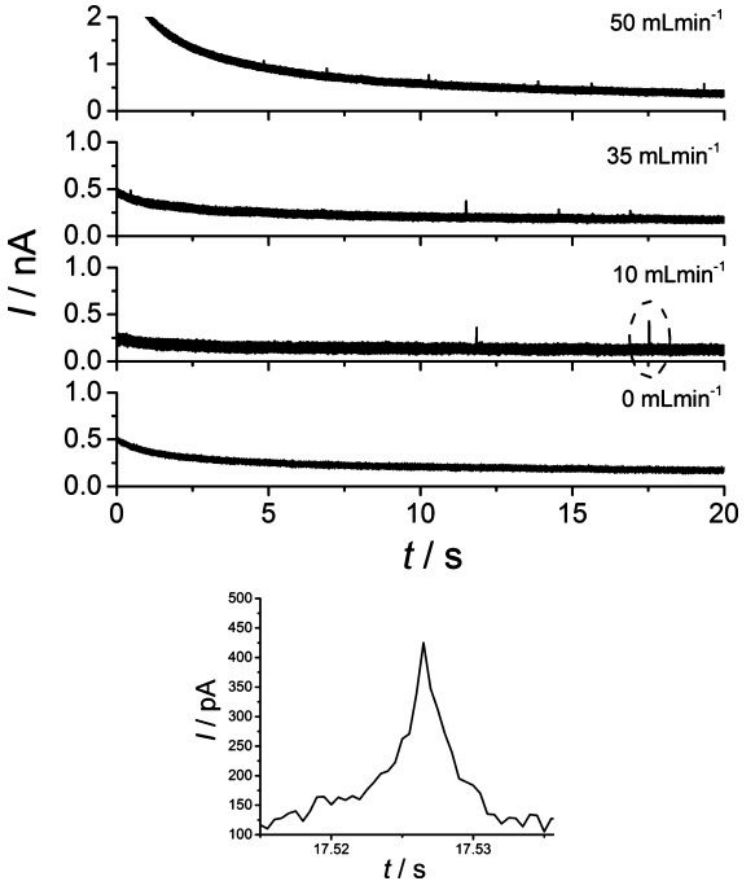

Figure 8.7: Example current-time transients recorded at varying flow rates showing nanoimpact spikes. Current-time transients were conducted at +0.60 V vs Ag/AgCl at a Ag NP concentration of 6.2 fM in 40 mM KCl. Inset shows an enlarged image of a current spike at 10 $mL\ min^{-1}$ (circled region in top portion of the figure).

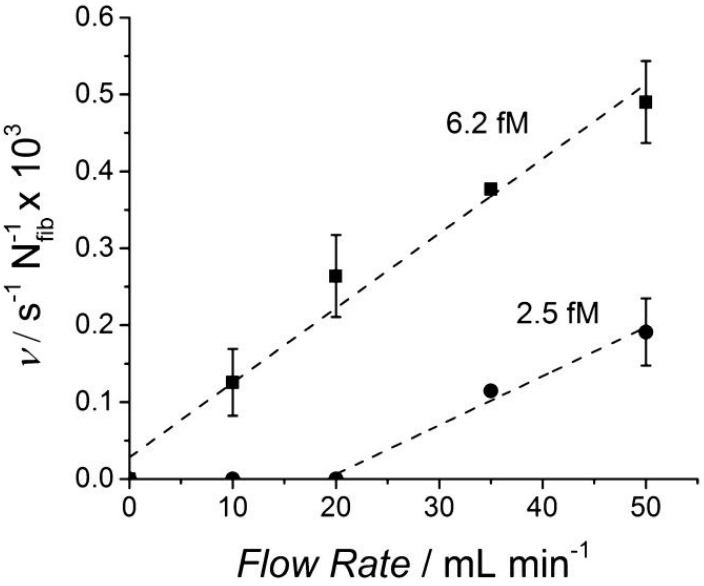

Figure 8.8: Nanoimpact frequency at RAMs at varying volumetric flow rates at a Ag NP concentration of 6.2 fM and 2.5 fM (No impacts were observed at a Ag NP concentration of 2.5 fM with volumetric flow rates up to 20 $mL\ min^{-1}$). Current-time transients were conducted at +0.60 V vs Ag/AgCl reference electrode in 40 mM KCl.

tration of 2.5 fM NPs was studied under the same conditions. Figure 8.8 shows the change in impact frequency with flow rate for this concentration and 6.2 fM. No impacts were observed at a Ag NP concentration of 2.5 fM with volumetric flow rates up to 20 $mL\ min^{-1}$. It can be seen that, for the lower concentration, high flow rates are required to detect particle impacts, and this stresses the benefits of flow over diffusion-only mass transport for NP impact voltammetry. By increasing the flow rate to 35 $mL\ min^{-1}$, NP impacts were detected on the time scale of the measurement. This is the lowest concentration of NPs (2.5 fM) ever used in a successful nanoimpact experiment, with an enhancement in experimental level of detection by two orders of magnitude over earlier attempts [95] and by one order of magnitude for mediated impacts. [226]

An additional benefit of nanoimpacts over DLS, is the ability to size individual impacting nanoparticles. By sampling a statistically significant number of particles (hundreds of particles), the sample size distribution can be deduced. The size distribution obtained via nano-impact method (bar chart) was compared to the distribution obtained using dynamic light scattering (dashed line) as shown in Figure 8.9. The mean size of the particles determined by nanoimpact voltammetry and DLS was determined to be $57.0 \pm 5nm$ and 58 ± 18 nm, respectively. The wider standard deviation of the DLS size distribution can be potentially due to presence of large clusters, which may affect the correlation function. As a result *quantitative* sizing of the particles as well as ability to detect Ag NP at a concentration of 6.2 fM was confirmed. Hitherto, the lowest reported experimentally detected concentration of NPs by direct impacts is 900 fM, using a carbon fiber microwire electrode. [47]

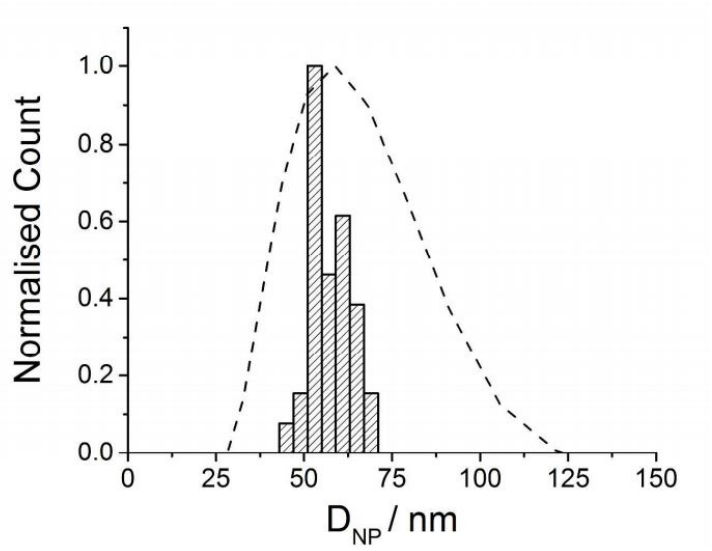

Figure 8.9: Comparison between nanoimpact (dashed grey bars) and DLS (dashed line) distributions. Nano impact distribution was gained by integration of current spikes across all measured flow rates. (244 Spikes)

Nonspecific adsorption is inherent in NP chemistry and can have an effect on the concentration of NPs in suspension. As a result, a lower frequency of impacts may be observed, leading to errors in concentration estimates. In addition, care must be taken to minimize agglomeration/ aggregation during nanoimpact experiments.

8.4 Conclusions

Femtomolar nanoparticle (NP) concentrations of citrate-capped silver nanoparticles have been detected for the first time by direct-Faradaic impact voltammetry, because of the enhancement of mass transport by flow. The method detailed herein allows determination of the presence of NPs and their concurrent sizing. We have demonstrated that the frequency of impacts increases

monotonically as the concentration increases. This is an improvement of more than two orders of magnitude in the detection limit, relative to that previously reported. [95] This extremely sensitive detection is a direct result of combining flow with a RAM electrode, increasing the signal-to-noise ratio. The presented method can be adjusted for sizing smaller NPs by choosing different array geometries in order to have suitable noise characteristics. This is of significant importance for the field of analytical NP detection. Further applications of the developed methodology may include applications to biological systems with the objective of the development of point of care sensors for viruses and bacteria through simple yet highly efficient methods, unaffected by optical clarity of the test solutions.

Chapter 9

Conclusions and Future Work

9.1 Conclusions

The present thesis has extended the use of electrode-particle impacts to alternative particle geometries and allowed the probing of a diverse range of phenomena including inter-particle interactions and colloidal mass transport.

First, the electrode-particle impact (EPI) technique can be used to effectively size quasi-spherical nanoparticles through the use of precise direct atom counting information, unobtainable via alternatives such as light scattering or electron microscopy.

Second, the EPI method in conjunction with light scattering methods was shown to be of unique importance in the study of agglomerating/aggregating systems as it allows distinguishing between reversible agglomeration and irreversible aggregation. It was concluded that electrolysis of the impacting particles induces a change in agglomerated/monomeric equilibria, and induces deagglomeration of particles, leading to the detection of monomeric

species.

Third, the theoretical maximization of the entropy of mixing presented in the present work, yielded excellent agreement with the experimentally observed particle distributions for systems of citrate-capped silver and bismuth oxide nanoparticles, where agglomeration takes place. Moreover the entropy of mixing was shown to play a key role in determining the cluster size distribution in weakly interacting systems. The present model complements the electrostatic-based DLVO theory, which dictates the stability criteria for nanoparticulate suspensions, but provides little insight into the cluster-size distribution.

Fourth, the near-wall hindered diffusion has a significant effect on the mass transport of nanoparticles even in convective systems as is found to be crucial in determining the current response for colloidal systems. It was concluded that this hydrodynamic effect puts a limit on the performance of the redox-flow fuel cells and demonstrates how the assumptions valid for molecular systems require re-evaluation for nanoparticulate suspension.

Last it was concluded, that the sensitivity of the EPI method can be significantly enhanced by the use of forced convection. Despite in principle the theoretical limit of detection being a single particle, for practical measurements forced convection allows rapid detection (seconds vs hours in static solution). Lowest to date femtomolar limit of detection was achieved for a system of citrate-capped nanoparticles through use of forced convection and a microelectrode arrays.

9.2 Future Work

The work reported herein provides exciting new pathways for future research. One potential direction of research would be concurrent dark field microscopy and electrochemical measurements. Through the use of such combinations oxidation/reduction of single nanoparticles could be imaged in real-time providing further insights into the kinetics of these processes and the fate of impacting particles. Through continuous optical tracking of the impacting particles near-wall hindered diffusion effects could be evaluated and validated. The development of nanoparticle flow sensor offers a way of detecting industrial and environmental particles in situ with minimal sample preparation and could be potentially extended to more complex species such as viruses and bacteria. This would require further study and testing of such systems in the field, with highly variable ionic strength.

Appendix A

A Thermodynamic View of Agglomeration

The present appendix provides the C++ code used to calculate the most probable cluster particle distribution in the Section 7. The code can be compiled using Microsoft Visual Studio 2015 and run on a personal computer.

```cpp


#include "stdafx.h"

#include <iostream>
using namespace std;
#include "stdafx.h"
#include <iostream>
#include <fstream>
#include <vector>
#include <cmath>
#include <iomanip>
using namespace std;


#include <iostream>



// main
// ========================================

int  main()
{
    double state [10 ];
    double sum = 0;
    double energyperbondval[6] = { -1000 / 6.022e23, -20 / 6.022e23, -50 / 6.022e23, -100 / 6.022e23, -120 / 6.022e23, 100 };
    double energyperbond = 100;
    double gibbs  = 0;
    double gibbsprev   = 0;
    double bonds[10 ] = { 0, 1, 3, 6, 9, 12, 15, 18, 21, 9 };
    double entropy   = 0;
    double enthalpy   = 0;
    double kB = 1.3806488e-23;
    double Avogadro = 6.0221413e+23;
    double entropyprev = 0;
    double numberofspecies    = 0;
    ofstream gibbse("i8nchain200dentropy.txt");
    ofstream gibbs1("i10attractweak20.txt");
    ofstream gibbs2("i10attract50.txt");
    ofstream gibbs3("i10attract100.txt ");
    ofstream gibbs4("i10attract120.txt");
    ofstream gibbs5("i10attract1000f0.txt");
    ofstream gibbs6("i77100oentropy.txt ");


    // parameters
    // ========================================
    int  nMax = 200; // total number of monomers in the system if there was no aggregation







    for  (int  b = 0; b < 6; b++)
    {
        for  (int  i = 0; i < nMax; i++)
        {

            for  (int  i2 = 0; i2 < (0.5*(nMax - i)); i2++)
            {

                for  (int  i3 = 0; i3 < (0.3333*(nMax - i - 2 * i2)); i3++)
                {

                    for  (int  i4 = 0; i4 < (0.25*(nMax - i - 2 * i2 - 3 * i3)); i4++)
                    {

                        for  (int  i5 = 0; i5 < 0.2*((nMax - i - 2 * i2 - 3 * i3 - 4 * i4)); i5++)
                        {

                            for  (int  i6 = 0; i6 < 0.16666*((nMax - i - 2 * i2 - 3 * i3 - 4 * i4 - 5 * i5)); i6++)
                            {
                                for  (int  i7 = 0; i7 < 0.142857*((nMax - i - 2 * i2 - 3 * i3 - 4 * i4 - 5 * i5 - 6 * i6)); i7++)
                                {
                                    for  (int  i8 = 0; i8 < 0.125*((nMax - i - 2 * i2 - 3 * i3 - 4 * i4 - 5 * i5 - 6 * i6 - 7 * i7)); i8++)
                                    {

```

```
                                    for (int i9 = 0; i9 < 0.1111*((nMax - i - 2 * i2 - 3 * i3 - 4 * i4 - 5 * i5 - 6 * i6 - 7 * i7 - 8 * i8)); i9++)
                                    {
                                    for (int i10 = 0; i10 < 0.1*(nMax - i - 2 * i2 - 3 * i3 - 4 * i4 - 5 * i5 - 6 * i6 - 7 * i7 - 8 * i8 - 9 * i9); i10++)
                                    {
                    numberofspecies = i + (i2)+(i3)+(i4)+(i5)+(i6)+(i7)+i8+(i8)+i10;
                                    state[0] = i*1.0;
                                    state[1] = i2*1.0;
                                    state[2] = i3*1.0;
                                    state[3] = i4 *1.0;
                                    state[4] = i5*1.0;
                                    state[5] = i6*1.0;
                                    state[6] = i7*1.0;
                                    state[7] = i8*1.0;
                                    state[8] = i9*1.0;
                                    state[9] = i10*1.0;
                                    for (int m = 0; m < 10; m++)
                                    {
                                        if (state[m] != 0)
                                        {
                                            entropy = entropy - 300.0*kB*numberofspecies * ((state[m] / numberofspecies) * log(state[m] / numberofspecies));
                                            enthalpy = enthalpy + (state[m] * bonds[m] * energyperbondval[b]);
                                        }
                                    }
                                    sum = state[0] + 2 * state[1] + 3 * state[2] + 4 * state[3] + 5 * state[4] + 6 * state[5] + 7 * state[6] + 8 * state[7] + 9 * state[8] + 10 * state[9];

                                    gibbs = enthalpy - entropy;
                                    if ((gibbs < gibbsprev) && (sum>190) && (sum<205))

                                    {
                                    //if (entropy > entropyprev){
                                        gibbsprev = gibbs;
                                        entropyprev = entropy;
                                        if (b == 0){
                                            gibbs1 << setprecision(6) << "\t" << state[0] / numberofspecies << "\t" << state[1] / numberofspecies << "\t" << state[2] / numberofspecies << "\t" << state[3] / numberofspecies << "\t" << state[4] / numberofspecies
                                                << "\t" << state[5] / numberofspecies
                                                << "\t" << state[6] / numberofspecies
                                                << "\t" << state[7] / numberofspecies << "\t" << state[8] / numberofspecies
                                                << "\t" << state[9] / numberofspecies << "\t" << gibbs << "\t" << endl;

                                        }
                                        if (b == 1){
                                            gibbs2 << setprecision(6) << "\t" << state[0] / numberofspecies << "\t" << state[1] / numberofspecies << "\t" << state[2] / numberofspecies << "\t" << state[3] / numberofspecies << "\t" << state[4] / numberofspecies
                                                << "\t" << state[5] / numberofspecies
                                                << "\t" << state[6] / numberofspecies
                                                << "\t" << state[7] / numberofspecies << "\t" << state[8] / numberofspecies
                                                << "\t" << state[9] / numberofspecies << "\t" << gibbs << "\t" << endl;

                                        }
                                        if (b == 2){
                                            gibbs3 << setprecision(6) << "\t" << state[0] / numberofspecies << "\t" << state[1] / numberofspecies << "\t" << state[2] / numberofspecies << "\t" << state[3] / numberofspecies << "\t" << state[4] / numberofspecies
                                                << "\t" << state[5] / numberofspecies
                                                << "\t" << state[6] / numberofspecies
                                                << "\t" << state[7] / numberofspecies << "\t" << state[8] / numberofspecies
                                                << "\t" << state[9] / numberofspecies << "\t" << gibbs << "\t" << endl;


                                        }
                                        if (b == 3){
                                            gibbs4 << setprecision(6) << "\t" << state[0] / numberofspecies << "\t" << state[1] / numberofspecies << "\t" << state[2] / numberofspecies << "\t" << state[3] / numberofspecies << "\t" << state[4] / numberofspecies
                                                << "\t" << state[5] / numberofspecies
                                                << "\t" << state[6] / numberofspecies
                                                << "\t" << state[7] / numberofspecies << "\t" << state[8] / numberofspecies
                                                << "\t" << state[9] / numberofspecies
```

```
    << "\t" << gibbs << "\t" << endl;
143
144
145                                             }
146                                             if (b == 4){
147                                                 gibbs5 << setprecision(6) << "\t" << state[0
    ] / numberofspecies << "\t" << state[1] / numberofspecies << "\t" << state[2] /
    numberofspecies << "\t" << state[3] / numberofspecies << "\t" << state[4] / numberofspecies
148                                                         << "\t" << state[5] / numberofspecies
149                                                         << "\t" << state[6] / numberofspecies
150                                                         << "\t" << state[7] / numberofspecies
    << "\t" << state[8] / numberofspecies
151                                                         << "\t" << state[9] / numberofspecies
    << "\t" << gibbs << "\t" << endl;
152
153                                             }
154                                             if (b == 5){
155                                                 gibbs6 << setprecision(6) << "\t" << state[0
    ] / numberofspecies << "\t" << state[1] / numberofspecies << "\t" << state[2] /
    numberofspecies << "\t" << state[3] / numberofspecies << "\t" << state[4] / numberofspecies
156                                                         << "\t" << state[5] / numberofspecies
157                                                         << "\t" << state[6] / numberofspecies
158                                                         << "\t" << state[7] / numberofspecies
    << "\t" << state[8] / numberofspecies
159                                                         << "\t" << state[9] / numberofspecies
    << "\t" << gibbs << "\t" << endl;
160
161                                             }
162
163                                         }
164                                         sum = 0;
165                                         entropy = 0;
166                                         enthalpy = 0;
167                                         gibbs = 0;
168                                         numberofspecies = 0;
169                                         for (int j = 0; j < 10; j++)
170                                         {
171                                             state[j] = 0;
172                                         }
173                                     }
174
175                                 }
176
177                                 }
178                                 }
179                                 }
180                                     }
181
182                             }
183                         }
184                     }
185
186
187
188
189
190
191
192
193
194
195
196
197                 }
198                 gibbsprev = 10000;
199             }
200             return 0;
201         }
202
203
204
```

Appendix B

Flow cell schematics

The present appendix shows the technical drawings for the flow cell discussed in Chapter 8 with the key dimensions drawn to scale. The flow cell was designed in collaboration with Mr. (now Dr.) Thomas R. Bartlett (University of Oxford, Department of Chemistry) and manufactured by Mr. Peter Fair (University of Oxford, Physical and Theoretical Chemistry Workshop).

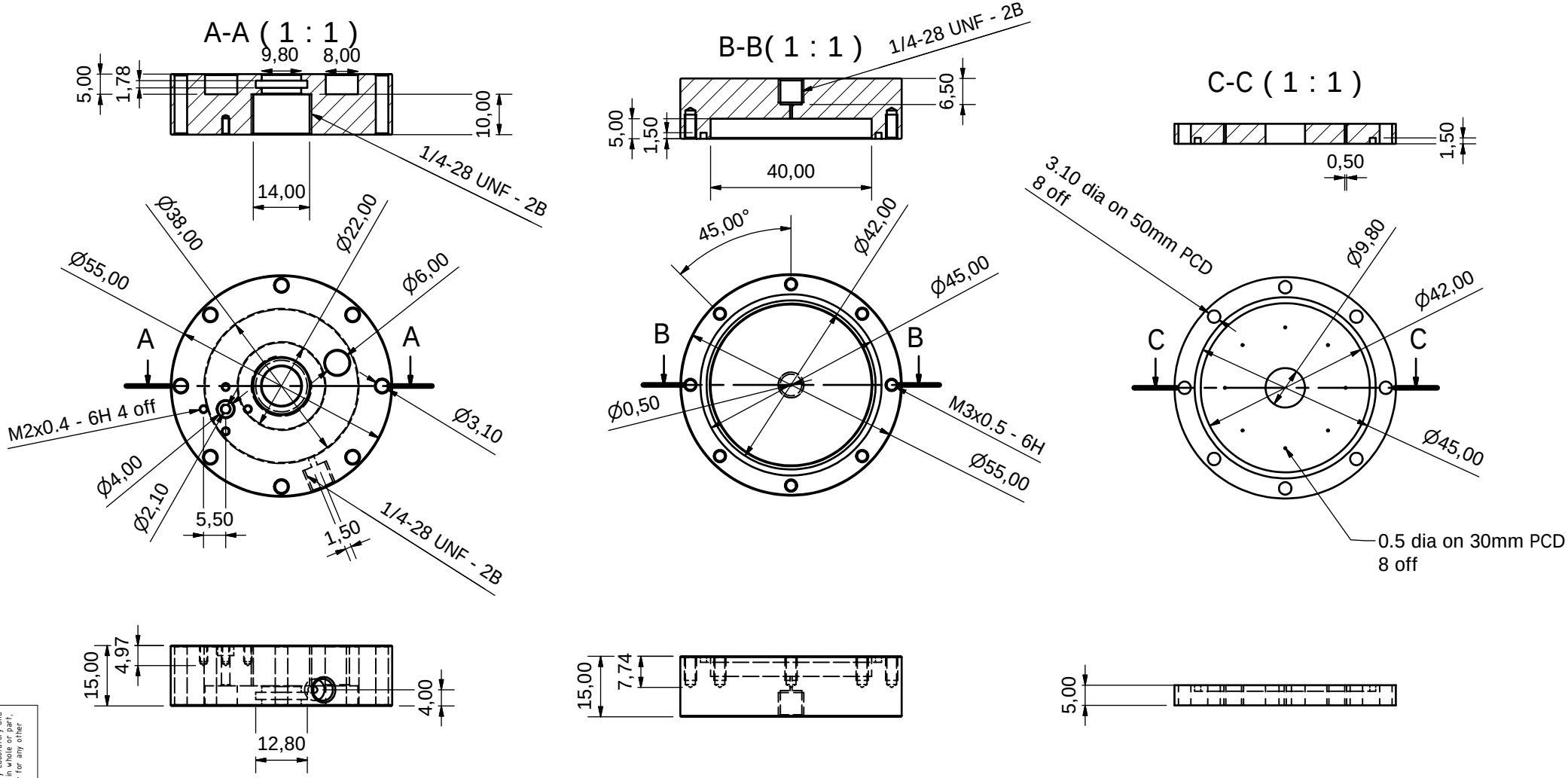

CELL BASE

CELL TOP

FLOW PLATE

Revision	Date	Issue

Dimensions in millimetres unless otherwise stated

Remove all burrs and sharp edges

Job Title: Radial Flow Cell

Part Description:BASE, FLOW PLATE & TOP

Material: PEEK | Qty:ONE EACH

Finish:N/A

Research Worker:Tom Bartlett | Group:RGC

PTCL WORKSHOP

Tolerances (unless otherwise stated)
Dim'n 0 ± 1mm
Dim'n 0.0 ± 0.1mm
Dim'n 0.00 ± 0.05mm
Angle ± 0° 30'
Surface Finish 1.6u

0 50 millimetres full scale 50

SCALE | A3

Date: 11/5/16 | Drawn By: PF

File:

Mechanical Workshop
Physical & Theoretical Chemistry Dept
Oxford University
South Parks Road
Oxford. OX1 3QZ.
Tel. 01865 275441, Fax 01865 275410

Contact: peter.fair@chem.ox.ac.uk

Path: WS12_Z:\Pete\

Assembly Section

B-B (1 : 1)

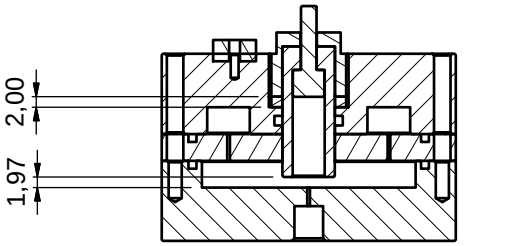

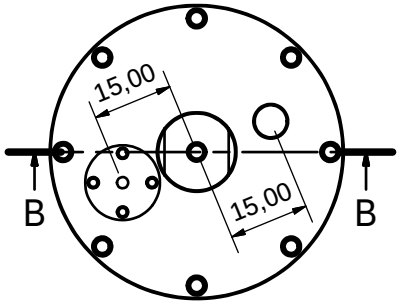

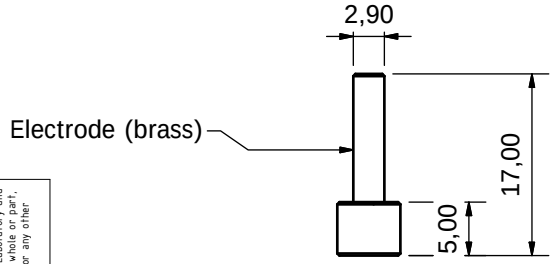

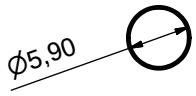

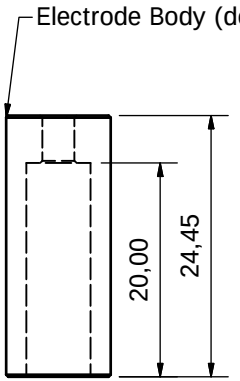

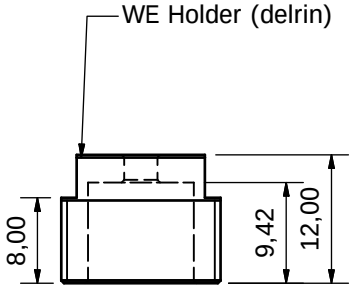

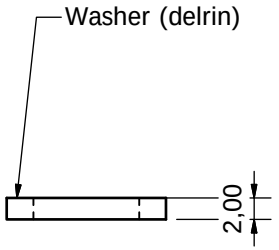

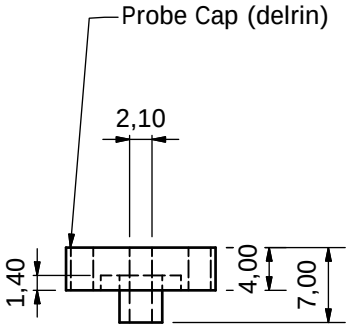

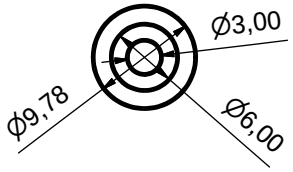

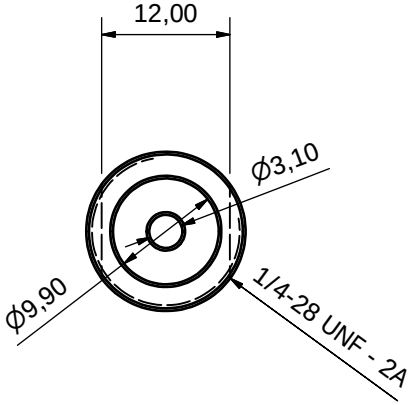

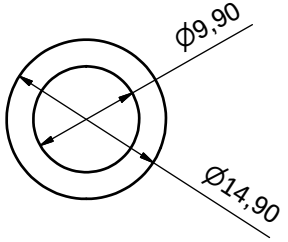

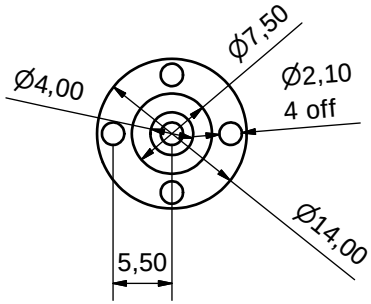

Revision	Date	Issue

Dimensions in millimetres unless otherwise stated

Remove all burrs and sharp edges

Job Title: Radial Flow Cell

Part Description: Assembly Section & Component Parts

Material: See Above | Qty:One

Finish:N/A

Research Worker:Tom Bartlett | Group:RGC

PTCL WORKSHOP

Tolerances (unless otherwise stated)

Dim'n 0 ± 1mm
Dim'n 0.0 ± 0.1mm
Dim'n 0.00 ± 0.05mm

Angle ± 0° 30'
Surface Finish 1.6u

0 50 millimetres full scale 50

SCALE | A3

Date: 11/5/16 | Drawn By: PF

File:

Mechanical Workshop
Physical & Theoretical Chemistry Dept
Oxford University
South Parks Road
Oxford. OX1 3QZ.
Tel. 01865 275441, Fax 01865 275410

Contact: peter.fair@chem.ox.ac.uk

Path: WS12_Z:\Pete\

Bibliography

[1] R. G. Compton and C. E. Banks, *Understanding Voltammetry*. Imperial College Press, 2nd ed., 2010.

[2] A. Bard and L. Faulkner, *Electrochemical methods: fundamentals and applications*. New York: Wiley, 2nd ed., 2001.

[3] M. D. Koretsky, *Engineering and Chemical Thermodynamics*. Wiley, 2nd ed., 2013.

[4] P. S. Nobel *Physicochem. Environ. Plant Physiol.*, vol. 2, pp. 545–553, 2009.

[5] C. G. Zoski, *Handbook of electrochemistry*. Elsevier, 2007.

[6] M. D. Archer, "Genesis of the Nernst Equation," in *Electrochem. Past Present*, pp. 115–126, 1989.

[7] M. A. Wilkinson A, *Compendium of Chemical Terminology, 2nd ed. (the "Gold Book")*. IUPAC, 1997.

[8] D. C. Grahame *Chem. Rev.*, vol. 41, pp. 441–501, 1947.

[9] J. Albery, *Electrode Kinetics*. Oxford University Press, 1975.

[10] K. B. Oldham *J. Electroanal. Chem.*, vol. 613, pp. 131–138, 2008.

[11] R. Kant and M. B. Singh *Phys. Rev. E - Stat. Nonlinear, Soft Matter Phys.*, vol. 88, 2013.

[12] E. Gileadi, *Physical Electrochemistry.* Wiley, 2011.

[13] P. Atkins and J. D. Paula, *Atkins' Physical Chemistry.* Oxford University Press, 9th ed., 2009.

[14] L. M. Torres, A. F. Gil, L. Galicia, and I. González *J. Chem. Educ.*, vol. 73, p. 808, 1996.

[15] M. Z. Bazant *Acc. Chem. Res.*, vol. 46, pp. 1144–1160, 2013.

[16] R. Guidelli, R. G. Compton, J. M. Feliu, E. Gileadi, J. Lipkowski, W. Schmickler, and S. Trasatti *Pure Appl. Chem.*, vol. 86, pp. 245–258, 2014.

[17] R. Guidelli, R. G. Compton, J. M. Feliu, E. Gileadi, J. Lipkowski, W. Schmickler, and S. Trasatti *Pure Appl. Chem.*, vol. 86, pp. 259–262, 2014.

[18] E. Kätelhön and R. G. Compton *Chem. Sci.*, vol. 5, pp. 4592–4598, 2014.

[19] J. Philibert, "Adolf Fick and diffusion equations," in *Diffus. Solids - Past, Present Futur.*, vol. 249, pp. 1–6, 2006.

[20] K. Krynicki, C. D. Green, and D. W. Sawyer *Faraday Discuss. Chem. Soc.*, vol. 66, p. 199, 1978.

[21] E. J. F. Dickinson, J. G. Limon-Petersen, N. V. Rees, and R. G. Compton *J. Phys. Chem. C*, vol. 113, pp. 11157–11171, 2009.

[22] E. J. Dickinson and R. G. Compton *J. Electroanal. Chem.*, vol. 661, pp. 198–212, 2011.

[23] J. O. Bockris and B. E. Conway, eds., *Modern Aspects of Electrochemistry No. 6*. Boston, MA: Springer US, 1971.

[24] K. Ngamchuea, S. Eloul, K. Tschulik, and R. G. Compton *Anal. Chem.*, vol. 87, pp. 7226–7234, 2015.

[25] Y. V. Pleskov and V. Y. Filinovskii, *The Rotating Disk Electrode*. New York: Consultants Bureau, 2nd ed., 1976.

[26] J. A. Cooper and R. G. Compton *Electroanalysis*, vol. 10, pp. 141–155, 1998.

[27] A. M. Bond *Analyst*, vol. 119, p. 1R, 1994.

[28] A. R. Halpern and R. M. Corn *ACS Nano*, vol. 7, pp. 1755–1762, 2013.

[29] Y. Li, L. Huang, M. Zhong, Z. Wei, and J. Li *Adv. Mater. Technol.*, vol. 1, pp. 1600001–1600008, 2016.

[30] S. Mu, X. Wang, Y.-T. Li, Y. Wang, D.-W. Li, and Y.-T. Long *Analyst*, vol. 137, p. 3220, 2012.

[31] I. Fried and P. J. Elving *Anal. Chem.*, vol. 37, pp. 803–806, 1965.

[32] C. E. Banks, A. O. Simm, R. Bowler, K. Dawes, and R. G. Compton *Anal. Chem.*, vol. 77, pp. 1928–30, 2005.

[33] V. C. Patel, W. Rodi, and G. Scheuerer *AIAA J.*, vol. 23, pp. 1308–1319, 1985.

[34] T. V. Kármán *ZAMM - J. Appl. Math. Mech. / Zeitschrift für Angew. Math. und Mech.*, vol. 1, pp. 233–252, 1921.

[35] W. Cochran *Proc. Camb. Philo. Soc.*, vol. 30, pp. 365–375, 1934.

[36] W. J. Albery and S. Bruckenstein *J. Electroanal. Chem. Interfacial Electrochem.*, vol. 144, pp. 105–112, 1983.

[37] B. Levich *Acta Physicochim. U.R.S.S.*, vol. 17, p. 257, 1942.

[38] V. Levich *Dokl. Akad. Nauk SSSR*, vol. 67, pp. 309–312, 1949.

[39] L. Challier, R. Miranda-Castro, D. Marchal, V. Noël, F. Mavré, and B. Limoges *J. Am. Chem. Soc.*, vol. 135, pp. 14215–14228, 2013.

[40] H. Gunasingham and B. Fleet *Anal. Chem.*, vol. 55, pp. 1409–1414, 1983.

[41] R. Compton, A. Fisher, M. Latham, R. Wellington, C. Brett, and A. Brett *J. Appl. Electrochem.*, vol. 23, pp. 98–102, 1993.

[42] M. G. Banus *Science*, vol. 93, pp. 601–602, 1941.

[43] F. Cottrell *Z. Physilk. Chem.*, vol. 42, p. 385, 1902.

[44] R. J. Forster *Chem. Soc. Rev.*, vol. 23, p. 289, 1994.

[45] D. Shoup and A. Szabo *J. Electroanal. Chem. Interfacial Electrochem.*, vol. 140, pp. 237–245, 1982.

[46] A. Szabo, D. K. Cope, D. E. Tallman, P. M. Kovach, and R. Wightman *J. Electroanal. Chem. Interfacial Electrochem.*, vol. 217, pp. 417–423, 1987.

[47] J. Ellison, C. Batchelor-McAuley, K. Tschulik, and R. G. Compton *Sensors Actuators B Chem.*, vol. 200, pp. 47–52, 2014.

[48] H. Matsuda and Y. Ayabe *Bull. Chem. Soc. Jpn.*, vol. 28, pp. 422–428, 1955.

[49] H. Matsuda and Y. Ayabe *Bull. Chem. Soc. Jpn.*, vol. 29, pp. 134–140, 1956.

[50] A. M. Bond, K. B. Oldham, and C. G. Zoski *J. Electroanal. Chem. Interfacial Electrochem.*, vol. 245, pp. 71–104, 1988.

[51] T. J. Davies, C. E. Banks, and R. G. Compton *J. Solid State Electrochem.*, vol. 9, pp. 797–808, 2005.

[52] S. Fletcher and M. D. Horne *Electrochem. Commun.*, vol. 1, pp. 502–512, 1999.

[53] N. Godino, X. Borrisee, F. X. Munoz, F. J. del Campo, and R. G. Compton *J. Phys. Chem. C*, vol. 113, pp. 11119–11125, 2009.

[54] Y. Xia, H. Yang, and C. T. Campbell *Acc. Chem. Res.*, vol. 46, pp. 1671–1672, 2013.

[55] K. Shimizu, K. Tschulik, and R. G. Compton *Chem. Sci.*, vol. 7, pp. 1408–1414, 2016.

[56] L. Tian, X. Yan, and X. Chen *ACS Catal.*, vol. 6, pp. 5441–5448, 2016.

[57] R. Tantra, *Nanomaterial Characterization : An Introduction*. Wiley VCH Verlag GmbH & Co. KGaA, 2016.

[58] W. J. Stark *Angew. Chemie Int. Ed.*, vol. 50, pp. 1242–1258, 2011.

[59] L. de Broglie *Found. Phys.*, vol. 1, pp. 5–15, 1970.

[60] D. B. Williams and C. B. Carter, *Transmission Electron Microscopy: A Textbook for Materials Science*, vol. V1-V4. 2009.

[61] S.-J. Lim and C.-H. Lee *Int. Conf. Smart Manuf. Appl.*, pp. 15–18, 2008.

[62] W. Zhou, R. P. Apkarian, and Z. L. Wang *Scanning Microsc. Nanotechnol.*, pp. 1–40, 2007.

[63] B. Faust, *Modern Chemical Techniques*. RSC Publishing, 1997.

[64] B. J. Plowman, N. P. Young, C. Batchelor-McAuley, and R. G. Compton *Angew. Chemie Int. Ed.*, vol. 55, pp. 7002–7005, 2016.

[65] B. J. Plowman, B. Sidhureddy, S. V. Sokolov, N. P. Young, A. Chen, and R. G. Compton *ChemElectroChem*, vol. 3, pp. 1186–1186, 2016.

[66] T. R. Bartlett, S. V. Sokolov, B. J. Plowman, N. P. Young, and R. G. Compton *Nanoscale*, vol. 8, pp. 16177–16181, 2016.

[67] B. Michen, C. Geers, D. Vanhecke, C. Endes, B. Rothen-Rutishauser, S. Balog, and A. Petri-Fink *Sci. Rep.*, vol. 5, p. 9793, 2015.

[68] J. B. Wagner, F. Cavalca, C. D. Damsgaard, L. D. Duchstein, and T. W. Hansen *Micron*, vol. 43, pp. 1169–1175, 2012.

[69] H.-G. Liao and H. Zheng *Annu. Rev. Phys. Chem.*, vol. 67, pp. 719–747, 2016.

[70] X. Fan, W. Zheng, and D. J. Singh *Light Sci. Appl.*, vol. 3, p. 179, 2014.

[71] H. A. Lorentz, "Clerk Maxwell's Electromagnetic Theory," in *Collect. Pap.*, pp. 353–366, Dordrecht: Springer Netherlands, 1935.

[72] G. Mie *Ann. Phys.*, vol. 330, pp. 377–445, 1908.

[73] M. Born and E. Wolf, *Principles of Optics: Electromagnetic Theory of Propagation, Interference and Diffraction of Light*. 1999.

[74] G. Papavassiliou *Prog. Solid State Chem.*, vol. 12, pp. 185–271, 1979.

[75] V. Amendola and M. Meneghetti *J. Phys. Chem. C*, vol. 113, pp. 4277–4285, 2009.

[76] W. Haiss, N. T. K. Thanh, J. Aveyard, and D. G. Fernig *Anal. Chem.*, vol. 79, pp. 4215–4221, 2007.

[77] J. Cao, T. Sun, and K. T. Grattan *Sensors Actuators B Chem.*, vol. 195, pp. 332–351, 2014.

[78] P. J. Vikesland, R. L. Rebodos, J. Y. Bottero, J. Rose, and A. Masion *Environ. Sci. Nano*, vol. 3, pp. 567–577, 2016.

[79] A. Einstein, *Investigations on the Theory of the Brownian Movement (Republication)*. Dover Publications, 1956.

[80] W. Sutherland *Philos. Mag.*, vol. 9, pp. 781–785, 1905.

[81] V. Filipe, A. Hawe, and W. Jiskoot *Pharm. Res.*, vol. 27, pp. 796–810, 2010.

[82] S. V. Sokolov, K. Tschulik, C. Batchelor-McAuley, K. Jurkschat, and R. G. Compton *Anal. Chem.*, vol. 87, pp. 10033–10039, 2015.

[83] V. Sokolova, A.-K. Ludwig, S. Hornung, O. Rotan, P. A. Horn, M. Epple, and B. Giebel *Colloids Surfaces B Biointerfaces*, vol. 87, pp. 146–150, 2011.

[84] K. Schmitz, *An Introduction to Dynamic Light Scattering by Macromolecules*, vol. 24. Elsevier, 2006.

[85] W. I. Goldburg *Am. J. Phys.*, vol. 67, pp. 1152–1160, 1999.

[86] B. Chu, "Dynamic Light Scattering," in *Soft Matter Charact.*, pp. 335–372, Dordrecht: Springer Netherlands, 2008.

[87] R. Pecora *J. Nanoparticle Res.*, vol. 2, pp. 123–131, 2000.

[88] R. B. Grubbs *Polym. Rev.*, vol. 47, pp. 197–215, 2007.

[89] C. Lourenco, M. Teixeira, S. Simões, and R. Gaspar *Int. J. Pharm.*, vol. 138, pp. 1–12, 1996.

[90] A. R. Studart, E. Amstad, and L. J. Gauckler *Langmuir*, vol. 23, pp. 1081–1090, 2007.

[91] R. J. Hunter, *Zeta Potential in Colloid Science : Principles and Applications*. Elsevier B.V., 1981.

[92] V. Tandon, S. K. Bhagavatula, W. C. Nelson, and B. J. Kirby *Electrophoresis*, vol. 29, pp. 1092–1101, 2008.

[93] F. W. Campbell and R. G. Compton *Anal. Bioanal. Chem.*, vol. 396, pp. 241–259, 2010.

[94] O. S. Ivanova and F. P. Zamborini *J. Am. Chem. Soc.*, vol. 132, pp. 70–2, 2010.

[95] S. J. Cloake, H. S. Toh, P. T. Lee, C. Salter, C. Johnston, and R. G. Compton *ChemistryOpen*, vol. 4, pp. 22–26, 2015.

[96] C. Batchelor-McAuley, E. Kätelhön, E. O. Barnes, R. G. Compton, E. Laborda, and A. Molina *ChemistryOpen*, vol. 4, pp. 224–260, 2015.

[97] A. Henglein *J. Phys. Chem.*, vol. 97, pp. 5457–5471, 1993.

[98] S. E. Ward Jones, F. W. Campbell, R. Baron, L. Xiao, and R. G. Compton *J. Phys. Chem. C*, vol. 112, pp. 17820–17827, 2008.

[99] S. E. Ward Jones, F. G. Chevallier, C. A. Paddon, and R. G. Compton *Anal. Chem.*, vol. 79, pp. 4110–4119, 2007.

[100] W. J. Plieth *J. Phys. Chem.*, vol. 86, pp. 3166–3170, 1982.

[101] M. Szymanski, A. P. F. Turner, and R. Porter *Electroanalysis*, vol. 22, pp. 191–198, 2010.

[102] N. Wang, T. Tong, M. Xie, and J.-F. Gaillard *Nanotechnology*, vol. 27, p. 324001, 2016.

[103] K. Micka *Collect. Czechoslov. Chem. Commun.*, vol. 21, pp. 647–651, 1956.

[104] G. Moller *Chimia (Aarau).*, vol. 25, p. 29, 1971.

[105] A. Holland and J. Sawers *Photogr. Sci. Eng.*, vol. 17, pp. 295–298, 1973.

[106] A. Holland and A. Feinerman *J. Appl. Photogr. Eng.*, vol. 8, pp. 165–167, 1982.

[107] M. Heyrovsky and J. Jirkovsky *Langmuir*, vol. 11, pp. 4288–4292, 1995.

[108] M. Heyrovsky, J. Jirkovsky, and M. Struplova-Bartackova *Langmuir*, vol. 11, pp. 4300–4308, 1995.

[109] M. Heyrovsky, J. Jirkovsky, and M. Struplova-Bartackova *Langmuir*, vol. 11, pp. 4309–4312, 1995.

[110] M. Heyrovsky, J. Jirkovsky, and B. R. Mueller *Langmuir*, vol. 11, pp. 4293–4299, 1995.

[111] X. Xiao and A. J. Bard *J. Am. Chem. Soc.*, vol. 129, pp. 9610–9612, 2007.

[112] S. V. Sokolov, S. Eloul, E. Kätelhön, C. Batchelor-McAuley, and R. G. Compton *Phys. Chem. Chem. Phys.*, vol. 19, pp. 28–43, 2017.

[113] Y.-G. Zhou, N. V. Rees, and R. G. Compton *Angew. Chemie Int. Ed.*, vol. 50, pp. 4219–4221, 2011.

[114] B. Haddou, N. V. Rees, and R. G. Compton *Phys. Chem. Chem. Phys.*, vol. 14, p. 13612, 2012.

[115] Y.-G. Zhou, N. V. Rees, and R. G. Compton *Phys. Chem. Chem. Phys.*, vol. 15, pp. 761–3, 2013.

[116] Y.-G. Zhou, N. V. Rees, J. Pillay, R. Tshikhudo, S. Vilakazi, and R. G. Compton *Chem. Commun.*, vol. 48, pp. 224–226, 2012.

[117] K. Tschulik, B. Haddou, D. Omanović, N. V. Rees, and R. G. Compton *Nano Res.*, vol. 6, pp. 836–841, 2013.

[118] W. Cheng, X.-F. Zhou, and R. G. Compton *Angew. Chem. Int. Ed. Engl.*, vol. 52, pp. 12980–2, 2013.

[119] E. E. L. Tanner, C. Batchelor-McAuley, and R. G. Compton *J. Phys. Chem. C*, vol. 120, pp. 1959–1965, 2016.

[120] E. J. E. Stuart, Y.-G. Zhou, N. V. Rees, and R. G. Compton *RSC Adv.*, vol. 2, p. 6879, 2012.

[121] J. Poon, C. Batchelor-McAuley, K. Tschulik, and R. G. Compton *Chem. Sci.*, vol. 6, pp. 2869–2876, 2015.

[122] B. M. Quinn, P. G. van't Hof, and S. G. Lemay *J. Am. Chem. Soc.*, vol. 126, pp. 8360–8361, 2004.

[123] J. E. Dick, C. Renault, and A. J. Bard *J. Am. Chem. Soc.*, vol. 137, pp. 8376–8379, 2015.

[124] P. H. Robbs and N. V. Rees *Phys. Chem. Chem. Phys.*, vol. 35, pp. 583–592, 2016.

[125] W. Cheng and R. G. Compton *TrAC Trends Anal. Chem.*, vol. 58, pp. 79–89, 2014.

[126] C. Batchelor-McAuley, J. Ellison, K. Tschulik, P. L. Hurst, R. Boldt, and R. G. Compton *Analyst*, vol. 140, pp. 5048–5054, 2015.

[127] S. V. Sokolov, C. Batchelor-McAuley, K. Tschulik, S. Fletcher, and R. G. Compton *Chem. - A Eur. J.*, vol. 21, pp. 10741–10746, 2015.

[128] W. J. Stark, P. R. Stoessel, W. Wohlleben, and A. Hafner *Chem. Soc. Rev.*, vol. 44, pp. 5793–5805, 2015.

[129] M. M. Shahjamali, M. Salvador, M. Bosman, D. S. Ginger, and C. Xue *J. Phys. Chem. C*, vol. 118, pp. 12459–12468, 2014.

[130] D. Uzio and G. Berhault *Catal. Rev.*, vol. 52, pp. 106–131, 2010.

[131] M. Atiyah and P. Sutcliffe *Milan J. Math.*, vol. 71, pp. 33–58, 2003.

[132] S. Alvarez *Dalt. Trans.*, pp. 2209–2233, 2005.

[133] J. C. Lees, J. Ellison, C. Batchelor-McAuley, K. Tschulik, C. Damm, D. Omanovic, and R. G. Compton *ChemPhysChem*, vol. 14, pp. 3895–3897, 2013.

[134] C. S. Lim, S. M. Tan, Z. Sofer, and M. Pumera *ACS Nano*, vol. 9, pp. 8474–8483, 2015.

[135] T. R. Bartlett, S. V. Sokolov, J. Holter, N. Young, and R. G. Compton *Chem. Eur. J.*, vol. 22, pp. 7408–7414, 2016.

[136] P. L. Stewart *WIREs Nanomed. Nanobiotechnol*, vol. 9, pp. 1417–1433, 2017.

[137] E. A. Ring and N. de Jonge *Micron*, vol. 43, pp. 1078–1084, 2012.

[138] J. Liu, Z. Wang, A. Sheng, F. Liu, F. Qin, and Z. L. Wang *Environ. Sci. Technol.*, vol. 50, pp. 5606–5613, 2016.

[139] T. Prathna, N. Chandrasekaran, and A. Mukherjee *Colloids Surfaces A Physicochem. Eng. Asp.*, vol. 390, pp. 216–224, 2011.

[140] A. E. James and J. D. Driskell *Analyst*, vol. 138, p. 1212, 2013.

[141] D. T. Yang, X. Lu, Y. Fan, and R. M. Murphy *AIChE J.*, vol. 60, pp. 1236–1244, 2014.

[142] X. Li and J. J. Lenhart *Environ. Sci. Technol.*, vol. 46, pp. 5378–5386, 2012.

[143] R. A. French, A. R. Jacobson, B. Kim, S. L. Isley, R. L. Penn, and P. C. Baveye *Environ. Sci. Technol.*, vol. 43, pp. 1354–1359, 2009.

[144] B. Ninham *Adv. Colloid Interface Sci.*, vol. 83, pp. 1–17, 1999.

[145] J. Lyklema, H. P. Van Leeuwen, and M. Minor *Adv. Colloid Interface Sci.*, vol. 83, pp. 33–69, 1999.

[146] D. Thomas, S. Judd, and N. Fawcett *Water Res.*, vol. 33, pp. 1579–1592, 1999.

[147] A. Sivakumar, B. Murugesan, A. Loganathan, and P. Sivakumar *J. Taiwan Inst. Chem. Eng.*, vol. 45, pp. 2300–2306, 2014.

[148] G. N. J. Tytgat *Digestion*, vol. 37, pp. 31–41, 1987.

[149] B. A. Baumert *J. Supercond.*, vol. 8, pp. 175–181, 1995.

[150] A. Espinosa, M. San José, M. Tascón, M. Vászquez, and P. Sánchez Batanero *Electrochim. Acta*, vol. 36, pp. 1561–1571, 1991.

[151] J. M. Kahk, N. V. Rees, J. Pillay, R. Tshikhudo, S. Vilakazi, and R. G. Compton *Nano Today*, vol. 7, pp. 174–179, 2012.

[152] S. V. Sokolov, E. Kätelhön, and R. G. Compton *J. Phys. Chem. C*, vol. 119, pp. 25093–25099, 2015.

[153] E. Kätelhön, S. V. Sokolov, T. R. Bartlett, and R. G. Compton *ChemPhysChem*, vol. 18, pp. 51–54, 2017.

[154] B. Derjaguin and L. Landau *Prog. Surf. Sci.*, vol. 43, pp. 30–59, 1993.

[155] E. J. W. Verway and J. T. G. Overbeek *J. Phys. Colloid Chem.*, vol. 51, pp. 631–636, 1948.

[156] E. M. V. Hoek and G. K. Agarwal *J. Colloid Interface Sci.*, vol. 298, pp. 50–58, 2006.

[157] S. Torkzaban, S. A. Bradford, and S. L. Walker *Langmuir*, vol. 23, pp. 9652–60, 2007.

[158] C.-J. Shih, S. Lin, M. S. Strano, and D. Blankschtein *J. Am. Chem. Soc.*, vol. 132, pp. 14638–14648, 2010.

[159] M. Baaden and S. J. Marrink *Curr. Opin. Struct. Biol.*, vol. 23, pp. 878–886, 2013.

[160] N. J. Kapur, *Maximum-entropy Models in Science and Engineering.* Wiley Eastern Limited, 1989.

[161] A. Zellner, "Bayesian Methods and Entropy in Economics and Econometrics," in *Maximum Entropy and Bayesian Methods*, pp. 17–31, Dordrecht: Springer Netherlands, 1991.

[162] E. Jaynes *Proc. IEEE*, vol. 70, pp. 1939–1982, 1982.

[163] E. Limpert, W. A. Stahel, and M. Abbt *Bioscience*, vol. 51, p. 341, 2001.

[164] S. Pressé, K. Ghosh, J. Lee, and K. A. Dill *Rev. Mod. Phys.*, vol. 85, pp. 1115–1141, 2013.

[165] J. R. Banavar, M. Kohmoto, and J. Roberts *Phys. Rev. A*, vol. 33, pp. 2065–2067, 1986.

[166] D. Kincaid and W. Cheney, "Numerical Analysis: Mathematics of Scientific Computing," 2002.

[167] A. L. Koch *J. Theor. Biol.*, vol. 12, pp. 276–290, 1966.

[168] A. L. Koch *J. Theor. Biol.*, vol. 23, pp. 251–268, 1969.

[169] J. Labille and J. Brant *Nanomedicine*, vol. 5, pp. 985–998, 2010.

[170] I. N. Bronstein, K. A. Semendjajew, G. Musiol, and H. Mühlig, *Taschenbuch der Mathematik*, vol. 23. 2008.

[171] D. Bertsekas, *Constrained Optimization and Lagrange Multiplier Methods*. Boston: Academic Press, 1982.

[172] J. Verbeke and R. Cools *Int. J. Math. Educ. Sci. Technol.*, vol. 26, pp. 177–193, 1995.

[173] S. V. Sokolov, E. Kätelhön, and R. G. Compton *J. Phys. Chem. C*, vol. 120, pp. 10629–10640, 2016.

[174] M. Beaudin, H. Zareipour, A. Schellenberglabe, and W. Rosehart *Energy Sustain. Dev.*, vol. 14, pp. 302–314, 2010.

[175] I. Dincer *Renew. Sustain. Energy Rev.*, vol. 4, pp. 157–175, 2000.

[176] Z. Yang, J. Zhang, M. C. W. Kintner-Meyer, X. Lu, D. Choi, J. P. Lemmon, and J. Liu *Chem. Rev.*, vol. 111, pp. 3577–613, 2011.

[177] C. Ponce de León, A. Frías-Ferrer, J. González-García, D. Szánto, and F. Walsh *J. Power Sources*, vol. 160, pp. 716–732, 2006.

[178] S. Sen, E. V. Timofeeva, C. J. Pelliccione, J. P. Katsoudas, D. Singh, and C. U. Segre *ECS Meet. Abstr.*, vol. MA2015-01, p. 224, 2015.

[179] S. Sen, E. Moazzen, S. Aryal, C. U. Segre, and E. V. Timofeeva *J. Nanoparticle Res.*, vol. 17, pp. 437–445, 2015.

[180] K.-M. Yao, M. T. Habibian, and C. R. O'Melia *Environ. Sci. Technol.*, vol. 5, pp. 1105–1112, 1971.

[181] Y. Tian, B. Gao, C. Silvera-Batista, and K. J. Ziegler *J. Nanoparticle Res.*, vol. 12, pp. 2371–2380, 2010.

[182] R. W. Harvey and S. P. Garabedian *Environ. Sci. Technol.*, vol. 25, pp. 178–185, 1991.

[183] H. Ma and W. P. Johnson *Langmuir*, vol. 26, pp. 1680–7, 2010.

[184] H. B. Eral, J. M. Oh, D. van den Ende, F. Mugele, and M. H. G. Duits *Langmuir*, vol. 26, pp. 16722–9, 2010.

[185] N. Tufenkji and M. Elimelech *Environ. Sci. Technol.*, vol. 38, pp. 529–536, 2004.

[186] W. Xing, G. Yin, and J. Zhang, *Rotating Electrode Methods and Oxygen Reduction Electrocatalysts*. 2014.

[187] R. G. Compton, M. E. Laing, D. Mason, R. J. Northing, and P. R. Unwin *Proc. R. Soc. A Math. Phys. Eng. Sci.*, vol. 418, pp. 113–154, 1988.

[188] A. Riese, D. Banham, S. Ye, and X. Sun *J. Electrochem. Soc.*, vol. 162, pp. F783–F788, 2015.

[189] L. Wang, X. Zhao, Y. Lu, M. Xu, D. Zhang, R. S. Ruoff, K. J. Stevenson, and J. B. Goodenough *J. Electrochem. Soc.*, vol. 158, pp. A1379–A1382, 2011.

[190] C. O. Laoire, S. Mukerjee, K. M. Abraham, E. J. Plichta, and M. A. Hendrickson *J. Phys. Chem. C*, vol. 113, pp. 20127–20134, 2009.

[191] J. Dolinska, M. Jonsson-Niedziolka, V. Sashuk, and M. Opallo *Electrochem. Commun.*, vol. 37, pp. 100–103, 2013.

[192] J. J. P. Roberts, J. A. Westgard, L. M. Cooper, and R. W. Murray *J. Am. Chem. Soc.*, vol. 136, pp. 10783–9, 2014.

[193] J. Dolinska, P. Kannan, J. W. Sobczak, and M. Opallo *ChemElectroChem*, vol. 2, pp. 1199–1205, 2015.

[194] E. O. Barnes, Y.-G. Zhou, N. V. Rees, and R. G. Compton *J. Electroanal. Chem.*, vol. 691, pp. 28–34, 2013.

[195] M. Yoda and Y. Kazoe *Phys. Fluids*, vol. 23, pp. 111301–111309, 2011.

[196] H. Brenner *Chem. Eng. Sci.*, vol. 16, pp. 242–251, 1961.

[197] E. Kätelhön, W. Cheng, C. Batchelor-McAuley, K. Tschulik, and R. G. Compton *ChemElectroChem*, vol. 1, pp. 1057–1062, 2014.

[198] K. D. Kihm, A. Banerjee, C. K. Choi, and T. Takagi *Exp. Fluids*, vol. 37, pp. 811–824, 2004.

[199] A. Pierres, A. M. Benoliel, C. Zhu, and P. Bongrand *Biophys. J.*, vol. 81, pp. 25–42, 2001.

[200] M. Elimelech *Sep. Technol.*, vol. 4, pp. 186–212, 1994.

[201] M. A. Bevan and D. C. Prieve *J. Chem. Phys.*, vol. 113, pp. 1228–1236, 2000.

[202] P. J. Sonneveld, W. Visscher, and E. Barendrecht *J. Appl. Electrochem.*, vol. 20, pp. 563–574, 1990.

[203] T. Dabroś and J. Czarnecki *J. Colloid Interface Sci.*, vol. 53, pp. 335–336, 1975.

[204] M. Marie de Ficquelmont-Loizos *J. Electrochem. Soc.*, vol. 135, pp. 626–634, 1988.

[205] C. Deslouis, A. Ezzidi, and B. Tribollet *J. Appl. Electrochem.*, vol. 21, pp. 1081–1086, 1991.

[206] *Transient Techniques in Electrochemistry*. Springer Science & Business Media, 2012.

[207] A. M. Bond, *Broadening Electrochemical Horizons: Principles and Illustration of Voltammetric and Related Techniques*. Oxford University Press, 2002.

[208] R. G. Compton, E. Laborda, and K. R. Ward, *Understanding Voltammetry Simulation of Electrode Processes*. Imperial College Press, 2014.

[209] D. J. Gavaghan and S. W. Feldberg *J. Electroanal. Chem.*, vol. 491, pp. 103–110, 2000.

[210] R. A. Marcus and P. Siders *J. Phys. Chem.*, vol. 86, pp. 622–630, 1982.

[211] E. Kätelhön and R. G. Compton *ChemElectroChem*, vol. 2, pp. 64–67, 2015.

[212] P. P. Edwards, H. B. Gray, M. T. J. Lodge, and R. J. P. Williams *Angew. Chemie Int. Ed.*, vol. 47, pp. 6758–6765, 2008.

[213] M. Hugelmann and W. Schindler *Surf. Sci.*, vol. 541, pp. L643–L648, 2003.

[214] S. W. Feldberg *J. Electroanal. Chem. Interfacial Electrochem.*, vol. 198, pp. 1–18, 1986.

[215] S. Teukolsky, W. Vetterling, B. Flannery, and W. V. W.H. Press, S.A. Teukolsky, *Numerical Recipes: The Art of Scientific Computing*. Cambridge University Press, 2007.

[216] T. M. Alligrant, M. J. Anderson, R. Dasari, K. J. Stevenson, and R. M. Crooks *Langmuir*, vol. 30, pp. 13462–13469, 2014.

[217] S. V. Sokolov, T. R. Bartlett, P. Fair, S. Fletcher, and R. G. Compton *Anal. Chem.*, vol. 88, pp. 8908–8912, 2016.

[218] S. Q. Wang and H. W. Lim, *Principles and practice of photoprotection*. Springer International Publishing, 2016.

[219] A. Hervault and N. Thanh *Nanoscale*, vol. 6, pp. 11553–11573, 2014.

[220] E. Tomaszewska, K. Soliwoda, K. Kadziola, B. Tkacz-Szczesna, G. Celichowski, M. Cichomski, W. Szmaja, and J. Grobelny *J. Nanomater.*, vol. 2013, p. 60, 2013.

[221] K. Tschulik, C. Batchelor-McAuley, H.-S. Toh, E. J. E. Stuart, and R. G. Compton *Phys. Chem. Chem. Phys.*, vol. 16, pp. 616–623, 2014.

[222] H. S. Toh, C. Batchelor-McAuley, K. Tschulik, M. Uhlemann, A. Crossley, and R. G. Compton *Nanoscale*, vol. 5, p. 4884, 2013.

[223] L. Piankova, N. Malakhova, N. Stozhko, K. Brainina, A. Murzakaev, and O. Timoshenkova *Electrochem. Commun.*, vol. 13, pp. 981–984, 2011.

[224] H. S. Toh, K. Jurkschat, and R. G. Compton *Chem. - A Eur. J.*, vol. 21, pp. 2998–3004, 2015.

[225] H. S. Toh, C. Batchelor-McAuley, K. Tschulik, and R. G. Compton *Sci. China Chem.*, vol. 57, pp. 1199–1210, 2014.

[226] J. J. Yoo, J. Kim, and R. M. Crooks *Chem. Sci.*, vol. 6, pp. 6665–6671, 2015.

[227] H. Deng and G. J. V. Berkel *Electroanalysis*, vol. 11, pp. 857–865, 1999.

[228] T. Noyhouzer, M. E. Snowden, U. M. Tefashe, and J. Mauzeroll *Anal. Chem.*, vol. 89, pp. 5246–5253, 2017.

[229] T. Noyhouzer and D. Mandler *Electroanalysis*, vol. 25, pp. 109–115, 2013.

[230] K. Cinková, M. Clark, S. V. Sokolov, C. Batchelor-McAuley, A. Švorc, and R. G. Compton *Electroanalysis*, vol. 29, pp. 1006–1013, 2016.

[231] R. C. Matos, M. A. Augelli, C. L. Lago, and L. Angnes *Anal. Chim. Acta*, vol. 404, pp. 151–157, 2000.

[232] J. S. Rossier, H. H. Girault, C. Stuver, H. B. Halsall, W. R. Heineman, E. Buckley, M. R. Smyth, J. F. Abgrall, C. Soria, J. Amiral, P. Ill, J. Clavier, and D. Mottier *Lab Chip*, vol. 1, p. 153, 2001.

[233] S. J. Konopka and B. McDuffie *Anal. Chem.*, vol. 42, pp. 1741–1746, 1970.

[234] T. R. Bartlett, S. V. Sokolov, and R. G. Compton *ChemistryOpen*, vol. 4, pp. 600–605, 2015.